

MODELLING AND ANALYSIS OF MULTI-WALLED CARBON
NANOTUBE REINFORCED POLYMER COMPOSITES

A THESIS SUBMITTED TO
THE BOARD OF CAMPUS GRADUATE PROGRAMS
OF MIDDLE EAST TECHNICAL UNIVERSITY
NORTHERN CYPRUS CAMPUS

BY

BUSHRA FATIMA

IN PARTIAL FULLFILLMENT OF THE REQUIREMENTS
FOR
THE DEGREE OF MASTER OF SCIENCE
IN
SUSTAINABLE ENVIRONMENT AND ENERGY SYSTEMS

AUGUST 2016

Approval of the Board of Graduate Programs

Prof. Dr. M. Tanju Mehmetođlu
Chairperson

I certify that this thesis satisfies all the requirements as a thesis for the degree of Master of Science.

Assoc. Prof. Dr. Ali Muhtaroglu
Program Coordinator

This is to certify that we have read this thesis and that in our opinion it is fully adequate, in scope and quality, as a thesis for the degree of Master of Science.

Assoc. Prof. Dr. Volkan Esat
Supervisor

Examining Committee Members

Assoc. Prof. Dr. Volkan Esat	Mechanical Engineering Prog. METU NCC	_____
Assoc. Prof. Dr. M. Murat Özer	Physics Group METU NCC	_____
Assist. Prof. Dr. Behzat Kentel	Mechanical Engineering Prog. METU NCC	_____
Assist. Prof. Dr. Mustafa E. Özser	Chemistry Group METU NCC	_____
Assist. Prof. Dr. Neriman Özada	Mechanical Engineering Dept. EMU NCC	_____

ETHICAL DECLARATION

I hereby declare that all information in this document has been obtained and presented in accordance with academic rules and ethical conduct. I also declare that, as required by these rules and conduct, I have fully cited and referenced all material and results that are not original to this work.

Name, Last name : Bushra Fatima

Signature :

ABSTRACT

MODELLING AND ANALYSIS OF MULTI-WALLED CARBON NANOTUBE REINFORCED POLYMER COMPOSITES

Fatima, Bushra

M.S., Sustainable Environment and Energy Systems Program

Supervisor: Assoc. Prof. Dr. Volkan Esat

August 2016, 114 Pages

In this study, multi-walled carbon nanotubes (MWNTs) and multi walled carbon nanotube reinforced epoxy composites (CNTRPs) are investigated by means of computational modelling. To begin with, individual tubes of MWNTs are modelled with varying chiralities through equivalent continuum modelling in order to examine their essential mechanical properties including Young's modulus, shear modulus, and Poisson's ratio. The finite element models developed incorporate beam elements that represent Carbon-Carbon bonds within each nanotube and spring elements that represent van der Waals interaction between concentric tubes. Unlike the models reported in literature, this study considers the variation of intershell spacing with varying inner diameters. Similarly, the literature has so far neither reported any results for the chiral configuration of MWNTs nor have reported any comparison between polychiral and monochiral configurations. This study determines the properties of MWNTs by considering both the polychiral and monochiral configurations. Novel relationships of tensile resistance and torsional stiffness are also obtained in terms of outer tube diameter of an MWNT. In the second part of the thesis, CNTRPs are modelled that embed 5 percent by volume of MWNTs, already modelled in the first part, as reinforcement elements in the epoxy resin. Continuum modelling and discrete modelling approaches are employed to model CNTRPs. In the former model, the interphase region is assumed to have perfect bonding with the polymer matrix and the MWNT, whereas in the latter the interphase is modelled using weak Van der Waals interactions that are characterized by Lennard-Jones "6-12" potential. The simulated Young's moduli show good agreement with the published computational results and analytical continuum rule of mixtures. In addition, influence of chirality and size of MWNTs on the Young's modulus and Poisson's ratio of CNTRPs are also studied. In general, CNTRPs reinforced with polychiral MWNTs are stiffer

than the ones reinforced with monochiral MWNTs which are more resistant to lateral deformation.

Keywords: multi-walled carbon nanotube, carbon nanotube reinforced epoxy composite, continuum modelling, discrete modelling, van der Waals, finite element method, polychiral, monochiral

ÖZ

ÇOK DUVARLI KARBON NANOTÜP TAKVİYELİ POLİMER KOMPOZİTLERİN MODELENMESİ VE ANALİZİ

Fatima, Bushra

Yüksek Lisans, Sürdürülebilir Çevre ve Enerji Sistemleri Programı

Tez Yöneticisi: Doç. Dr. Volkan Esat

Ağustos 2016, 114 sayfa

Bu tez kapsamında Çok Duvarlı Karbon Nanotüpler (ÇDKNT) ve Karbon Nanotüp Takviyeli Polimer (KNTTP) kompozitler hesaplamalı modelleme yöntemi vasıtasıyla araştırılmaktadır. ÇDKNT tüpleri, eşdeğer sürekli ortamlar modellemesiyle değişen kiralitelerde modellenmiş ve Young modülü, kesme modülü ve Poisson oranı gibi temel mekanik özellikleri incelenmiştir. Oluşturulan sonlu elemanlar modelleri, her bir nanotüpte karbon-karbon bağı temsil eden kiriş elemanları ve iç içe tüplerin aralarındaki van der Waals etkileşimlerini sağlayan yay elemanları içermektedir. Literatürdeki modellerin aksine, bu çalışmada iç içe tüpler arasındaki mesafe değişken alınmıştır. Benzer şekilde, literatürde ne kiral konfigürasyonun sonuçları rapor edilmiş, ne de polikiral ve monokiral konfigürasyonlar karşılaştırılmıştır. Bu çalışmada ÇDKNT'lerin polikiral ve monokiral konfigürasyonları dikkate alınmıştır. Tezin ikinci kısmında, ilk kısımda modellenmiş olan ÇDKNT'ler epoksi reçine içinde hacmen %5 kaplayacak şekilde takviye elemanı olarak kullanılarak KNTTP'ler modellenmiştir. KNTTP'lerin oluşturulmasında sürekli ortamlar modellemesi ve münferit modelleme yöntemleri kullanılmıştır. Sürekli ortamlar modellemesinde ara bölgede polimer matrisi ve ÇDKNT'ler arasında mükemmel bağ olduğu öngörülürken, münferit modelleme yönteminde zayıf van der Waals etkileşimleri Lennard-Jones "6-12" potansiyeliyle oluşturulmaktadır. Simülasyon sonuçları, yayımlanmış hesaplamalı model sonuçları ve analitik karışımlar kuralıyla elde edilmiş sonuçlarla iyi bir uyum göstermektedir. Ek olarak, ÇDKNT'lerin kiralite ve boyutlarının KNTTP'lerin Young modülü ve Poisson oranı gibi temel mekanik özelliklerine olan etkileri çalışılmıştır.

Anahtar Kelimeler: Çok duvarlı karbon nanotüp (ÇDKNT), karbon nanotüp takviyeli polimer kompozit (KNTTP), sürekli ortamlar modellenmesi, münferit modelleme, van der Waals, sonlu elemanlar yöntemi, polikiral, monokiral

DEDICATION

To my
Cute little niece and nephew
And my beloved parents and siblings.

ACKNOWLEDGEMENTS

I would like to take this opportunity to express my deepest gratitude to my adviser, Dr. Volkan Esat for his invaluable support and guidance for the duration of this thesis that has made this work possible.

I would also like to thank my other committee members, Assoc. Prof. Dr. M. Murat Özer, Assist. Prof. Dr. Behzat Kentel, Assist. Prof. Dr. Mustafa E. Özser and Assist. Prof. Dr. Neriman Özada for their insightful comments and suggestions.

I would also like to convey my heartfelt thanks to the honourable professors in the SEES program for enlightening me with the research methodologies and guidelines.

My sincerest thanks goes to the Mechanical Engineering Program of METU NCC for providing me with an opportunity of being a Teaching Assistant that has been a truly edifying and eye-opening experience. I am humbled by the support and guidance that was extended to me by all the faculty members and fellow teaching assistants.

I would also like to thank my friends Madina Obaidullah, Sundas Khalid, Elham Jahani, Nurgul Temirbekova, Hafsa Nadeem Butt, Maryam Ghias, Aigul Myrzabekova, Samangan Orozbaeva, Çansu Günsel, Çağlan Sevinç, Oya Gürcüoğlu, Humayun Ahmed, Kathy Kiema, Fahad Haneef, Obaidullah Mohiuddin, Ali Hamza, Loiy Al-Ghussain, and Muhammad Saleh Rashid for making my stay in Cyprus memorable. I am also grateful to my respected seniors, Eda Koksall, Fassahat Ullah Qureshi, Muhammad Jibran Shahzad, Muhammad Arsalan Tariq and Sajed Sadati for their guidance in scientific writing.

I would like to extend my love and regards to my mother Mrs. Rubina Khaliq and father Mr. Abdul Khaliq to whom I shall remain indebted for their consistent support and prayers. Last but not least, I would like to extend my gratitude to my brother Muhammad Siddique and my sisters for always being there with me through thick and thin.

TABLE OF CONTENTS

ETHICAL DECLARATION	iii
ABSTRACT.....	iv
ÖZ	vi
DEDICATION	viii
ACKNOWLEDGEMENTS	ix
LIST OF TABLES	xv
LIST OF FIGURES.....	xviii
NOMENCLATURE.....	xxii
Chapter 1	1
1. INTRODUCTION.....	1
1.1. Motivation	1
1.2. Geometry of Carbon Nanotubes	2
1.3. Types of Carbon Nanotubes	6
1.4. Polymer Nanocomposites as Advanced Materials	7
1.5. Mechanical properties of CNTRPs.....	8
1.6. Applications of CNTRPs.....	9
1.7. Thesis Objective and Overview.....	10
Chapter 2.....	12

2. LITERATURE REVIEW	12
2.1. Literature Review on MWNTs	12
2.1.1 Synthesis of CNTs	12
2.1.1.1 Arc Discharge Technique	13
2.1.1.2 Laser Ablation Technique	14
2.1.1.3 Chemical Vapour Deposition	15
2.1.2 Structure of MWNTs	16
2.1.3 Experimental Techniques for Determining Properties of MWNTs	18
2.1.4 Modelling Techniques for Simulating Individual Tubes of MWNTs	21
2.1.5 Modelling Techniques for Simulating van der Waals Force	22
2.2. Literature Review on CNTRPs	30
2.2.1. Synthesis of CNTRPs	30
2.2.2. Nanotube-Reinforced Epoxy Composites	31
2.2.3. Experimental Results on the properties of CNTRPs	32
2.2.4. Modelling Techniques for Simulating CNTRPs	34
2.2.5. Modelling the Interphase Region	36
2.2.6. Challenges in Commercializing CNTRPs	36
2.3. Gaps in the Literature	37
Chapter 3	38
3. FINITE ELEMENT MODELLING OF MULTI-WALLED CARBON NANOTUBES	38
3.1. Simulation of SWNTs	38
3.1.1. Equivalent Continuum Modelling	39

3.1.1.1. Molecular Mechanics	39
3.1.1.2. Structural Mechanics	40
3.1.1.3. Interrelationship between Molecular and Structural Mechanics	41
3.2. Simulation of vdW Interaction Between Adjacent Tubes	44
3.2.1. Intershell Spacing of MWNTs.....	45
3.2.2. Lennard-Jones Force	46
3.3. Numerical Results and Discussion	49
3.3.1. Prediction of Young's Modulus of MWNTs.....	53
3.3.1.1. Impact of DWNT's Diameter and Chirality on its Young's Modulus	55
3.3.1.2. Impact of Intershell Spacing on the Young's Modulus of DWNTs	57
3.3.1.3. Impact of Number of Tubes on Young's Modulus of MWNTs	59
3.3.1.4. Influence of Axial Length on DWNT's Young's Modulus.....	60
3.3.2. Prediction of Shear Modulus of MWNTs.....	62
3.3.2.1. Impact of DWNT's Diameter and Chirality on its Shear Modulus	63
3.3.2.2. Influence of Intershell Spacing on DWNT's Shear Modulus.....	64
3.3.2.3. Influence of Number of Tubes on MWNT's Shear Modulus.....	65
3.3.3. Prediction of Shear Strain of MWNTs	66
3.3.3.1. Impact of DWNT's Diameter and Chirality on its Shear Strain.....	67
3.3.3.2. Impact of Intershell Spacing on Shear Strain of DWNTs	68
3.3.3.3. Impact of Number of Tubes on Shear Strain of MWNT	69
3.3.4. Prediction of Poisson's Ratio of MWNTs.....	70
3.3.4.1. Impact of DWNT's Diameter and Chirality on its Poisson's Ratio	70
3.3.4.2. Impact of Number of Tubes on Poisson's Ratio of MWNTs	72

3.3.5. Tensile resistance and Torsional Stiffness of MWNTs	73
3.4. Model Validation.....	74
Chapter 4	78
4. MULTI-WALLED CARBON NANOTUBE REINFORCED POLYMER COMPOSITES	78
4.1. Simulation Models of CNTRPs.....	78
4.1.1. Discrete Modelling Approach	79
4.1.2. Continuum Modelling Approach.....	82
4.2. Model Validation.....	83
4.3. Numerical Results and Discussion	86
4.3.1. Prediction of Young’s Modulus of RVE	87
4.3.2. Prediction of Poisson’s Ratio of RVE	89
4.4. Predicted Reduction of Crude Oil Consumption.....	91
Chapter 5	92
5. CONCLUSIONS AND FUTURE WORK.....	92
5.1. Conclusions	92
5.2. Future Work	94
6. REFERENCES.....	95
APPENDIX A	102
7. CHARACTERISTICS OF SIMULATED FINITE ELEMENT MODELS.....	102
APPENDIX B	104
8. IMPORTANT NUMERICAL RESULTS.....	104
APPENDIX C	113

9. SENSITIVITY ANALYSIS OF CONTINUUM MODELS	113
---	-----

LIST OF TABLES

Table 1.1. The chiralities of different types of CNT configurations [16,18].	5
Table 2.1 Summary of the experimental published results of the Young's modulus (E) of MWNTs.....	20
Table 2.2 Properties of MWNT with n number of tubes as found by [54].	29
Table 2.3 Precis of the mechanical properties of MWNTs as reported in literature.	30
Table 2.4 Young's modulus of pure epoxy resin and CNTRP epoxy composite containing 1 and 4 % by weight of MWNT respectively [59].....	33
Table 2.5 Young's modulus of the MWNT/epoxy composite reinforced with 0, 0.1, 0.5, 1.0, 1.5, 2 and 3 wt. % MWNTs as reported by [61].	33
Table 2.6 Summary of the experimental results of MWNT/epoxy composites available in literature (E_m and E_c refer to the Young's modulus of polymer matrix and composite respectively).	34
Table 2.7 Simulation results of the Young's moduli of the composite (E_c) and its Poisson's ratio against different moduli of the matrix (E_m) [29].....	35
Table 3.1 Cross-Sectional properties of the circular beam element used for modelling C-C bond, taken from [72].....	43
Table 3.2 Characteristics of monochiral and polychiral DWNTs investigated.	51
Table 3.3 Characteristics of TWNT investigated.	52
Table 3.4 Characteristics of MWNT investigated.	52
Table 3.5 Effect of chirality on the average Young's moduli of DWNT and the corresponding standard deviation.	57
Table 3.6 Different configurations of monochiral armchair and zigzag under investigation to study the effect of intershell spacing	58
Table 3.7 Different configurations of monochiral armchair and zigzag MWNTs under investigation to study the effect of number of tubes.	59

Table 3.8 Influence of number of tubes on the average elastic moduli of MWNT (n is the number of tubes).....	60
Table 3.9 Effect of length on the Young's modulus of DWNT.	62
Table 3.10 Effect of chirality on the average shear moduli of DWNT and the corresponding standard deviation.	64
Table 3.11 Influence of number of tubes on the average shear moduli of zigzag and armchair MWNT (n is the number of tubes).	66
Table 3.12 Effect of chirality on the average shear strain of the outer tube of DWNT.	67
Table 3.13 Effect of number of tubes on the average shear strain of MWNT (n is the number of tubes).	69
Table 3.14 Effect of chirality on the average Poisson's ratio of DWNT and the corresponding standard deviation.	72
Table 3.15 Reported and predicted average mechanical properties of DWNTs.	77
Table 4.1 Comparison of numerical results of the elastic modulus of the epoxy composite reinforced with zigzag and armchair DWNTs with the analytical results by rule of mixtures and modified rule of mixture.	84
Table 4.2 Comparison of numerical results of the epoxy composite reinforced with zigzag DWNT against the extrapolated results from the trend found by Joshi and Upadhyay [29].....	85
Table 4.3 Properties of CNTRP RVE models reinforced with DWNT.....	87
Table 4.4 Effect of DWNT's helicity on the Poisson's ratio of the RVE about 8 nm in diameter.	90
Table 4.5 Properties of glass fibre, DWNT (9, 0) - (20, 0) and neat epoxy resin along with their composites. (Asterisked entities are taken from [79]).....	91
Table A.1 Characteristics of the simulated DWNT models.	102
Table A.2 Characteristics of the simulated continuum RVE models.	103
Table B.1 Predicted Young's moduli of Monochiral and Polychiral DWNTs.	104
Table B.2 Predicted Young's moduli of Monochiral triple walled carbon nanotubes.	105
Table B.3 Predicted Young's moduli of Monochiral Four-walled carbon nanotubes.....	106

Table B.4 Predicted Shear Moduli of Monochiral and Polychiral DWNTs.....	107
Table B.5 Predicted Shear Moduli of Monochiral triple-walled carbon nanotubes.....	108
Table B.6 Predicted Shear Moduli of Monochiral four-walled carbon nanotubes.....	108
Table B.7 Predicted Shear Strain of Monochiral and Polychiral DWNTs.....	109
Table B.8 Predicted Poisson’s ratio of Monochiral and Polychiral DWNTs.....	110
Table B.9 Predicted Young’s moduli of the RVE.....	111
Table B.10 Predicted Poisson’s Ratio of RVE.....	112
Table C.1 Mesh refinement of continuum model RVE reinforced by monochiral armchair DWNT (15, 15) – (21, 21) by Young’s modulus sensitivity analysis.....	113

LIST OF FIGURES

Figure 1.1 Basic hexagonal repeat unit of a graphene sheet [13].....	3
Figure 1.2. Illustration of chiral vector (Ch) and chiral angle (θ) in a graphene sheet.	4
Figure 1.3 Side views of (a) armchair (11, 11), (b) zigzag (16, 0), and (c) chiral (16, 5) nanotubes.....	5
Figure 1.4 Repeat units of (a) armchair (11, 11) and (b) zig-zag (16, 0) carbon nanotubes.	6
Figure 1.5 Illustration of (a) single-walled and (b) multi-walled carbon nanotubes.	7
Figure 1.6 Prospective applications of CNTRPs as envisioned by TASC [33].	10
Figure 2.1 Schematic of arc discharge method [40].....	14
Figure 2.2 Schematic of Laser Ablation method [40].	15
Figure 2.3 TEM of MWNT produced by (a) arc-discharge (b) Catalytic decomposition of acetylene [38].	16
Figure 2.4 Structure of MWNT. (a) Russian Doll or nested tube model. (b) Parchment or Scroll Model [23].....	17
Figure 2.5 Plot of energy cost per unit area for converting graphene into nanotubes against the width (W) of graphene layer [46].	18
Figure 2.6 Initial pressure P_{ij} caused by van der Waals interaction between tubes i and j of a 10-walled MWNT with innermost radius = 0.68 nm, interlayer distance=0.34 nm, thickness of the tube=0.34 nm.....	23
Figure 2.7 Normalized load-displacement curve for the non-linear truss rod [53].	24
Figure 2.8 Spring modelling stages of Lennard-Jones Force [5].	26
Figure 2.9 Variation of interlayer pressure with interlayer distance [4].	28
Figure 3.1 Simulation of a SWNT as a space-frame structure with its beams and joints representing carbon-carbon bonds and carbon atoms respectively.	38
Figure 3.2 Illustration of interatomic interactions in molecular mechanics.	40

Figure 3.3 Illustration of a uniform beam under pure tension, bending moment and Torsion moment.....	41
Figure 3.4 Simulation of a single tube of MWNT with zigzag configuration (16, 0).....	44
Figure 3.5 Plot of intershell spacing versus average diameter of a MWNT with different number of shells [75].....	46
Figure 3.6 Plot of Lennard-Jones potential versus the interatomic distance.....	47
Figure 3.7 Plot of Lennard-Jones force versus the interatomic distance.....	48
Figure 3.8 The portion of force-displacement curve considered in the study to simulate the stiffness of the springs used for modelling vdW interaction among the adjacent tubes of MWNT.....	49
Figure 3.9 Finite element mesh of armchair DWNT of configuration (5, 5) - (11, 11) (a) Isometric view (b) Top view.....	50
Figure 3.10 Schematic illustration of the cross section of a DWNT depicting thickness (t), inner diameter (d_i) and outer diameter (d_o).....	53
Figure 3.11 Model mesh of (a) zigzag (5, 0) - (16, 0), (b) armchair (3, 3) - (9, 9) (c) armchair-chiral (2, 2) - (13, 2) and (d) zigzag-chiral (3, 0) - (13, 2) showing the imposed boundary conditions.....	54
Figure 3.12 Simulation of Armchair (3, 3) - (9, 9) DWNT subjected to axial displacement (Both original and deformed simulations are shown).....	55
Figure 3.13 Young's Moduli versus the outer tube diameter of DWNT for zigzag, armchair, armchair-chiral and zigzag-chiral configurations.....	56
Figure 3.14 The relation between tensile resistance and the intershell spacing of DWNT of an outer diameter of ~ 1.7 nm for monochiral zigzag and armchair configurations.....	58
Figure 3.15 The relation between Young's Moduli and the number of tubes of MWNT with an outermost tube diameter of ~ 3.0 nm.....	60
Figure 3.16 The relation between Young's Moduli and the length of DWNT for zigzag (9, 0) - (20, 0) and armchair (5, 5) - (11, 11).....	61
Figure 3.17 Simulation of Zigzag (8, 0) - (19, 0) DWNT subjected at one end to torsional load about the axial axis and fixed at the other end (Both original and deformed simulations are shown).....	63

Figure 3.18 Shear moduli versus the outer tube diameter of DWNT for zigzag, armchair, armchair-chiral and zigzag-chiral configurations.....	64
Figure 3.19 The relation between shear moduli and the intershell spacing of DWNT of an outer diameter of ~1.7 nm for zigzag, armchair, armchair-chiral and zigzag-chiral configurations. ...	65
Figure 3.20 The relation between shear moduli and the number of tubes of MWNT with an outermost tube diameter of ~3.0 nm.....	66
Figure 3.21 Shear strain versus the outer tube diameter of DWNT for zigzag, armchair, armchair-chiral and zigzag-chiral configurations.....	68
Figure 3.22 The relation between shear strain and the intershell spacing of DWNT of an outer diameter of ~1.7 nm for monochiral zigzag and monochiral armchair configurations.	69
Figure 3.23 The relation between shear strain and the number of tubes of MWNT with an outer most tube diameter of ~3.0 nm.....	70
Figure 3.24 Poisson’s ratio versus the outer tube diameter of DWNT for zigzag, armchair, armchair-chiral and zigzag-chiral configurations.....	71
Figure 3.25 The relation between Poisson’s ratio and the number of tubes of MWNT with an outermost tube diameter of ~3.0 nm.....	72
Figure 3.26 The relation between tensile resistance and the outer tube diameter of MWNT.	73
Figure 3.27 The relation between torsional stiffness and the outer tube diameter of MWNT. ...	74
Figure 3.28 Comparison of the simulation results of Young’s modulus for monochiral armchair and zigzag MWNTs with the computational results computed by [4,53] and experimental results reported by [41,42].....	75
Figure 3.29 Comparison of the simulation results for monochiral armchair and zigzag MWNTs with the computational results computed by [4,5,53].	76
Figure 4.1 Types of RVE model (a) circular, (b) square (c) hexagonal together with its constituents.....	79
Figure 4.2 Finite Element model of RVE simulated by discrete modelling approach: (a) isometric view (b) Top view.	81
Figure 4.3 Finite Element model of RVE simulated by continuum modelling approach: (a) isometric view (b) Top view.	82

Figure 4.4 Illustration of the increasing linear trend between E_f / E_m and E_c / E_m as found by Joshi and Upadhyay [29].	84
Figure 4.5 Model mesh of an RVE reinforced with zigzag (9, 0) - (20, 0) DWNT highlighting the imposed boundary conditions.	88
Figure 4.6 The relation between Young's Moduli and RVE diameter of CNTRPs reinforced with DWNT zigzag, armchair, armchair-chiral and zigzag-chiral configurations.	89
Figure 4.7 The relation between Poisson's ratio and RVE diameter of CNTRPs reinforced with DWNT zigzag, armchair, armchair-chiral and zigzag-chiral configurations.	90
Figure C.1 Mesh refinement of continuum model RVE reinforced by monochiral armchair DWNT (15, 15) – (21, 21).	114

NOMENCLATURE

2α	Change in rotation angle (rad)
γ_o	Shear strain of the outermost tube
γ	Shear strain
$\Delta\beta$	Twist angle
$\Delta\theta$	Bond length variation due to bending
$\Delta\emptyset$	Bond length variation due to twisting
Δd	Change in diameter (nm)
ΔL	Axial displacement (nm)
Δr	Bond length variation due to stretching
ε	Lennard-Jones potential constant (kJ/mol)
θ_i	Innermost Chiral angle (degrees)
θ_o	Outermost Chiral angle (degrees)
θ	Chiral angle (degrees)
ν	Poisson's ratio
σ	Lennard-Jones potential constant (nm)
ϕ	Torsional angle (rad)
A	Annular cross-sectional area (nm ²)
a	Length of the unit vector of the hexagonal lattice (nm)
C	Circumference of nanotube (nm)
\vec{C}_h	Chiral vector
d	Diameter (nm), thickness of the circular beam element
d_{CNT}	Diameter of CNT (nm)
d_i	Innermost diameter of MWNT (nm)
d_o	Outermost diameter of MWNT (nm)
\hat{d}_{002}	Intershell spacing (nm)
E	Young's Modulus of MWNT (TPa), Steric potential energy
E_c	Young's Modulus of composite (GPa)
E_m	Young's Modulus of polymer matrix (GPa)

F	Net reaction force (nN)
F_{L-J}	Lennard Jones force (nN)
G	Shear Modulus (TPa, GPa)
I	Area moment of inertia (nm ⁴)
J	Polar moment of inertia (nm ⁴)
k	Spring constant (nN/nm)
k_{θ}	Force constants of bending resistance
k_{τ}	Force constants of torsional resistance
k_r	Force constants of bond stretching resistance
L	Length (nm)
m	Index of chiral vector
M	pure bending moment (nN nm)
n	Index of chiral vector
N	axial force (nN)
r	Inter-atomic distance of the interacting atoms
r_0	Critical distance (nm)
t	Thickness of the annular tube (nm)
T	Torsional load (nN nm)
U	Total potential energy of a molecule
U_{ω}	Potential energy of a molecule energy due to out-of-plane torsion (bond inversion),
U_{τ}	Potential energy of a molecule energy due to torsion
U_{L-J}	Lennard-Jones potential (kJ)
U_M	Strain energy due to pure bending moment M
U_N	Strain energy due to axial force N
U_T	Strain energy due to pure torsional moment T

CHAPTER 1

INTRODUCTION

1.1. Motivation

This century has seen great technological breakthroughs which consequently resulted in massive material consumption. As a result, generation of the uncontrollable waste together with unsustainable ways of treating them have disrupted the ecosystem at large. This has raised an alarm prompting the research and development organizations across the globe to develop eco-friendly advanced composite materials with integrated waste management of the products to help maintain a sustainable environment economically. Nanocomposites have come into the limelight due to their extraordinary advantages over the conventional composites [1]. Researchers in various disciplines such as material science and engineering, mechanical engineering, and physics are investigating various nanomaterials with carbon nanotubes and its applications being the front runner [2].

After the discovery of fullerenes in 1985, while conducting some investigations on it Iijima accidentally discovered carbon nanotubes (CNTs) in 1991. Fullerene is a spherical structure constituting sixty carbon atoms organized in a pattern of twenty hexagons and twelve pentagons, while nanotubes are an elongated structure with long narrow tubes [3]. Since their discovery, CNTs have been under constant research [4]. They are known to possess exceptional mechanical, thermal and electrical properties including high strength-to-weight ratio, stiffness and resilience due to which they have a variety of applications in diverse engineering and material science [4–6]. Their application especially as molecular reinforcements in polymers to make high strength composites is highly promising owing to their high aspect ratio and surface area to volume ratio. Graphite and carbon fibres, which are analogous to CNTs, are being commercially used as reinforcing agents in composites for well over a decade. However, carbon nanotubes possess all the in-plane properties of graphite making their inherent defect-free bonds among the few strongest bonds in nature. CNTs can thus provide a greater range of applications with far better performance than that obtained from both carbon fibres and graphite. It is also anticipated that

CNTs can provide various other multifunctional properties to the composite other than just being a load-bearing fibre [7].

The applications of CNTs in the industry are, however, only limited owing to the inadequate knowledge, challenges in their processing, scaling up and nanoscale assembling [4,7]. In spite of sharing their basic chemistry, fullerene, graphene and CNTs have stark differences in properties which are not fully understood [8], this is why the researchers worldwide have been trying all means to fully understand their properties. It is now evident that application of nanotube based composites would need several more years before its effectiveness is rendered suitable as opposed to the fibre-reinforced composites [7].

Though there are variations in the published results about the precise properties of carbon nanotubes, experiments and theoretical studies report Young's modulus around 1 TPa and tensile strength of around 100 GPa [2]. Being 10-100 times stronger than steel at 1/6th of its weight, carbon nanotubes are an ultimate candidate for the design of a 23,000 miles long cable for the space elevator between space and the Earth [3]. They exhibit thermal stability for up to 2800 °C in vacuum, offer twice as much thermal conductivity as diamond and 100 times more electrical conductivity than copper [2,9]. CNTs form an entirely new category of advanced materials considering their superior material properties [2].

1.2. Geometry of Carbon Nanotubes

Carbon nanotubes are made up of a sheet of graphene which is rolled in the form of a hollow cylinder such that the diameter of the tube is in the order of nanometer and its length in micrometer [10]. Due to this high aspect ratio, they are regarded as one-dimensional structures [11]. Unlike the two-dimensional graphene sheet which suffers from large out-of-plane deformations, carbon nanotubes' strength lies in the strong C-C in-plane bonds that resist any in-plane deformation [12].

The characteristic feature of the graphene sheet is the periodic repetition of the hexagonal network of carbon atoms in space. The hexagonal pattern is created when one carbon atom covalently bonds with three other carbon atoms as a result of sp^2 hybridization. sp^2 hybridization occurs when one s -orbital combines with two out of three p -orbitals giving rise to three hybridized sp^2 orbitals

oriented at 120° to each other on a plane. When one of these sp^2 orbitals covalently bonds with the sp^2 orbital of another atom, σ bond is formed which is a strong bond responsible for the superior mechanical properties of CNTs [13]. The un-hybridized p -orbital gives rise to the relatively weaker bond, known as the π -bond. Figure 1.1 shows the basic hexagonal repeat unit of the graphene sheet together with its σ and π -bonds.

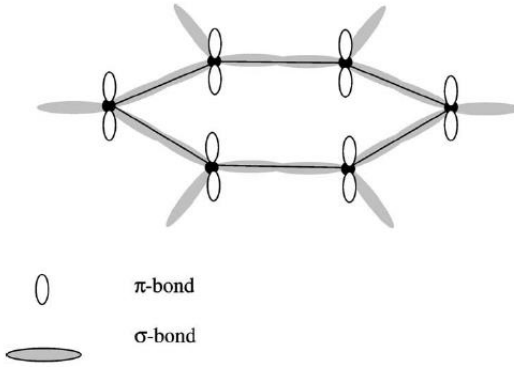


Figure 1.1 Basic hexagonal repeat unit of a graphene sheet [13].

When graphene sheet is rolled in the form of a tubular structure of CNT, the σ and π -bonds re-hybridize therefore CNTs do not comprise pure sp^2 bonding [13]. Figure 1.2 illustrates the geometry of CNTs defined by their chirality which depends on how the hexagons are packed in the graphene sheet. Chirality, also known as helicity, is well-elucidated using a chiral vector (\vec{C}_h) or a chiral angle (θ). Chiral vector, also called the roll up vector, can be expressed as a sum of unit translational vectors of the hexagonal lattice as given by Equation (1.1) [9]. Chiral angle is the angle between the chiral vector and the axis corresponding to $(n, 0)$ which determines the amount of twist in the tube and can be calculated by Equation (1.2) [11,14].

$$\vec{C}_h = n\vec{a}_1 + m\vec{a}_2 \quad (1.1)$$

$$\theta = \sin^{-1} \frac{\sqrt{3}m}{2\sqrt{n^2 + nm + m^2}} \quad (1.2)$$

where n and m are the indices in integers that correspond to the number of steps along the Carbon-Carbon bond of the hexagonal lattice and a_1 and a_2 are the unit cell base vectors of the graphene

sheet given by $a = a_1 = a_2 = \sqrt{3}L$ where a is the unit vector length and L is the Carbon-Carbon bond length in graphene, taken as 0.142 nm [11,15,16].

The graphene sheet rolls over such that the head of the \vec{C}_h joins its tail, giving a tubular structure with its axis being perpendicular to this chiral vector. The resulting circumference (C) and diameter (d_{CNT}) of the CNT are given by Equation (1.3) and Equation (1.4) respectively [11].

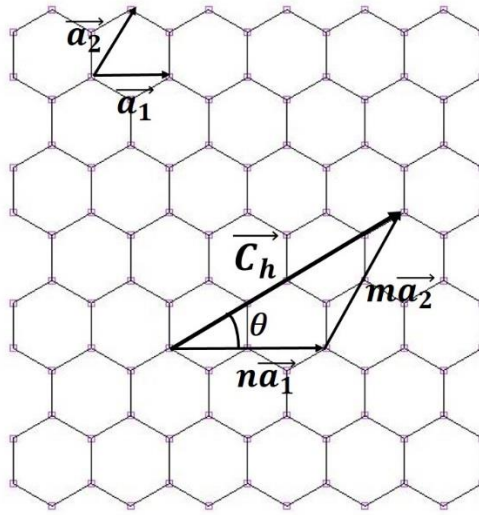


Figure 1.2. Illustration of chiral vector (\vec{C}_h) and chiral angle (θ) in a graphene sheet.

$$C = a\sqrt{n^2 + nm + m^2} \quad (1.3)$$

$$d_{CNT} = \frac{C}{\pi} \quad (1.4)$$

Depending on their chirality, nanotubes' configurations can be classified as achiral and chiral. Achiral nanotubes exhibit symmetry in their structure, while chiral nanotubes do not. Achiral nanotubes can be further classified into armchair and zigzag nanotubes [17]. The three types of nanotube configuration with their respective chiral vector indices and chiral angle are tabularized in Table 1.1.

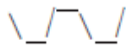
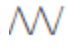
Figure 1.3 displays the side views of the three types of nanotubes. Figure 1.3a shows an armchair configuration (11, 11), the name coming from the resemblance to an armchair  shape perpendicular to the tubular axis. Figure 1.3b shows a zigzag configuration (16, 0), the name coming from the zigzag  shape perpendicular to the tubular axis. Figure 1.3c shows a chiral or helical configuration (16, 5) which does not have any consistent pattern perpendicular to the tube's axis [12].

Table 1.1. The chiralities of different types of CNT configurations [16,18].

Nanotube Configuration	Chiral Vector Indices	Chiral Angle θ
Armchair	(n, n)	30°
Zigzag	$(n, 0)$	0°
Chiral	(n, m) where $n \neq m$ and $n > m > 0$	$0^\circ < \theta < 30^\circ$

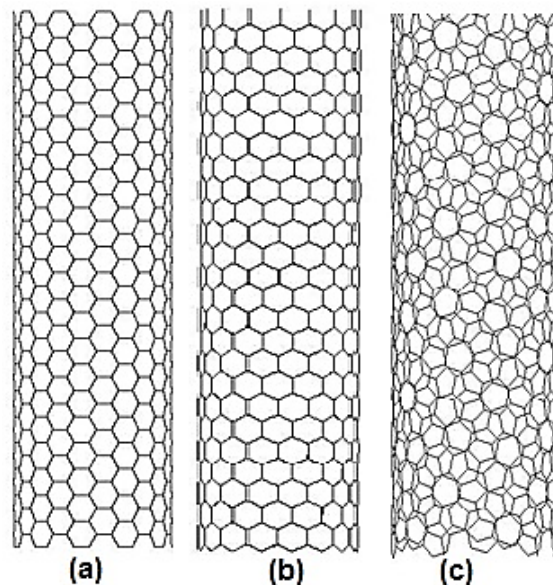


Figure 1.3 Side views of (a) armchair (11, 11), (b) zigzag (16, 0), and (c) chiral (16, 5) nanotubes.

Figure 1.4 shows the repeat unit for armchair (11, 11) and zigzag (16, 0) nanotubes. Both armchair and zigzag nanotubes are symmetric about their tube axis with the repeat units' length being equal to 0.25 nm and 0.43 nm respectively (the repeat unit is considered along the tube's axis) [12]. Both armchair and zigzag nanotubes demonstrate translational symmetry [19].

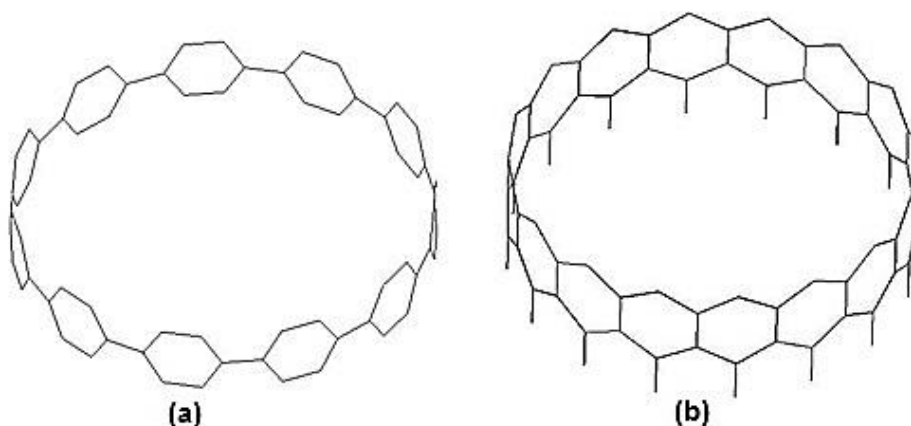


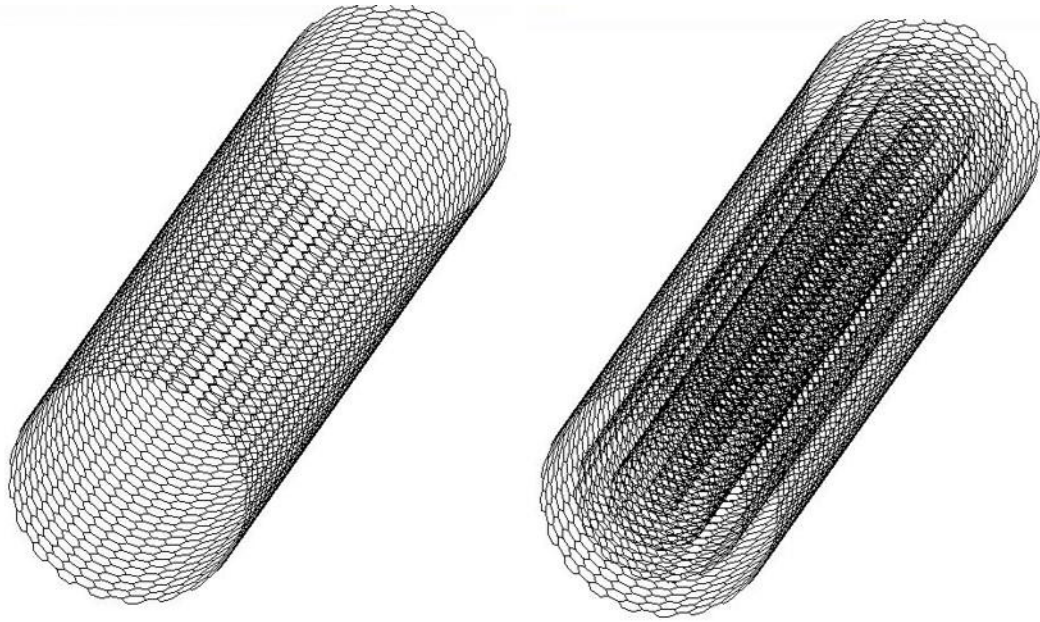
Figure 1.4 Repeat units of (a) armchair (11, 11) and (b) zigzag (16, 0) carbon nanotubes.

The arrangement of the array of hexagons along the tube governs if the CNT is metallic or semi-conducting in nature [10]. Carbon nanotubes are metallic if their indices follow the relation $n - m = 3q$ where q is an integer and are semi-conducting if their indices follow the relation $n - m = 3q \pm 1$ [11]. According to this criteria, all armchair nanotubes are metallic in nature whereas only a few of zigzag nanotubes are metallic.

1.3. Types of Carbon Nanotubes

Carbon nanotubes can be categorized into two groups according to the number of concentric tubes: single walled carbon nanotubes (SWNTs) and multi-walled carbon nanotubes (MWNTs). Figure 1.5 illustrates these types.

SWNT is a graphene sheet rolled up into a seamless tube or cylinder enclosed at both ends with one half of a dome-shaped fullerene molecule [12,16,20]. The curvature in the sidewall is the effect of rolling up the graphene sheet, while the curvature on the end caps is a result of topological defects in the form of pentagonal rings. The positive convex curvature as a result of the pentagonal ring closes the tube [12].



(a) Single-walled carbon nanotube

(b) Multi-walled carbon nanotube

Figure 1.5 Illustration of (a) single-walled and (b) multi-walled carbon nanotubes.

A MWNT is formed when two or more concentric cylinders are placed one into another [20,21]. The ends of the MWNTs are either kept open or closed [12]. The bonds within the shells are strong covalent bonds in nature but weak van der Waals force of attraction binds the shells together [15]. Double-walled carbon nanotubes (DWNTs) are MWNTs that are comprised of two concentric cylinders only.

1.4. Polymer Nanocomposites as Advanced Materials

Polymers today heavily dominate the industrial market because they are not only light in weight but also a significant number of them are ductile. However, for structural applications their mechanical properties may not be adequate enough for load bearing as a structural member as compared to metals and ceramics. Therefore, reinforcement materials in the form of fibres, whiskers, platelets or particles are added in the polymer matrix to form polymer composites which offer enhanced mechanical properties [22].

Since their discovery, polymeric composites have dominated the aerospace, automotive and sports industry [23]. Its preference over metal is due to its advantages over the latter. These include; being lighter in weight, better fatigue performance, being resistant to corrosion,

modifiable mechanical properties, being more flexible with different designs and cheaper assembly costs. Properties of composites are governed by the properties of its constituents and the compatibility between the matrix and the reinforcing agent. The constituents making up the composite are thus chosen based on the application where the composite will be used. Since the polymeric composites have a disadvantage of an invisible impact damage, researchers have been trying to enhance their thermomechanical properties especially for use in structural applications. One method by which the performance of the composite can be enhanced is by incorporating nanoparticles like nano-sized metallic particles, nanoclays, carbon nanotubes and carbon fibres [24]. Incorporation of nanoparticles in the polymer leads to the formation of a new class of materials known as polymer matrix nanocomposites or simply polymer nanocomposites. Since at least one dimension of the filler is nanoscopic in size, high aspect ratio of the nanoparticles significantly enhances the material properties at the interface region between the matrix and the reinforcing agent [22,23].

The last two decades saw an unprecedented development of polymeric nanocomposites. This upsurge in the nanotechnology was made possible due to the development of powerful microscopy techniques and the boost in computer technology [23]. However, their commercialized use is yet to be seen because of the inadequate knowledge of structure-property relationships and ineffective processing techniques at both nano and micro scale [1].

1.5. Mechanical properties of CNTRPs

Carbon-carbon bond is one of the strongest bonds in nature so a structure based on these bonds aligned perfectly along the axis of CNTs would give rise to a material with exceptionally high strength to weight ratio [25]. The fibre-like structure of the nanotubes together with its ability to stiffen locally makes the load transfer at the fibre-matrix interface quite efficient [26]. This makes carbon nanotubes an ideal filler material in the polymer matrix [25] to form a super-tough polymer nanocomposite commonly referred to as carbon nanotube reinforced polymer composites (CNTRPs) [27,28]. CNTRPs are ultra-light in weight thus easier to ship, strong, corrosion resistant and have improved biodegradability and thus are ideal candidates for use in eco-friendly applications [22,25]. Subsequent processing does not break CNTs down, thus making CNT recycling possible without comprising their properties [25]. According to an investigation, adding 1 percent by weight of carbon nanotubes into a matrix increases the stiffness and tensile strength of the resulting composite by 36 to 42 percent, and 25 percent, respectively [29].

Normally, a strong interaction between the fibre and the matrix at their interface in a fibre-reinforced polymer composite increases its stiffness and strength but lowers its toughness owing to the brittle nature of the fibre and absence of crack propagation at the fibre-matrix interface. Conversely, a weak interaction lowers the stiffness and strength of the composite but increases its toughness. However, with CNT used as a filler material, a strong interface would lead to a composite with not only higher stiffness and strength but also higher toughness because of the carbon nanotubes' ability to undergo deformation prior to breaking. As for the weak interface, high toughness can still be obtained owing to the rationale of nano-cracking and crack propagation within the deformation zone [27]. It is reported that CNTRPs can attain tensile strength of 3.6 GPa and elastic modulus of 80 GPa [30].

1.6. Applications of CNTRPs

Among the various organizations investing in carbon nanotubes-based composites, the most prominent ones are NASA for finding its potential applications in the aerospace industry, Zyvex and Mistui corporations for making superior sports goods [7], Babolat for making tennis rackets and Easton Hockey for making carbon nanotubes hockey sticks [31]. A research group going by the name of Technology Research Association for Single-Walled Carbon Nanotubes (TASC) envisions a whole new industry dominated by the composites of nanotubes and graphene by the year 2025 with the vision of creating a low carbon society. Figure 1.6 shows the potential applications of the CNTRPs that TASC is prospecting.

For structural applications, CNTRPs are the ultimate materials for use in the automotive and aerospace industry. It was reported that by replacing the material of airframes made of aluminium with CNTRPs, on average 14.05 percent reduction in structural mass was observed along with 9.8 percent of fuel savings. Moreover, being mechanically strong and light in weight, they are far better than the standard fibre-glass automobile bumpers that require 30 percent by weight or more of fibre-glass as opposed to just 1 to 5 percent of CNTs. CNTRPs bumpers will offer an extra advantage of saving paint consumption by making use of electrostatic spraying because of their capability of conducting electricity. CNTRPs can also be used in earthquake prone areas in the earthquake resistant buildings that will utilize their flexibility [25]. CNTs are now being extensively studied for use in high-efficiency photovoltaic devices where their exceptional physical, electrical and optical properties can be put to use to generate clean renewable energy [32].

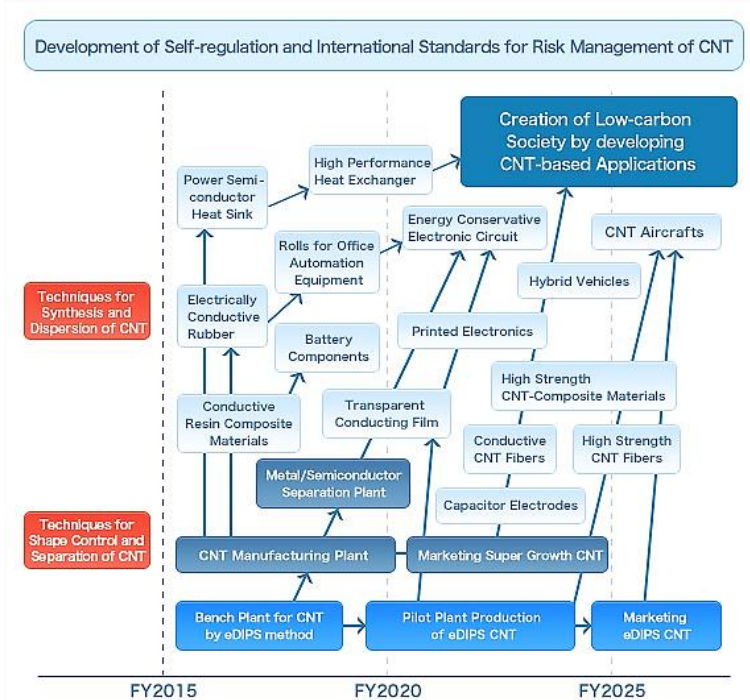


Figure 1.6 Prospective applications of CNTRPs as envisioned by TASC [33].

1.7. Thesis Objective and Overview

The objective of the research is to present a thorough insight into computational modelling which has been utilized to address important aspects of both multi-walled carbon nanotube and multi-walled carbon nanotube reinforced polymer composites. Multi-walled carbon nanotubes are first modelled using Equivalent Continuum Modelling and Lennard-Jones potential. Both polychiral and monochiral MWNTs are modelled and analysed to determine their mechanical properties and the effect of various factors on these properties. The modelled multi-walled carbon nanotubes are then used as reinforcements to model the epoxy composites using two different modelling approaches: discrete and continuum. Thereafter, their mechanical properties are also determined as a function of diameter and chirality of MWNTs.

The thesis is organized such that Chapter 2 summarizes the literature reviewed that helped identify the state-of-the-art modelling techniques and the literature gap. Chapter 3 provides a comprehensive parametric study on the effect of chirality, diameter, intershell spacing and

number of tubes of multi-walled carbon nanotube on their mechanical properties namely Young's modulus, shear modulus and Poisson's ratio. Chapter 4 is dedicated to multi-walled carbon nanotube reinforced polymer composites where its properties are also computationally obtained and their variation with different chirality and size of multi-walled carbon nanotube is also examined. The thesis is concluded in Chapter 5 with possible future work in this area.

CHAPTER 2

LITERATURE REVIEW

Despite having different mechanical properties and being discovered earlier than SWNTs, MWNTs have not been as extensively studied as SWNTs [15,34]. This is partially due to the fact that SWNTs have higher specific stiffness and strength than MWNTs [34]. Nonetheless, it is worth noting that while SWNTs are stiffer than MWNTs under axial strain, MWNTs offer higher resistance to bending and buckling [12,34], therefore if MWNTs are overlooked in applications under axial stress, they should be considered in applications under bending and buckling. Also, MWNTs are easier to produce and easier to purify than SWNTs hence are a lot cheaper [35]. Moreover, as opposed to SWNTs, they do not have the tendency to agglomeration thereby offering better and easier dispersion in the polymer matrix [34], for that reason, the emphasis of the present study is dedicated to MWNTs.

2.1. Literature Review on MWNTs

The section covers the important aspects of multi-walled carbon nanotubes including their synthesis techniques, structure, and experimental and modelling techniques published in the literature so far for the determination of their mechanical properties.

2.1.1 Synthesis of CNTs

The synthesis of CNTs involves heating any carbon-containing source, be it gas or solid. Three main synthesis techniques are:

1. Arc Discharge
2. Laser Ablation
3. Chemical Vapour Deposition (CVD).

While the former two techniques require high temperatures in the range between 1000 to 3000°C to allow the sublimation of the graphite target, the last technique requires medium to low temperatures above 1000°C to allow the reaction between the incoming carbon-containing gas

and the catalyst. On one hand, high-temperature synthesis methods produce less defected nanotubes with narrow diameters of higher crystalline quality and hence more ordered bundles, but they also tend to produce more and a larger variety of impurities and have lack of control on the growth conditions like the size of particles and temperature owing to less homogeneous conditions [36,37]. This means that CVD can help control the growth conditions, consequently minimizing the amount of impurities in the sample and can also control the diameter of the product. Moreover, unlike the former two methods, CVD can also be used for bulk production [36].

2.1.1.1 Arc Discharge Technique

Arc-discharge method is the most popular technique of synthesizing MWNTs. The as-produced MWNTs contain a few point defects, which, though barely affect the elastic properties, can be removed later by use of high temperature annealing [38]. Arc discharge method is an easier technique and produces higher yield than the other techniques [39].

Figure 2.1 illustrates the setup of an arc discharge method. The technique involves generation of an electric arc between the two carbon electrodes, cathode and anode of 5 mm to 20 mm in diameter, placed at a constant distance of 1 to 2 mm apart [37,39]. The generated arc causes the sublimation of the graphitic anode leading to the creation of plasma in the region between the two electrodes. The temperatures in this region can reach up to 600°C which is enough to support the sublimation. Ejaculation of carbon from the solid causes the pressure in the chamber to rise. The carbon atoms then migrate towards the colder region within the chamber where due to strong temperature gradient, they condense onto the cathode as nanotubes [36].

To avoid contamination, this process is carried out in an inert atmosphere with Helium, Argon gas or a mixture of these at a pressure of 100 to 1000 torr [37,39]. In order to produce SWNTs, a metal catalyst (Iron, Nickel, Yttrium, Cobalt or rare earth metals) is added to the bored holes of the anode made of graphite and for MWNTs only a pure sample of graphite is used [2,36,37]. With the pure anode, two types of products are formed: one that deposits on the cathode and the other that forms on the reactor walls in the form of soot. The one deposited on the cathode is comprised of an outer hard shell that consists of fused nanoparticles and MWNTs and an inner

soft core consisting of polyhedral graphitic nanoparticles and MWNTs with the ratio of 1:2. The soot, however, does not contain any nanotubes [36].

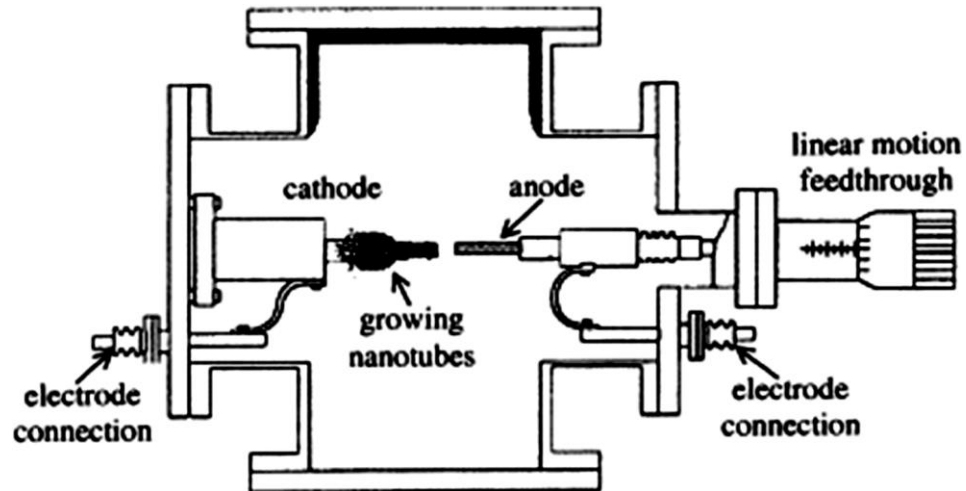


Figure 2.1 Schematic of arc discharge method [40].

Figure 2.3a (Section 2.1.1.3) shows the Transmission Electron Micrograph (TEM) of MWNTs produced from arc discharge technique that has undergone soft purification from a mixture of nanoparticles, graphite and nanotubes [38,41]. The TEM shows the MWNTs consisting of concentric tubes that are perfectly aligned with the axis of the tube and have low density of defects [38,41]. The number of concentric cylinders found in MWNTs are typically 2 to 5 [2].

2.1.1.2 Laser Ablation Technique

Laser Ablation is technically similar to the arc discharge technique [21], as depicted by Figure 2.2. A stream of laser is used to sublime a graphite disc through a quartz tube in an inert environment at high temperature of 1200°C and high pressure of 500 mbar [36,40]. The carbon nanotubes then nucleate in the gaseous state, coalesce, get displaced with the flow of gas and ultimately get deposited on a water-cooled copper collector. The product, containing either SWNTs or MWNTs depending on the flow and pressure conditions in the setup, is then scraped off the wall. There are two different Laser ablation methods employed: pulsed laser and continuous laser. Pulsed Laser uses Nd:YAG (neodymium-doped yttrium aluminium garnet;

Nd:Y₃Al₅O₁₂) laser pulse, while continuous Laser uses a continuous wave of carbon dioxide gas [36].

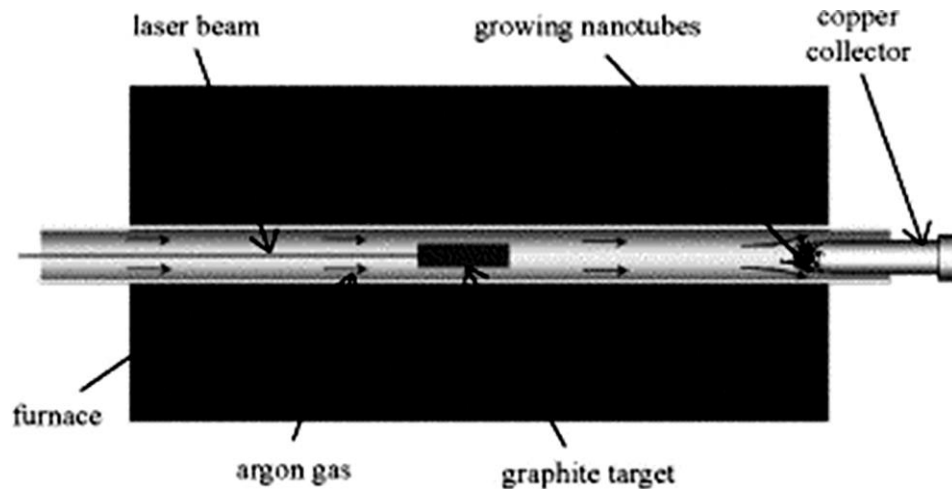


Figure 2.2 Schematic of Laser Ablation method [40].

2.1.1.3 Chemical Vapour Deposition

Carbon nanotubes synthesized using high temperature arc discharge and laser ablation techniques are rendered unsuitable for electronics because most of its components contain aluminium whose melting point is below 700°C, this has prompted low temperature synthesis techniques. In the CVD technique, a mixture of hydrocarbon gas, acetylene, methane (or ethylene) and nitrogen are fed into a reaction chamber maintained at temperatures between 700 and 900 °C at atmospheric pressure. The hydrocarbon is then decomposed to form carbon nanotubes on the substrate [2]. This method, however, produces less ordered MWNTs with structural defects marring the mechanical properties [38]. Despite always producing structurally defected MWNT, catalytic production offers an advantage of controlling the degree of disorder [42]. It is worth stating that elastic properties of nanotubes are more affected by the disorder and stacking defects rather than by the presence of point defects [38]. A type of CVD technique by the name of plasma enhanced CVD (PECVD) has gained popularity because of its ability to produce aligned tubes and ability to control their length [31].

Figure 2.3b shows the TEM of MWNT produced by the catalytic decomposition of acetylene. The TEM shows disordered MWNT with the plane of the tubes tilted approximately at an angle of 30° [38].

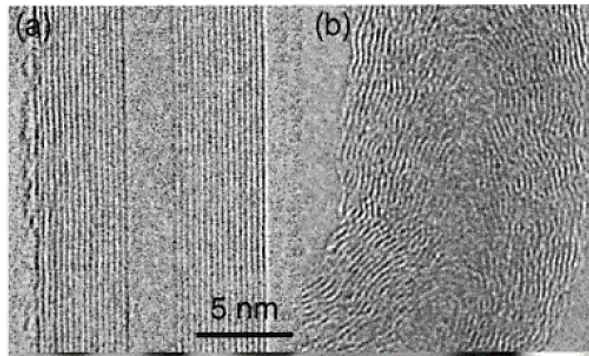


Figure 2.3 TEM of MWNT produced by (a) arc-discharge (b) Catalytic decomposition of acetylene [38].

2.1.2 Structure of MWNTs

MWNTs can be classified as polychiral or monochiral based on the chirality of individual tubes constituting it. A Polychiral MWNT is formed when each of its wall exhibits different chirality to its adjacent wall [43,44], but when every wall exhibits uniform chirality, they are called monochiral MWNTs [43]. Different manufacturing techniques have been investigated to attain MWNT with uniform chirality. Friedrichs et al. [44] synthesized large MWNTs consisting of 70 - 90 concentric tubes with each layer demonstrating same chirality. This was achieved using a modified chemical vapour deposition technique which in addition to a carbon source and a catalyst employed up to 3% of nitrogen [44]. Ruland et al. [43] obtained MWNTs with uniform chirality by catalytic decomposition of iron phthalocyanine. The electron diffraction (ED) patterns of such MWNTs indicate that they are made up of a single rolled up graphene sheet giving rise to a scroll structure [43].

Figure 2.4 shows two different models used to depict the structure of MWNT: the Russian Doll model (or nested tube model) and the Parchment model (or scroll model) [36]. In the former model, it is suggested that MWNT forms when rolled up graphene sheets of sp^2 hybridized carbon atoms are put together in concentric tubes as shown in Figure 2.4a [36,45]. Thus, for a nested structure, since the chirality of individual tubes depends on its diameter, it varies from layer to layer [46]. The scroll model can be depicted by a single graphene sheet that is rolled onto itself like a parchment as shown in Figure 2.4b [36,43].

Out of the two models, the nested tube model is more commonly used [36] due to the fact that it is more stable than the scroll model. The scroll model is regarded as less stable than the nested tube model owing to the existence of two edges along its length. As a result of this difference in stability, transformation occurs between the two structures such that the metastable scroll co-exists with the stable nested structure within individual MWNT which are conspicuously separated by major defects affecting the overall strength of the structure [46].

Figure 2.5 shows the energy associated with the conversion of graphene to nanotubes. The energy associated with the formation of a multi-walled carbon nanotube involves the required strain energy to form the tubular structure which is followed by a gain in the energy upon the formation of an additional wall that increases the interwall interaction at the expense of increased strain energy. The figure shows that SWNTs are stable until the width (W) of 7.7 nm, beyond which double walled carbon nanotubes (DWNTs) are more stable until the width of 17 nm, and beyond which triple-walled carbon nanotubes are more stable. For every width, since the scroll structure are energetically more costly, the nested structure is more stable. For width greater than 0.7 nm, graphene layer with exposed edges is energetically more costly than SWNT, thus making the latter more stable. Scroll structures are energetically more feasible than the graphene with exposed edges beyond the critical W of 8.4 nm. Upon further increasing the width of the graphene, the energy of all MWNTs would asymptotically attain the energy cost of bulk graphite (~ 2.5 eV/mm²) [46].

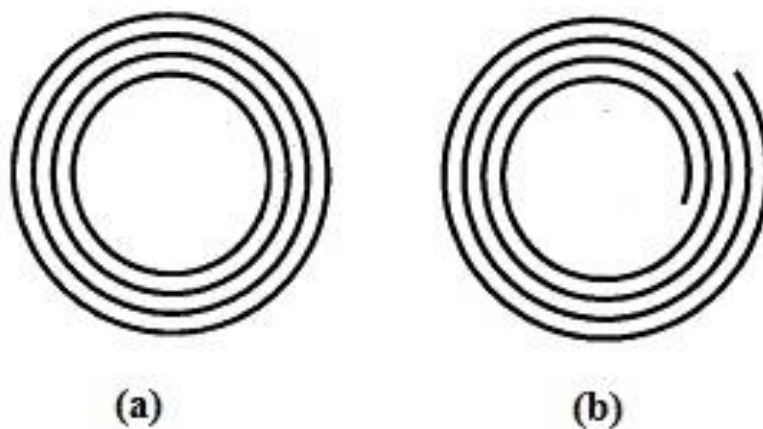


Figure 2.4 Structure of MWNT. (a) Russian Doll or nested tube model. (b) Parchment or Scroll Model [23].

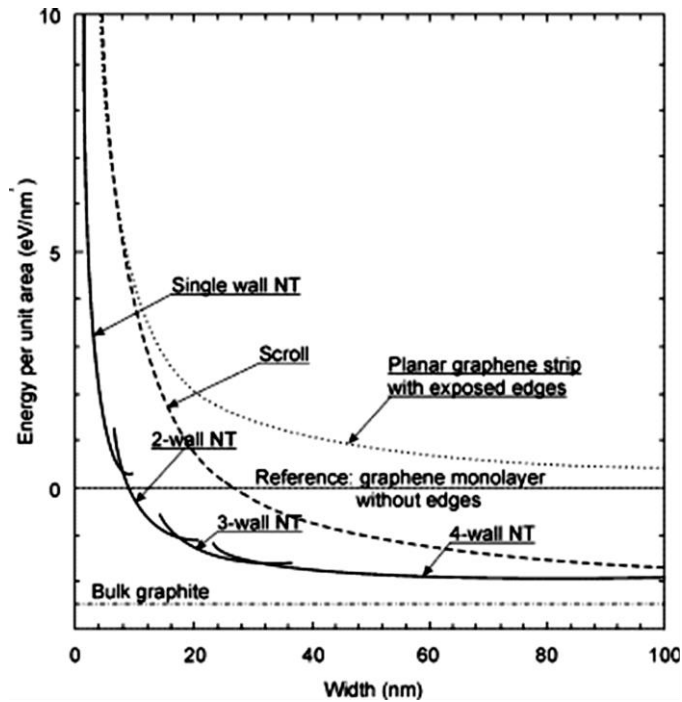


Figure 2.5 Plot of energy cost per unit area for converting graphene into nanotubes against the width (W) of graphene layer [46].

2.1.3 Experimental Techniques for Determining Properties of MWNTs

Both experimental and computational methods have been employed by different researchers worldwide to evaluate the mechanical properties of CNTs [4]. Experimental determination of mechanical properties with the methods employed at microscale has proven to be difficult at nanoscale [41]. One such method was to apply a controllable force on the specimen mounted at both ends using conventional extensometers provided the material's quantity is enough to be able to give it a shape of a rod [41,42]. Difficulty at handling the specimen at nanoscale resulted in the exploration of new experimental methods that measured thermal vibration amplitudes using transmission electron microscopy (TEM), force-displacement characteristics of the cantilevered or suspended nanotubes using atomic force microscopy (AFM), crystallographic parameters using X-ray diffraction, surface topography using scanning probe microscopy and internal structure using electron diffraction [46,47]. For studying MWNTs in particular, high-resolution transmission electron microscopy (HRTEM) is the most applied technique [46].

Treacy et al. [48] assessed the Young's modulus by determining the amplitude of the inherent thermally induced vibrations of 11 different MWNTs using TEM by varying the temperature from room temperature to 800 °C [42,48]. The average Young's modulus for MWNT was 1.8 TPa [48]. The technique employed by Treacy et al. [48] was also applied by Krishnan et al. [49] to estimate the Young's modulus of SWNTs of various diameters in the range of 1.0 to 1.5 nm. Krishnan et al. [49], however, observed vibrations at room temperature only using TEM and found an average Young's modulus of 1.25 TPa for SWNTs. A lower average value found by Krishnan et al. [49] for SWNT as compared to that of MWNTs found by Treacy et al. [48] was attributed to the systematic errors in length and temperature measurement hence no plausible conclusion as to which of the two is stiffer than the other could be drawn back then [49].

Such technique, however, has certain limitations. Firstly, for reliable results the excitation needs not to be either too small or too large thereby limiting the size, both diameter and length, of the sample. Secondly, the technique cannot measure the critical properties like toughness and strength of the nanotube [41]. Therefore, Wong et al. [41] presented a technique of directly measuring the bending force and the resulting displacement. This involved pinning one end of the MWNT to the flat surface of a low-friction-coefficient substrate and using AFM, they could directly measure the force-displacement at various points. They conducted the experiment with different diameters of MWNT ranging between 26 and 76 nm. MWNTs (which were affixed to the surface of molybdenum disulfide by one end) underwent elastic buckling when bent at large angles which compromises its ultimate strength but makes them tougher. The average Young's modulus with no diameter dependence ascertained was 1.28 ± 0.59 TPa which is equivalent to the in-plane modulus of the largest known bulk material, graphite, whose Young's modulus is 1.06 TPa. The average and maximum bending strength was determined to be equal to 14.2 ± 8.0 GPa, and 28.5 GPa, respectively [41].

Salvetat et al. [42] also employed AFM technique to evaluate the Young's modulus of eleven MWNTs grown by arc-discharge method. The average Young's modulus found was equal to 0.81 ± 0.41 TPa [42].

Uncertainties associated with experimental methods including imprecise measurement of the amplitude of the thermally induced vibration in case of TEM and effect of tip and calibration in case of AFM, made Poncharal et al. [47] explore another technique whereby MWNTs were made to resonate *in situ* in a TEM. They found that for smaller diameters (less than 10 nm) the Young's

modulus is quite large and is approximately equal to 1 TPa but for larger diameters it drops drastically to around 100 GPa. This reduction can be explained by the ripples that appear on the inner curve of the bent tube on the application of alternating potential, due to the decreased contraction of the carbon bonds in the inner curve which reduces the strain energy that is linked to the Young's modulus parallel to the basal plane of graphite [47].

Cooper et al. [50] determined the Young's modulus of MWNTs produced by arc discharge method by investigating effective Raman band shifts using Raman spectroscopy. They reported a value of 0.3 TPa [50].

Table 2.1 gives the precis of the experimental results on the mechanical properties of MWNTs available in literature

Table 2.1 Summary of the experimental published results of the Young's modulus (E) of MWNTs.

Reference	Year	Method	E (TPa)
Treacy et al. [48]	1996	Determined the amplitude of the intrinsic thermal vibrations of 11 different MWNTs using TEM	1.8 (0.40-4.15)
Wong et al. [41]	1997	Directly measured the bending force and the resulting displacement of MWNT (with diameters ranging between 26-76 nm) using AFM	1.28 ± 0.59
Salvetat et al. [42]	1999	Used AFM to measure the Young's Modulus of eleven MWNT synthesized by arc-discharge method	0.81 ± 0.41
Poncharal et al. [47]	1999	Used TEM where MWNTs were made to resonate <i>in situ</i>	1 (for diameters < 10 nm) 0.1 (for diameters > 10 nm)
Cooper et al. [50]	2001	Investigated effective Raman band shifts using Raman spectroscopy to observe deformation of arc-discharge produced MWNTs	0.3

As apparent from the experimental results, the error bars are quite significant which make it difficult to state anything about the characteristics of CNTs of different chirality and diameters with certainty [18]. Owing to the technological difficulties associated with the synthesis and handling of objects at nanoscale, theoretical studies outweigh the experimental ones both in terms of number and technological level. However, as pointed out by Cornell and Wille, the simulations are just a guide to better interpret the experiments and can thus in no way offer a complete substitute for them. But in addition to being difficult, experiments at nanoscale greatly affect the precision of the results thereby hampering the observations of second-order effects caused by the curvature and helicity of the tubes [42]. For this reason, computational modelling has become an

attractive tool for investigating nanomaterials timely and cost effectively [2,18]. The following section covers the details of the modelling techniques employed for the determination of the mechanical properties of carbon nanotubes.

2.1.4 Modelling Techniques for Simulating Individual Tubes of MWNTs

Prior to the introduction of powerful computers, structural, mechanical and thermal properties of infinite systems were investigated using analytical approximation techniques. Emergence of the powerful computers led to the widespread use of numerical simulation techniques of the finite systems [12].

Modelling can be generally categorized into: ‘bottom up’ approach or ‘top down’ approach [18]. The bottom up approach is commonly known as atomistic modelling, under which falls the classical molecular dynamics (MD), ab-initio, tight-binding molecular dynamics (TBMD) and density functional theory (DFT) [14,51].

Derived from Newton’s second Law of motion, classical molecular dynamics technique was the first of its kind to be used for simulating CNTs and its allotropes. It determines the properties of atoms and molecules by evaluating overall energy of a system of particles ensuing from differentiation of the inter-atomic potential functions [51]. The inter-atomic potentials, both bonded and non-bonded, are expressed in terms of force constants and the inter-atomic distances. The elastic behaviour is determined by application of small deformations [4].

Though molecular dynamics simulations reasonably predict the mechanical behaviour of CNTs under external forces, it is not preferable when computation of CNTs constituting large number of atoms is required since it takes considerable amount of time and computational resources [51]. Thus, it limits the size of CNT up to millions of atoms on shorter-than-micro-to-nanoseconds time scale [18]. It is also not justified to use MD when working with very light atoms and extremely low temperatures [12].

Ab-initio (or first principles [12]) technique is an accurate method which works from accurate solutions of the Schrödinger equation. Unlike MD technique, it obtains the atomic forces not from the potential functions but from progressive calculations of electronic structure [51]. Though ab-initio gives more precise results than MD, the former being computationally more intensive is

limited to small systems comprising of a few hundred atoms [18]. Among ab-initio, MD and TBMD, ab-initio is the most costly one [12].

Tight-binding molecular dynamics (TBMD) can be used to provide accurate structural, electronic and mechanical characteristics for a system comprising of up to a few thousand atoms. In terms of accuracy and computational cost, TBMD is in between MD and DFT [12].

DFT can provide extremely accurate, self-consistent electronic characteristics of a system of up to hundreds of atoms, otherwise it becomes computationally expensive [12].

Top down approach is based on continuum mechanics. To simulate larger and longer systems outside the range of ab initio and MD, continuum methods are currently being used [18]. Continuum mechanics modelling assumes that CNT has a continuous mass and stiffness distribution and thus can be modelled as a space truss/frame or cylindrical shell-like structure constituting continuum solid beam or shell that are subjected to tensile loading, bending moment and torsional moment [4,51,52]. The mechanical properties can be attained analytically using classical continuum mechanics or numerically using finite element method (FEM) [4,51]. Since the unequivocal lattice structure of CNT is disregarded by this assumption and the method is unable to take into account the forces acting on individual atoms, it is imperative to validate the findings obtained from continuum modelling approach [14,51]. To overcome the inaccuracy involved with continuum mechanics method, the required input data can be obtained by experiment or atomistic modelling [2].

2.1.5 Modelling Techniques for Simulating van der Waals Force

A good model for an MWNT should possess a good model for the vdW interactions between the atoms [52]. Researchers have used different techniques to simulate van der Waals interaction between the tubes of MWNT.

He et al. [52] computed the initial pressure P_{ij} due to the vdW interaction only from Lennard-Jones (L-J) potential using Equation (2.1).

$$P_{ij} = \left[\frac{2048\epsilon\sigma^{12}}{9a^4} \sum_{k=0}^5 \frac{(-1)^k}{2k+1} \binom{5}{k} E_{ij}^{12} - \frac{1024\epsilon\sigma^6}{9a^4} \sum_{k=0}^2 \frac{(-1)^k}{2k+1} \binom{2}{k} E_{ij}^6 \right] R_j \quad (2.1)$$

where $a = 0.142$ nm, R_j is the radius of the j th layer, i and j are the subscripts denoting the tube numbers, ε and σ are the Lennard Jones parameters and E_{ij}^m is the elliptical integral which is determined by Equation (2.2).

$$E_{ij}^m = (R_i + R_j)^{-m} \int_0^{\pi/2} \frac{d\theta}{[1 - K_{ij}(\cos \theta)^2]^{m/2}} \quad (2.2)$$

where m is an integer and K_{ij} is determined by Equation (2.3).

$$K_{ij} = \frac{4R_i R_j}{(R_i + R_j)^2} \quad (2.3)$$

Figure 2.6 shows the pressure interaction among the tubes of a 10-walled MWNT as found by He et al. [52] but for brevity only results for 4 tubes are shown. The figure shows that the vdW interactions are strongest between the adjacent tubes, any interaction among the remote tubes is thus negligible.

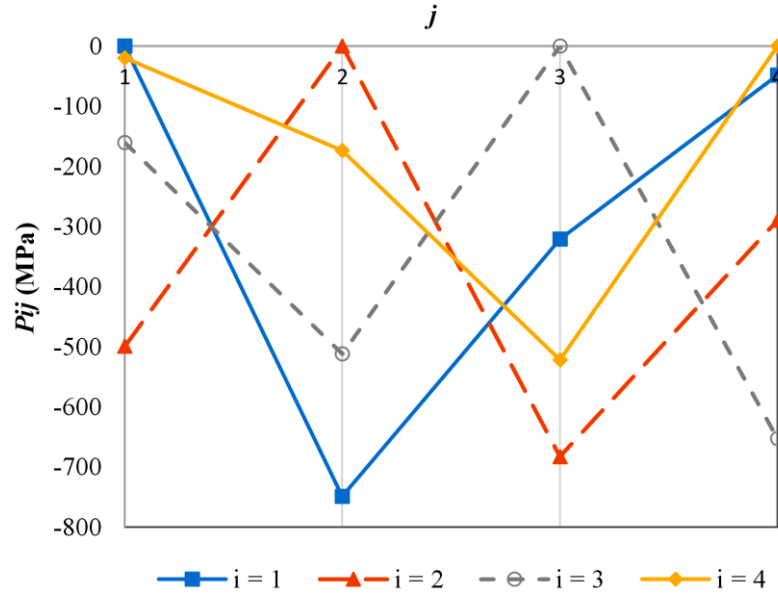


Figure 2.6 Initial pressure P_{ij} caused by van der Waals interaction between tubes i and j of a 10-walled MWNT with innermost radius = 0.68 nm, interlayer distance=0.34 nm, thickness of the tube=0.34 nm.

They also modelled the vdW force in a MWNT using an interaction coefficient c_{ij} .

$$c_{ij} = - \left[\frac{1001\pi\epsilon\sigma^{12}}{3a^4} E_{ij}^{13} - \frac{1120\pi\epsilon\sigma^6}{9a^4} E_{ij}^7 \right] R_{ij} \quad (2.4)$$

They found out that for a smaller inner radius ($r < 7$ nm), vdW interactions are radius-dependent but for larger inner radius, greater than 40 nm, the vdW is independent of the radius and takes up a constant value which differs between two different tubes [52].

Li and Chou [53] simulated the vdW interaction between the two interacting atoms on the neighbouring tubes of an MWNT based on the L-J “6-12” potential using a non-linear truss rod with rotatable end joints. A truss rod implies that the atoms can interact only by means of compression or tension. According to the criterion developed by Haile (1997), the van der Waals bonds are presumed to be active only when the distance between the interacting atoms on the adjacent tubes is lower than 2.5σ so no interactions are considered beyond this distance without incorporating any significant errors [53].

Figure 2.7 shows their normalized load-displacement curve for the truss rod. To analyse the stiffness behaviour from the non-linear curve, Li and Chou [53] employed generalized displacement control method which involves N number of displacements and one load parameter. N number of equations of equilibrium are obtained plus one constraint equation coming from the bounded nature of the load parameter. The stiffness parameter is then obtained iteratively with each load increment and updated displacements [53].

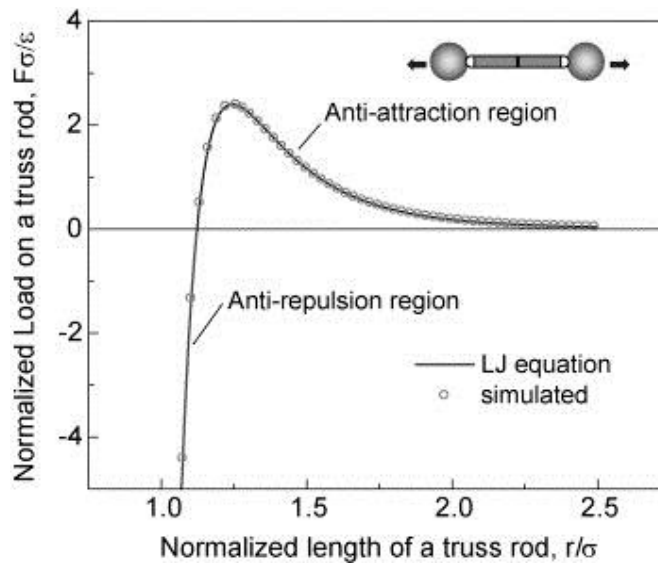


Figure 2.7 Normalized load-displacement curve for the non-linear truss rod [53].

The Young's modulus of MWNTs (by keeping the thickness and intershell spacing as 0.34 nm) was found to be around 1.05 ± 0.05 TPa which is a bit greater than that of SWNTs and shear modulus around 0.40 ± 0.05 TPa which is less than that of SWNTs [53].

The vdW force depends on the distance between the two interacting atoms on the different tubes of an MWNT [5]. On the application of the external force, interatomic distance between them changes [5]. Ghavamian et al. [5] thus used the force acting on the interacting atom to be the sum of the vdW force and the force ensuing from the deformation as a result of an applied load. They simulated the vdW force using a linear spring, being effective only in the domain 0.33-0.38 nm, with a stiffness value of $k = 0.24245$ N/m [5].

Ghavamian et al. [5] modelled the spring between the two interacting atoms on the adjacent tubes of MWNT in three stages as shown in Figure 2.8:

- a) In the first stage, the carbon atoms are hypothetically assumed to be at a certain distance apart where the total force acting on them is zero i.e. $F_T = 0$ (Figure 2.8a).
- b) In the second stage, the carbon atoms are not acted upon by any external force and thus are at an undeformed length apart i.e. $F_T = F_{L-J}$ (Figure 2.8b).
- c) In the last stage, the spring is loaded causing it to deform and change the distance between the atoms on the adjacent tubes. As a result, the L-J force between the two atoms is changed according to $F_T = F_{L-J} + k\Delta r$ (Figure 2.8c) [5].

where F_T is the total force and Δr is the displacement from the initial distance r_0 .

By applying fixed angular rotation at one end of the tube which is fixed from the other end, Ghavamian et al. [5] found out shear modulus in the range of 0.073 – 0.378 TPa for MWNTs with 2 to 5 tubes.

Rahmandoust and Ochsner [20] used the technique used by Li and Chou [14] to find out the properties of the thin elastic beam representing Carbon-Carbon covalent bond in the MWNT. They then represented the vdW interaction between the 2 tubes of a DWNT, by use of a spring element. Absence of any material between the tubes, makes the spring element the best element between the interacting atoms on different tubes. In order to deal with the fact that the spring

force is a function of displacement and the vdW force is the function of distance, they used a coordinate transformation to define a force intersect between the interacting atoms that are at an initial distance apart. Any change in their distance would alter the interacting force based on the force-displacement equation. They obtained the Young's modulus for armchair configuration to be ~ 1.05 TPa and for zigzag to be around 1.03 TPa. By using tension test and imposing isotropic conditions, they also determined the shear modulus for armchair and zigzag configurations which came around 0.448 TPa, and 0.424 TPa, respectively [20].

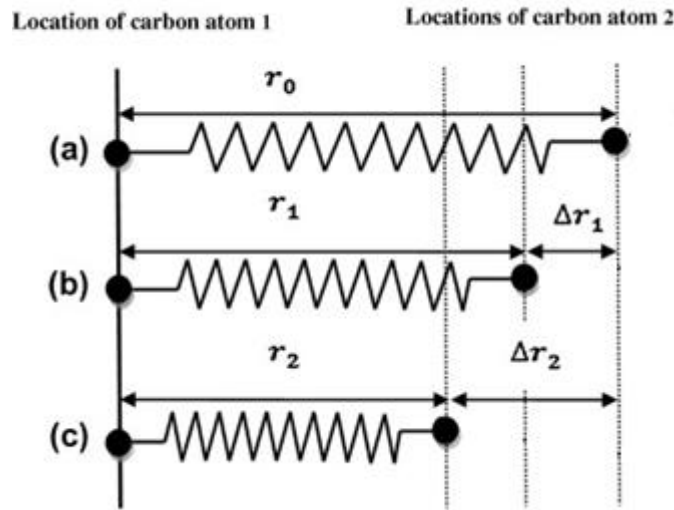


Figure 2.8 Spring modelling stages of Lennard-Jones Force [5].

Brcic et al. [15] used FEM to predict Young's and shear modulus of an armchair DWNT with the chirality of (10,10)-(15,15). They used 0.34 nm both as the interlayer spacing (\hat{d}_{002}) and as the thickness (t) of the wall. For the sake of saving computational cost, they disregarded vdW interactions between the two tubes in their study. To obtain Young's modulus, they applied an axial force of 5 nN at the free end of the cantilevered beam which is constrained by connecting the top nodes of each wall of the DWNT to the centrally positioned master node. They found the Young's modulus of 1.04 TPa and by subjecting the same beam to the torsional moment of 5 nN nm, they obtained the shear modulus of 0.418 TPa [15].

Fan et al. [4] used FEM by means of ANSYS software on the nested zig-zag type DWNT in their study with the chirality (9, 0)-(18, 0). They also used 0.34 nm as the interlayer spacing and the wall thickness. To avoid non-linearity in modelling vdW interaction, they used interlayer pressure

instead of van der Waals force and linearized it to model it using the spring element [4]. The interlayer pressure is a function of the interlayer distance (r) as given by Equation (2.5) [4].

$$p(r) = \frac{\psi}{6} \left[\left(\frac{\sigma}{r} \right)^{10} - \left(\frac{\sigma}{r} \right)^4 \right] \quad (2.5)$$

where the values of constants ψ and σ are 36.5 GPa, and 0.34 nm, respectively [4].

Figure 2.9 shows the relation of the interlayer pressure with the interlayer distance, using which they deduced that at some incremental distance away from the equilibrium position, the pressure variation is linear which can be rewritten using Equation (2.6) [4].

$$p(r) = -a_0(r - r_0) = -a_0\Delta r \quad (2.6)$$

where a_0 is the slope calculated as 107 GPa/nm [4].

The force equation was then obtained:

$$F_{vdW} = -(a_0\Delta r)A_{ave} \quad (2.7)$$

where A_{ave} is the average area of the two tubes.

The m number of spring elements that will simulate this force will take up the form:

$$F_s = -\frac{1}{m}(a_0\Delta r)A_{ave} = k_s\Delta r \quad (2.8)$$

where k_s is the spring stiffness taking the form:

$$k_s = \frac{1}{m}a_0A_{ave} \quad (2.9)$$

They obtained spring stiffness of 3.7 N/m with 27 spring elements between the tubes of diameter 0.704 nm and 1.408 nm each [4]. This stiffness value can be used for any sized DWNT since increasing the size would linearly increase the spring elements thereby keeping the stiffness value constant as long as the value of a_0 stays constant.

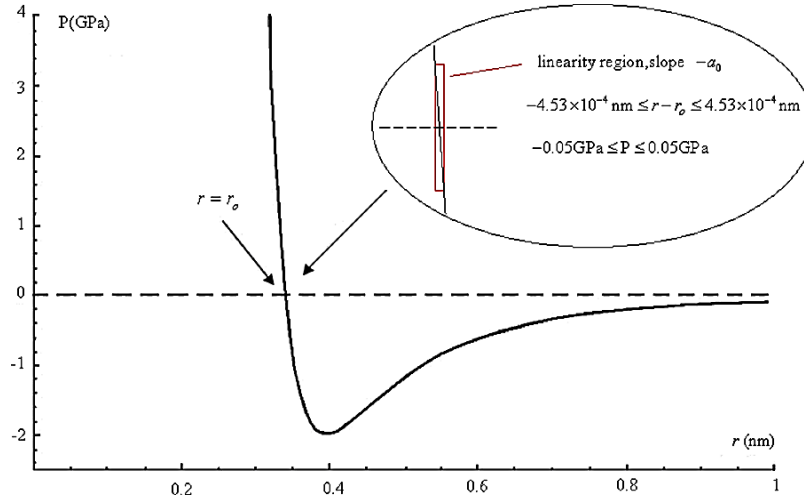


Figure 2.9 Variation of interlayer pressure with interlayer distance [4].

To determine the axial Young's modulus, they used three methods: The first two are numerical techniques while the last one is analytical [4].

1. By applying uniform tension at one end of the tube which is fixed at the other end, they determined stress/strain relationship to find out Young's modulus.
2. By applying three different uniform displacements at one end of the tube which is fixed at the other end, they determined the overall strain energy, that was presumably taken as parabolic, to ultimately find out axial Young's modulus by strain energy equation.
3. By treating the MWNT as the nested SWNTs and utilizing the Young's modulus of each SWNT in the equation from composite mechanics to attain the Young's modulus of the MWNT [4]:

$$E_a = \frac{E_o A_o + E_m A_m + E_i A_i}{A_o + A_m + A_i} \quad (2.10)$$

where E_o , E_m , and E_i are the axial Young's modulus of the outer SWNT, of the inner SWNT, and of the interlayer region (which is assumed to be negligible), respectively. Similarly, A_o , A_m and A_i are the cross-sectional area of the outer SWNT, inner SWNT and the interlayer region [4].

The axial Young's modulus for DWNT zigzag with all these methodologies came out to be around 1.0 TPa [4].

Fan et al. [4] also found the radial Young's modulus by employing method 2. They concluded that during pure tensile loading in radial direction, the DWNT's radial Young Modulus was nearly equivalent to that of the outer SWNT since the vdW bond being weak is unable to efficiently transfer the load from outer to the inner tube. Their radial Young's modulus also came out to be greater than the axial Young's modulus of MWNT which made them conclude that there is some anisotropy in CNTs [4]. Fan et al. [4] also found the shear modulus of the MWNT about 0.4 TPa.

Lu [54] studied the mechanical properties of MWNTs by making use of an empirical force-constant model. By keeping the interlayer distance as 0.34 nm, they chose the MWNT with the combination of $(5n, 5n)$ where n is the number of tube. Table 2.2 lists the properties Lu [54] found. From this and the properties found for SWNT, they concluded that the elastic moduli are not dependent on the number of tubes and share of inter-layer van der Waals interaction to the elastic moduli of MWNT is less than 10% [54].

Table 2.2 Properties of MWNT with n number of tubes as found by [54].

n	Young's Modulus (TPa)	Shear Modulus (TPa)	Bulk Modulus (TPa)
1	0.97	0.436	0.191
2	1.05	0.455	0.194
3	1.08	0.464	0.194
4	1.09	0.472	0.194
5	1.10	0.481	0.194
6	1.10	0.491	0.194
7	1.11	0.502	0.194
8	1.11	0.514	0.194
9	1.11	0.527	0.194
10	1.11	0.541	0.194
Average	1.083	0.488	0.194

Table 2.3 presents a precis of the literature results on the mechanical properties of MWNTs.

Table 2.3 Precise of the mechanical properties of MWNTs as reported in literature.

Reference	Year	Method	d_{002} (nm)	t (nm)	E (TPa)	G (TPa)
Li & Chou [53]	2003	Computational modelling with non-linear truss element Simulated vdW with LJ potential and modelled it by applying non-linear force on the truss rod	0.34	0.34	1.05 ± 0.05	0.40 ± 0.05
Ghavamian et al. [5]	2012	Computational modelling with 3D thin elastic beam element Simulated vdW with LJ potential and modelled it by spring elements of stiffness $k = 0.24245$ N/m Determined shear modulus by applying Torsion test	0.34	0.34	-	0.073–0.378
Rahmandoust et al. [20]	2012	Computational modelling of DWNT with 3D thin elastic beam element Simulated vdW with LJ potential and modelled it by non-linear spring elements Determined shear modulus by applying Tensile Test and imposing isotropic condition	0.34	0.34	~ 1.05 [Armchair] ~ 1.03 [Zigzag]	0.448 [Armchair] 0.424 [Zigzag]
Brcic et al. [15]	2009	Computational modelling of DWNT (10,10) - (15,15) with cantilevered beam. Disregarded vdW interaction	0.34	0.34	1.04	0.418
Fan et al. [4]	2009	Used FEM to model Zigzag DWNT. Modelled vdW using spring elements of stiffness 3.7 N/m	0.34	0.34	~ 1.0 [Zigzag]	~ 0.4 [Zigzag]
Lu [54]	1997	Used empirical force-constant model	0.34	-	1.083 (Average)	0.488 (Average)

2.2. Literature Review on CNTRPs

This section covers briefly the synthesis techniques of CNTRPs, the properties of the most prevalent polymer used in the CNTRPs that is the Epoxy resin, the experimental and computational techniques used to determine the mechanical properties of the CNTRPs, and lastly the reasons that limit their commercialization.

2.2.1. Synthesis of CNTRPs

The synthesis techniques for CNTRPs published so far are:

1. Solution Mixing
2. Melt blending
3. *In situ* polymerization

In solution mixing, nanotubes are spread in a solvent which is then added into a solution of polymer where they are mixed using any of the three techniques: mechanical mixing, magnetic agitation or high energy sonication. The solvent is thereafter vaporised to obtain the CNTRPs [30]. This technique helps achieve good dispersion of CNTs [25]. Epoxy resin, a thermosetting resin, is often added in CNTRPs by means of solution mixing [30].

For thermoplastic polymers, melt blending technique is employed. In this technique, the dispersal of CNTs in the polymer matrix is achieved by blending the nanotubes with melted polymer [30].

The most effective technique when it comes to best nanotube dispersion in the polymer and improved interaction between CNT and polymer is *in situ* polymerization. Herein, nanotubes are first put together with the monomers which undergo polymerization later at certain conditions [30].

2.2.2. Nanotube-Reinforced Epoxy Composites

Thermoset polymers have massive industrial applications today ranging from coatings to matrix in the fibre reinforced polymer composite [55]. The most prevalent thermoset polymer in industrial use today is the epoxy resin since it possesses relatively high tensile strength, elastic modulus and good adhesive properties, undergoes little shrinkage during curing, and is resistant to chemicals and corrosion [55,56]. Also, epoxy resins exhibit strong level of adhesion with most of the surfaces except a few non-polar ones [35]. Developments in composite manufacturing in the form of large complex composites led to the use of polymer adhesives like epoxy to join the various parts. Adhesive bonds are cost effective and easy to process, they also have high strength-to-weight ratio, fatigue resistance and minimal stress build up at joints [57]. From the sustainability standpoint, epoxy resins' light weight can help reduce material consumption and its importance as a sustainable polymer is manifested further by the fact that in spite of the presence of a volatile solvent in it, it still does not emit any volatile emissions upon curing [35]. In structural applications, neat epoxy resin has a drawback of being brittle which can be compensated by the addition of nanotubes [55]. Nanotube-reinforced epoxy composites have demonstrated an

increase in ultimate strength and modulus by 30 to 70 percent, increased strain-to-failure (which is otherwise lower in the epoxy resin itself [56]) and thereby toughness by a mere weight addition of 1 to 4 percent of functionalized SWNT [58]. Therefore, epoxy resin is regarded as the standard of performance for the polymer matrix in a composite [24].

2.2.3. Experimental Results on the properties of CNTRPs

Lu [59] prepared a MWNT/epoxy composite that comprised of highly disoriented CVD prepared MWNTs with the diameters ranging between 15 to 400 nm and a hardened epoxy resin that is ductile unlike the resins used before. They concluded that adding MWNTs 1 percent by weight doubled the composite's Young's modulus and yield strength whereas adding 4 percent by weight quadrupled the properties [59]. Table 2.4 shows the results [59] reported.

Cristina et al. [24] prepared a MWNT/epoxy composite reinforced with 2 percent of MWNTs that was functionalized with carboxylic group and had the diameter of 5 nm and length 5-15 micrometer. The epoxy resin used was P401. The Young's modulus they reported for this composite and the neat epoxy resin were 3.42 GPa, and 2.8 GPa, respectively. They also reported the tensile strength of the MWNT/epoxy composite made of 2% MWNT to be equal to 98 MPa [24]. They concluded that by adding 2% of MWNTs in the composite, mechanical strength and Young's modulus improved by 15-17% and 20-25 % respectively.

Du et al. [30] reported the results obtained by Ying et al. [60]. Ying et al. [60] prepared a MWNT/epoxy composite reinforced with 2 wt.% of MWNT. They tested the Young's modulus of the CNTRP made of treated and untreated MWNTs. For treated MWNTs they reported the Young's modulus of around 1.3 GPa and for untreated MWNTs they found out the value of 1.18 GPa which is same as the Young's modulus of neat epoxy resin.

Cooper et al. [50] evaluated the effective Young's modulus of the MWNT/epoxy composite made of the arc-discharge produced MWNT and LY5052 epoxy resin with HY5052 hardener and found it to be 60 GPa. They investigated effective Raman band shifts using Raman spectroscopy to arrive at the value of 0.3 TPa for the Young's modulus of MWNTs and thereafter using the similar technique they found the Young's modulus of the composite [50].

Table 2.4 Young's modulus of pure epoxy resin and CNTRP epoxy composite containing 1 and 4 % by weight of MWNT respectively [59].

MWNT wt. %	Young's modulus (GPa)
0	0.118
1	0.236
4	0.465

Montazeri et al. [61] used the tensile test to examine the mechanical properties of the MWNT/epoxy composites reinforced with untreated and acid treated MWNTs, having the average length of 8.5 μm and 2 μm respectively and same diameter of 20 nm. The resin used was Ly564 epoxy resin with Hy560 hardener. Table 2.6 tabulates the results [61] obtained for the addition of 0, 0.1, 0.5, 1.0, 1.5, 2 and 3 wt. % MWNTs. On average the Young's modulus of the untreated MWNT/epoxy composites yielded a value of 3.97 GPa which is greater than the composite reinforced with treated MWNT whose Young's modulus came out as 3.89 GPa. This can be attributed to the ability of agglomeration of the untreated MWNT which provides higher filler loading [61]. Table 2.5 tabulates their results.

Table 2.5 Young's modulus of the MWNT/epoxy composite reinforced with 0, 0.1, 0.5, 1.0, 1.5, 2 and 3 wt. % MWNTs as reported by [61].

MWNT wt. %	Young's modulus (GPa)	
	Untreated	Acid-treated
0.0	3.43	-
0.1	3.458	3.465
0.5	3.705	3.680
1.0	3.951	3.860
1.5	4.138	4.050
2.0	4.225	4.100
3.0	4.365	4.200
Average	3.974	3.893

Table 2.6 summarizes the experimental studies done on investigating the mechanical properties of MWNT/epoxy composites.

Table 2.6 Summary of the experimental results of MWNT/epoxy composites available in literature (E_m and E_c refer to the Young's modulus of polymer matrix and composite respectively).

Reference	Year	Method	E_m (GPa)	E_c (GPa)	% increase
Lu [59]	2002	Prepared a MWNT/epoxy composite MWNTs with the diameters ranging between 15 to 400 nm were synthesized using CVD Epoxy resin was hardened	0.118	0.236 [1 wt. %] 0.465 [4 wt. %]	100 % [1 wt. %] 300 % [4 wt. %]
Cristina et al. [24]	2012	Prepared a MWNT/epoxy composite MWNT were functionalized with carboxylic group The diameter of MWNT was 5 nm and length 5-15 μ m	2.8	3.42 [2 wt. %]	22 % [2 wt. %]
Ying et al. [60] (Taken from Du et al. [30])	2002	Prepared MWNT/epoxy composite with 2 wt. % of MWNT MWNT samples were treated with different solutions	1.18	1.18 [untreated MWNTs] ~ 1.3 [Treated MWNTs]	10 % [Treated MWNTs]
Cooper et al [50]	2001	Investigated effective Raman band shifts using Raman spectroscopy MWNTs were synthesized by Arc discharge 50 % volume by fraction of 0.3 TPa modulus MWNTs	-	60	-
Montazeri et al. [61]	2010	Used tensile test to examine the mechanical properties of the MWNT/epoxy composites Untreated and acid treated MWNTs were used having the average length of 8.5 μ m and 2 μ m respectively and same diameter of 20 nm.	3.43	3.974 [Untreated] 3.893 [Treated]	15 % [Untreated MWNTs] 13 % [Treated MWNTs]

2.2.4. Modelling Techniques for Simulating CNTRPs

As the experimental published results on CNTRPs are highly varied, it is important to characterize its mechanical properties by means of computational modelling. In order to completely reveal the engineering potential of CNTRPs, computational modelling plays an utmost important role in characterisation of the mechanical properties [62]. Not much literature is available on the subject of mechanical properties of CNTRPs using modelling techniques and what is available, mostly covers SWNT based polymer composites [63]. This research will be dedicated to predict the mechanical properties of MWNT/epoxy composites.

Ayatollahi et al. [64] used the continuum modelling approach to build a cylindrical representative volume element (RVE) of the composite reinforced with SWNT for studying the effect of interface characteristics on the properties of RVE under tension, bending moment and torsional load. They concluded that high stiffness of the interface would minimally affect the axial stiffness but would maximally affect the composite's bending stiffness [64].

Zuberi and Esat [28] modelled CNTRPs using both the perfect bonding and non-bonding interactions to investigate the mechanical properties of SWNT/epoxy composite using finite element modelling. Both the models presented more or less the same results so for the sake of simplicity they chose the perfect bonding model to examine the effects of different configurations of SWNT in terms of chirality and size on its properties [28].

Karimzadeh et al. [65] modelled CNTRPs by employing the discrete finite element modelling approach to investigate the impact and post-impact behaviour of SWNT composites. They modelled the interface region using non-linear spring elements characterized by L-J potential. They concluded that the addition of 5% by volume of CNT in the polymer tremendously improved the impact resistance of the composite [29].

Joshi and Upadhyay [29] evaluated the elastic properties of range of different polymer matrix reinforced with MWNTs using a 3D cylindrical RVE based on continuum modelling. They used finite element method and validated their numerical results by rule of mixtures. They used two kinds of RVEs, one with a long MWNT whose length was same as that of the polymer matrix and the other a small one whose length for shorter than the matrix. Longer MWNT proved to be a better reinforcement than shorter [29]. The numerical results for tensile axial loading for different moduli of the matrix (E_m) obtained by them are tabularized in Table 2.7:

Table 2.7 Simulation results of the Young's moduli of the composite (E_c) and its Poisson's ratio against different moduli of the matrix (E_m) [29].

E_f/E_m	E_c/E_m	ν
5	1.072	0.279
7	1.149	0.279
10	1.264	0.280
15	1.456	0.284
50	2.803	0.284
100	4.727	0.287
150	6.651	0.298
200	8.575	0.300

2.2.5. Modelling the Interphase Region

The critical issue that governs the efficiency of CNTRPs at microscale is the load transferring phenomenon from the polymer to the nanotubes that is achieved through an interface [65]. The interface region between the polymer matrix and the embedded fibre is the one whose properties differ from the host polymer matrix [64]. The exact properties of this region are unavailable since the experimentation at nano-scale is quite demanding and no other technique exists as yet to determine its properties [64,66]. The outer radius of this region is thus unknown and have been arbitrarily chosen by the researchers ranging between 1 to 9 times the radius of the embedded CNT [64]. As for the stiffness behaviour of this region, Ayatollahi et al. [64] examined the effect of three different Young's moduli of the interface region, 0.2, 2 and 20 GPa, on the composite behaviour and concluded that 20 GPa minimally affected the axial stiffness of the composite, hence Zuberi and Esat [28] picked this value which has also been used in this study.

2.2.6. Challenges in Commercializing CNTRPs

CNTRPs have failed to commercialize in the market today, albeit the appreciable amount of research that has been dedicated to CNTs and CNTRPs [31]. The failure to do so has been attributed to the following factors:

- Tendency of CNTs to agglomeration causing difficulty in their dispersal in the polymer matrix
- Weak bonding at the CNT-matrix interface causing fracture at the very interface
- Difficulty in orienting the tubes in the polymer matrix
- Telescopic motion of the tubes of MWNT causing them to slide past each other on the application of a load
- The length of the CNTs has to be greater than the critical length $l_c = \sigma_f d / 2\tau_c$ where σ_f is the ultimate tensile strength of the fibre, d is the diameter of the fibre and τ_c is the strength of the bond between the fibre and the matrix. However, commercially available CNTs are within 100 nm to some microns only.
- CNTs' use as a filler in the polymeric composites is also hindered due to its cost. In addition to the synthesis techniques that are expensive per se, high purity and defect-free nanotubes require processing which adds to the cost [31].

- CNTs manufactured from the same technique differ in properties like their morphology, aspect ratio, mechanical properties etc. and often contain impurities that are difficult to completely remove [30].

Extensive studies are being done in order to address these issues. The problem of dispersion is expected to be resolved by making use of different solvents or by means of sonication of the suspension of nanotubes in the solvent. Similarly, for enhancing the bond between the nanotube and the matrix, surface treatments are done on the nanotubes or by its functionalizing. Likewise, inter-tube slipping has been controlled to an extent by means of reduced pressure catalytic CVD technique which produces CNTs as coils. It is anticipated that current research underway will positively tackle the aforementioned issues [31].

2.3. Gaps in the Literature

Results obtained by experiments on the mechanical properties of both MWNTs and CNTRPs are highly varied with great uncertainties and thus it cannot be stated with certainty how they can be of use in the structural applications. Almost all the work that has been done on the modelling of MWNT have used 0.34 nm as the intershell spacing. Unlike the models reported in literature, this study considers the variation of intershell spacing with varying inner diameters. Similarly, the literature has so far neither reported any results for the chiral configuration of MWNT nor examined any comparison between polychiral and monochiral configurations. This study determines the mechanical properties of MWNTs with various chiralities by considering both polychiral and monochiral configurations.

Also, unlike the composites of SWNT, there is paucity in the previous studies on the mechanical properties of MWNT reinforced polymer composites based on computational modelling that makes this study a relevant contribution to the literature.

CHAPTER 3

FINITE ELEMENT MODELLING OF MULTI-WALLED CARBON NANOTUBES

Since Middle East Technical University has the licensed version of the software MSC Marc Mentat 2013, it has been employed to model and simulate multi-walled carbon nanotube. It is a multi-physics software for simulating both static and dynamics problems with the aid of finite element analysis [67]. Finite element modelling of MWNTs is accomplished in two stages. The first stage encompasses simulation of each tube in an MWNT whereas the second deals with the interaction between the adjacent tubes. The following sections explain both the stages in detail.

3.1. Simulation of SWNTs

Each tube in an MWNT is treated as an individual SWNT. SWNT is entirely made of carbon atoms which are bonded together by means of covalent bonds forming a hexagonal array [53]. Because of structural similarity, CNTs can be modelled as a space-frame structure, whose connecting beam elements and joints represent the Carbon-Carbon bond and carbon atoms respectively [4]. Figure 3.1 shows the simulation of a SWNT that has been enlarged to show the hexagon made of beam elements representing C-C bonds and its joints denoting carbon atoms.

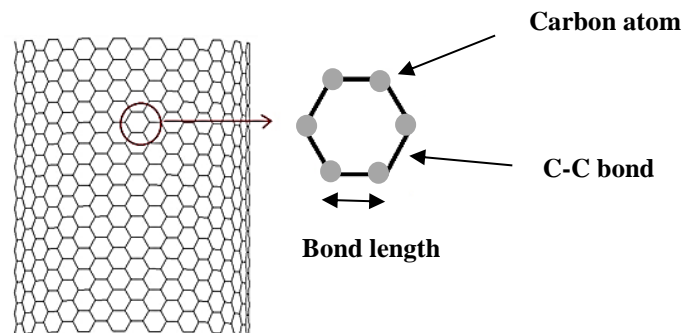


Figure 3.1 Simulation of a SWNT as a space-frame structure with its beams and joints representing carbon-carbon bonds and carbon atoms respectively.

3.1.1. Equivalent Continuum Modelling

Equivalent-continuum modelling (ECM) was developed from continuum mechanics modelling [18]. For the purpose of determining the macroscopic properties of CNTs like Young's modulus, Poisson's ratio and strength, it was important to address the issue of the difference in the length scales between modelling bulk properties at macroscopic scale and designing nano-structured materials on molecular level at nanoscale. Solid mechanics and computational chemistry, the two already developed and widely used models, can reliably model and predict macroscopic, and molecular properties, respectively, but a model at intermediate length scale did not exist. ECM helps bridge the gap where molecular mechanics approach is first used to determine the molecular properties that are then utilised to obtain the bulk mechanical properties at macroscopic scale by developing an equivalent continuum model [68]. It is considered an efficient method and has been used by many researchers over the past few years [18].

3.1.1.1. Molecular Mechanics

Molecular Mechanics (MM) is a way of modelling bonded atoms whose idealized geometry has been distorted. The distortion occurs when the bonds undergo stretching, bending and torsion and also when the non-bonded atoms interact by means of van der Waals interaction and Coulombic interaction [69]. From molecular mechanics' point of view, CNT is a large molecule that comprises many carbon atoms whose motions are governed by a force field. This force field is usually expressed by the steric potential energy [14].

The potential energy of a molecule using molecular mechanics is a function of energy coming from all factors contributing to the distortion as given by Equation (3.1) [14].

$$U = U_R + U_\theta + U_\phi + U_\omega + U_{vdW} + U_{el} \quad (3.1)$$

where U_R , U_θ , U_ϕ , U_ω , U_{vdW} and U_{el} are the energy due to bond stretching, bond angle bending, dihedral angle torsion, out-of-plane torsion (bond inversion), van der Waals interaction, and Coulombic (or electrostatic) interaction, respectively [70]. Figure 3.2 illustrates the diagrammatic representation of these interactions.

The bonded interactions (first four terms of Equation (3.1)) are the main contributors to the overall steric potential energy for covalent structures [71]. By assuming small deformation, it is sufficient

to use among the various energy forms the simple harmonic representation of the energies [4,14]. The simplest harmonic representation of each of these energies is given by Equation (3.2) [14]. Since both out-of-plane and dihedral torsion involve torsional deformation, they have been merged for the sake of simplicity as U_τ [14]:

$$U_R = \frac{1}{2}k_r(\Delta r)^2 \qquad U_\theta = \frac{1}{2}k_\theta(\Delta\theta)^2 \qquad U_\tau = \frac{1}{2}k_\tau(\Delta\phi)^2 \qquad (3.2)$$

where k_r , k_θ and k_τ are the force constants of bond stretching, bending, and torsional resistance, respectively, and Δr , $\Delta\theta$, and $\Delta\phi$ are the change in bond length as result of stretching, change in the bond angle as a result of bending and change in the bond angle as a result of twisting, respectively [71].

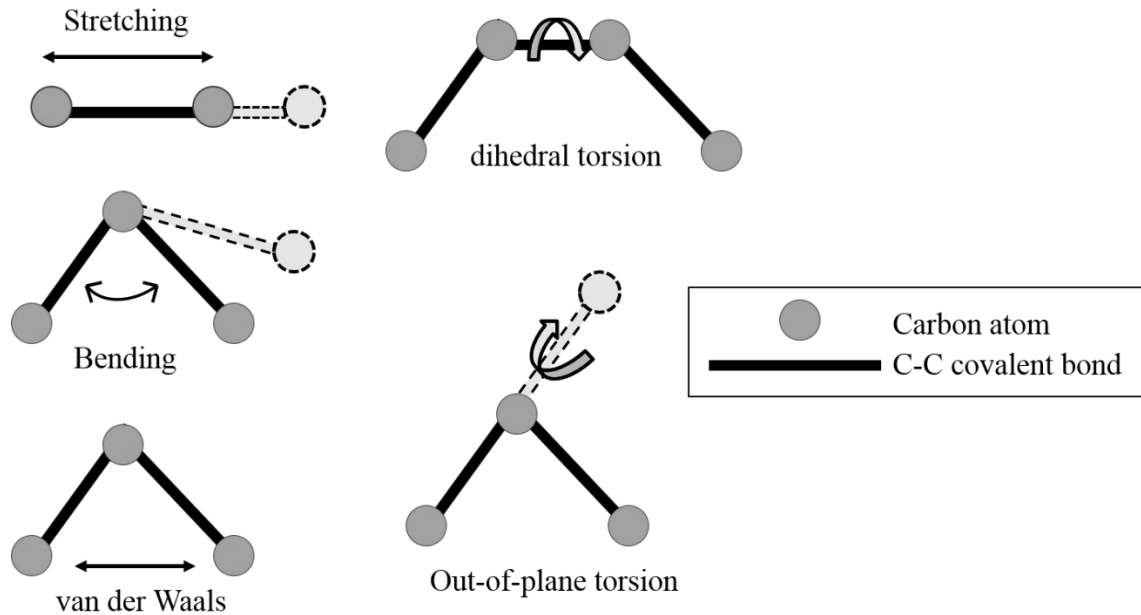


Figure 3.2 Illustration of interatomic interactions in molecular mechanics.

3.1.1.2. Structural Mechanics

By means of structural mechanics analysis, under given loading conditions, displacements, strains and stresses of a given structural element can be determined [14]. Because of structural similarity, carbon nanotubes can be represented by a space-frame structure with their bonds represented by a beam of characteristic bond length and bond angle and carbon atoms represented by the joints

[4,14,15]. By assuming that each C-C bond in the nanotube can behave as a three-dimensional beam capable of stretching, bending and twisting, it can be represented by an isotropic beam element of length L ($L = 0.142$ nm), circular cross-sectional area (A) and thickness (d) [15,72]. According to the classical theory of structural mechanics, the strain energy of this beam under the influence of an axial force (N), pure bending moment (M) or pure torsional moment (T) (see Figure 3.3) can be written as given by Equation (3.3) [14,15]:

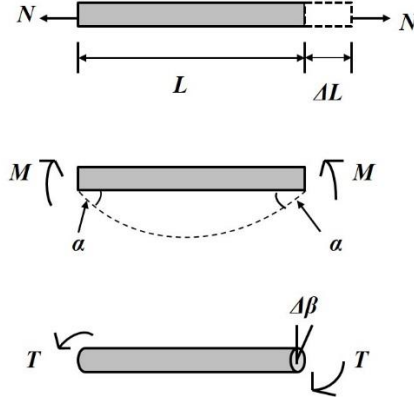


Figure 3.3 Illustration of a uniform beam under pure tension, bending moment and Torsion moment.

$$U_N = \frac{1}{2} \frac{EA}{L} (\Delta L)^2 \quad U_M = \frac{1}{2} \frac{EI}{L} (2\alpha)^2 \quad U_T = \frac{1}{2} \frac{GJ}{L} (\Delta\beta)^2 \quad (3.3)$$

where ΔL is the displacement in axial direction, 2α is the variation in rotation angle (bond angle variation), and $\Delta\beta$ is the twist angle, E and G are the mechanical properties, namely, equivalent Young's and shear Moduli, respectively, and A , J and I are the geometric properties namely; area of cross section, polar and area moment of inertias, respectively, given by Equation (3.4): [15].

$$A = \frac{\pi}{4} d^2 \quad I = \frac{\pi}{64} d^4 \quad J = \frac{\pi}{32} d^4 \quad (3.4)$$

3.1.1.3. Interrelationship between Molecular and Structural Mechanics

In order to determine the cross sectional properties of the beam elements, Odegard et al. [68] established a link between the microscopic computational chemistry and macroscopic structural mechanics. By applying energy equivalence between the potential energy due to tension, bending and torsional moment from molecular mechanics point of view (Equation (3.2)) with their respective strain energies from structural mechanics' standpoint (Equation (3.3)), direct

relationship between the cross-sectional properties of the beam element (tensile resistance (EA), flexural rigidity (EI), torsional stiffness (GJ)), and the molecular force field constants (k_r , k_θ and k_τ) is established as given by Equation (3.5) [4,14]:

$$k_r = \frac{EA}{L} \qquad k_\theta = \frac{EI}{L} \qquad k_\tau = \frac{GJ}{L} \qquad (3.5)$$

Equation (3.5) provides the foundation for the modelling of carbon nanotubes like a frame structure with beam elements [14,15]. The structural mechanics' parameters can be determined if the force constants are known. Using these force constants and the stiffness matrix method for frame structures, the elastic behaviour of the carbon nanotubes can then be analysed [14]. Li and Chou [14] were among the first few who used this technique and verified it by applying it on graphite. The force constants as adopted by them are [15]:

$$k_r = 652 \text{ nN/nm} \qquad k_\theta = 0.876 \text{ nN}\cdot\text{nm/rad}^2 \qquad k_\tau = 0.278 \text{ nN}\cdot\text{nm/rad}^2$$

It is noted that to obtain the torsional rigidity, it was assumed by Li and Chou [14] that U_τ is a function of dihedral torsion since it contributes the most to the torsional deformation [14]. However, by equating U_τ and U_T an error is introduced when the parameter k_τ reflects the effect of out-of-plane torsion [14]. But since Li and Chou [14] proved that k_τ negligibly influenced the Young's modulus, the authors believed that the error induced was negligible. However, by neglecting out-of-plane torsion, Li and Chou [14] did not properly address the bending resistance of SWNT [18].

When Fan et al. [4] used the approach by Li and Chou [14], irrespective of the values of k_τ , they always obtained Poisson's ratio more than 0.5, which is the violation of the isotropic elasticity theory [4].

Tserpes and Papanikos [71] also used the approach by Li and Chou [14] and determined a unique bond diameter (wall thickness) equal to $d = 0.147$ nm that is almost equal to the C-C covalent bond length of 0.142 nm. If isotropy is imposed from $E = 5.49$ TPa and $G = 871$ GPa found by Tserpes and Papanikos [71], Poisson's ratio obtained is 2.15 which is only possible in case of an anisotropic material [72]. This supports the argument that equating U_τ and U_T is flawed for the standard beam element used [4].

Therefore, Scarpa and Adhikari [72] adopted a different methodology. They equated U_R and U_N and imposed an equivalence between U_θ and U_T to arrive at the expressions for Young's and shear Modulus that are given by Equation (3.6) and Equation (3.7) respectively.

$$E = \frac{4k_r L}{\pi d^2} \quad (3.6)$$

$$G = \frac{32k_\theta L}{\pi d^4} \quad (3.7)$$

It is noted that the expression obtained for k_θ in Equation (3.5) is valid for slender uniform beams subjected to pure bending. For (deep) thick beams, in order to accurately estimate the beam deflection, it is essential to consider the shear deformation of the cross-sectional area under bending [16,72].

Scarpa and Adhikari [72] also incorporated the effect of Poisson's ratio and shear deformation of the cross-section of a thick beam under bending. While Li and Chou [14] used thickness d of the circular beam (the bond diameter of the Carbon-Carbon bond in CNTs) same as the interplanar spacing of graphite that is 0.34 nm, Scarpa and Adhikari [72] imposed the condition of an isotropic material by incorporating the correlation $G = E/2(1 + \nu)$ to obtain the cross-sectional parameters of the beam [16] tabulated in Table 3.1 that have been used by Zuberi and Esat [67] and also in this study.

Table 3.1 Cross-Sectional properties of the circular beam element used for modelling C-C bond, taken from [72].

Bond Length (L)	Bond Diameter (d)	Young's Modulus (E)	Shear Modulus (G)	Poisson's ratio (ν)
0.142 nm	0.0844 nm	16.71 TPa	8.08 TPa	0.034

To simulate the C-C bonds in a layer of an MWNT, a 3D beam element of Type 98 has been used as employed by Zuberi and Esat [67]. Every node of the said straight beam element has six degrees of freedom, three being rotational about x , y , and z axes and three being translational on x , y , and z axes [67]. The element can demonstrate not only linear and nonlinear elastic material behaviour but can also depict inelastic behaviour including the effect of transverse shear [73].

Figure 3.4 shows the simulated single tube of an MWNT of the zigzag configuration (16, 0) modelled with the 3D beam element of Type 98 of the aforementioned properties.

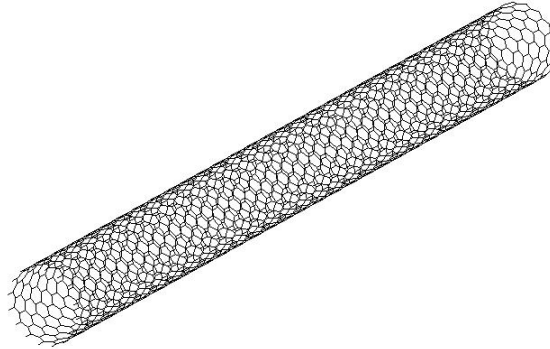


Figure 3.4 Simulation of a single tube of MWNT with zigzag configuration (16, 0).

3.2. Simulation of vdW Interaction Between Adjacent Tubes

Though, it is established that the C-C bonds within each tube of an MWNT is covalent, there is no unanimous agreement on the type of bonding among the atoms on adjacent tubes. The commonly agreed bonding type is the weak van der Waals force of interaction which arises due to the dipole-dipole interaction that is ensued from the motion of the delocalized electrons [74].

Van der Waals force is neglected when simulating SWNTs since it is between the non-bonded atoms hence are weaker than the covalent bonds [4,15]. On the other hand, when modelling MWNTs it becomes critical to incorporate the interaction between the tubes in MWNT [4]. But some researchers choose not to introduce these bonds in the model since it increases the computational cost substantially [15]. However, according to He et al. [52], vdW are significant at molecular level and hence should not be neglected.

Since vdW force comes into effect when the interacting atoms are within an effective range of distance, it is imperative to find out the intershell spacing that is the distance between the two adjacent tubes. Section 3.2.1 explains this in depth.

3.2.1. Intershell Spacing of MWNTs

Many researchers have used different techniques to determine the intershell spacing of MWNTs. Iijima and Zhang *et al.* using TEM and ED techniques respectively found the spacing to be about 0.34 nm. Saito *et al.* using X-ray diffraction found the average intershell spacing to be equal to 0.344 nm. Bretz *et al.* and Sun *et al.* employed high resolution transmission electron microscopy (HRTEM) and found 0.375 nm and 0.36 nm respectively [75].

Kiang *et al.* [75] digitally analyzed images from HRTEM to obtain not only the intershell spacing but also its dependence on the diameter and number of tubes of the MWNT [75]. They obtained an empirical relationship between inner tube diameter (d_i) in nm and the intershell spacing (\hat{d}_{002}) (also in nm) as given by Equation (3.8):

$$\hat{d}_{002} = 0.344 + 0.1e^{-d_i/2} \quad (3.8)$$

According to this relationship, the spacing decreases with an increase in the diameter. Figure 3.5 shows the graph demonstrating the relationship between average diameter and intershell spacing. For diameters up to around 10 nm, the spacing decreases exponentially with increasing diameter. This is because smaller diameters have larger curvatures which offer greater repulsion against the adjacent tubes, perturbing the geometric and electronic structure of the nanotube as compared to the planar graphene sheet. The graph attains an asymptotic value after ~10 nm which corresponds to the spacing of 0.344 nm which is same as the spacing in graphite. This can be expected in a defect-free MWNT which has circular cross-section. Smaller innermost diameter nanotubes have a few number of shells owing to the low stability associated with the growth of small diameter tubules. The effect of number of shells (n) on the intershell spacing was concluded to be the result of experimental uncertainties since intershell spacing as a function of number of shells would imply changes in the bond length of C-C bond which is not possible [75].

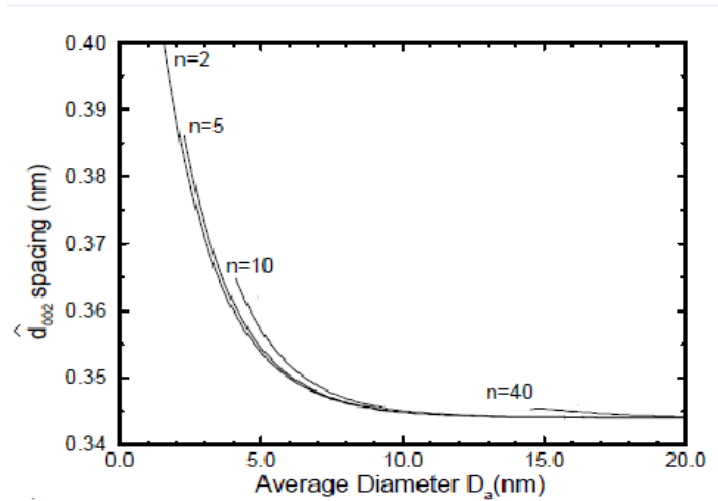


Figure 3.5 Plot of intershell spacing versus average diameter of a MWNT with different number of shells [75].

3.2.2. Lennard-Jones Force

Van der Waals (vdW) force between the adjacent tubes of MWNT is both attractive and repulsive in nature; attractive when the approaching atoms are at a certain distance apart and repulsive when the two interacting atoms are at a distance less than sum of their radii [15,52]. Lennard-Jones (L-J) “6-12” potential, as given by Equation (3.9), models the smooth switch from repulsive to attractive force [15,52] and hence can effectively elucidate the non-covalent interaction between the tubes [20]:

$$U_{L-J} = 4\varepsilon \left[\left(\frac{\sigma}{r} \right)^{12} - \left(\frac{\sigma}{r} \right)^6 \right] \quad (3.9)$$

where r is the inter-atomic distance, ε and σ are the L-J constants which depend on the material and the inherent strength and type of the interaction between the interacting atoms [20]. In the case of carbon-carbon non-bonded interaction, the values of ε and σ are 0.4396 kJ/mol ($0.072997284 \times 10^{-20}$ J) and 0.3851 nm respectively [20,70,76]. By definition, σ is the inter atomic distance when the interatomic potential becomes nil and ε is the minimum potential between them [20].

Figure 3.6 shows the Lennard-Jones potential for carbon-carbon non-bonded interaction. Increasing the distance between the interacting particles up to an inter-atomic potential of ε leads

to reduction in the potential which reaches zero at an inter-atomic distance of σ and thereafter attains a negative value. After attaining the minimum potential ε , the potential increases on further increasing the distance.

The vdW force acting on the interacting particles can be obtained by differentiating U_{L-J} with respect to r as shown in Equation (3.10) [9]:

$$F_{L-J} = -\frac{dU(r)}{dr} = 4\varepsilon \left[12 \left(\frac{\sigma}{r} \right)^{12} - 6 \left(\frac{\sigma}{r} \right)^6 \right] \quad (3.10)$$

Figure 3.7 shows the plot of Lennard-Jones force against the interatomic distance. The atoms are subjected to repulsion up to a critical distance $r_0 = \sqrt[6]{2}\sigma = 0.43266$ nm which is the interatomic distance when the force between the interacting atoms becomes nil [20]. Beyond r_0 the atoms are mildly attracted to each other [20]. As shown in the figure, the attractive forces are negative whereas the repulsive forces are positive.

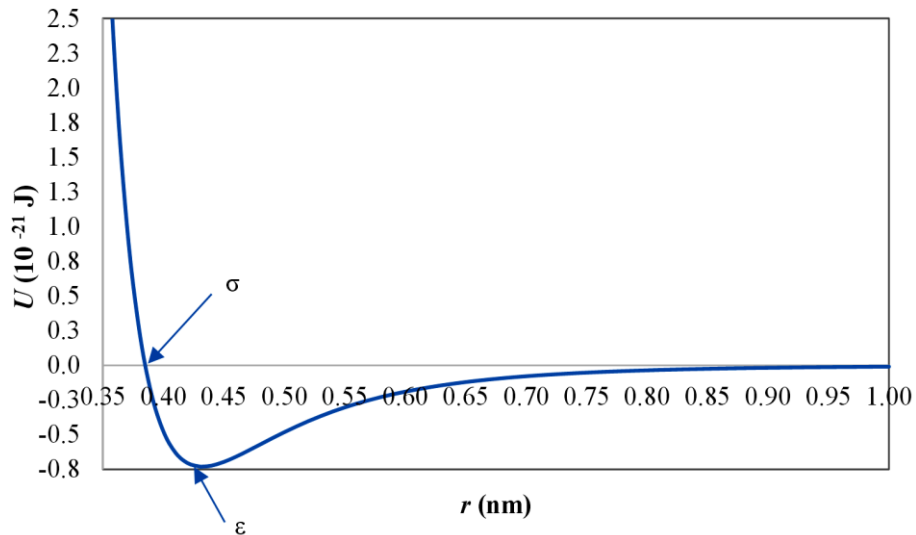


Figure 3.6 Plot of Lennard-Jones potential versus the interatomic distance.

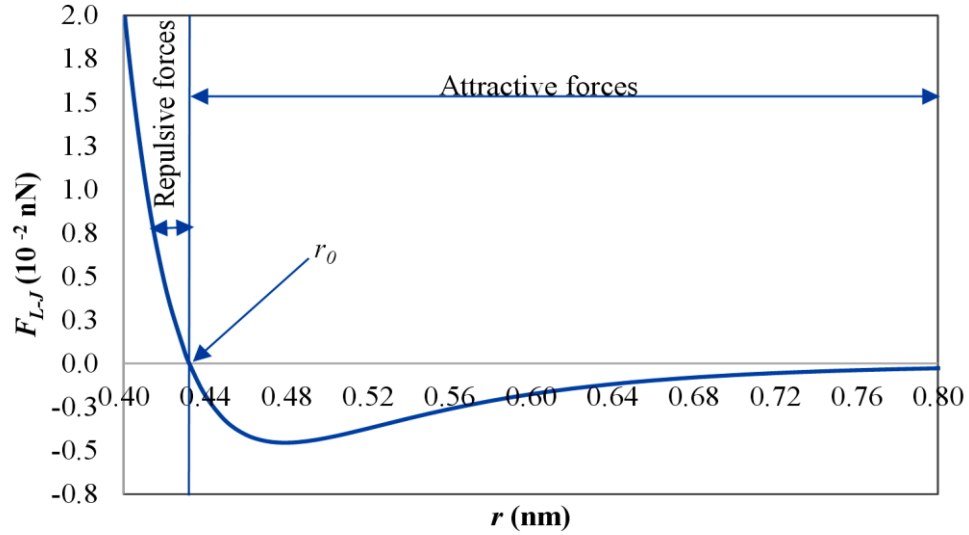


Figure 3.7 Plot of Lennard-Jones force versus the interatomic distance.

In order to simulate the weak vdW force of interaction between the tubes of MWNT, springs have been used in accordance with the authors Ghavamian et al. and Rahmandoust and Ochsner [5,20]. The challenge in characterizing the stiffness matrix for the springs used as reported by Rahmandoust and Ochsner [20] was to find force versus displacement points from the force versus distance values obtained from the Lennard-Jones potential. As already mentioned, at a critical distance $r_0 \sim 0.432$ nm, the force between the interacting atoms reaches zero. Interestingly, the interlayer distance for all the configurations considered in the study are all close to the critical distance, therefore the latter is considered as the unstretched length of the spring. To obtain the displacement points, this unstretched length of the spring was subtracted from the distance values. Due to the intrinsic non-linearity of the attained force-displacement curve, the software was unable to determine the appropriate stiffness matrix. Therefore, Rahmandoust and Ochsner [20] considered a small portion of the Lennard-Jones force graph. Likewise, this study considered a portion of the obtained force-displacement curve such that the original distance of the Lennard-Jones force encompasses around the range of intershell spacing considered in the study. Also it was important to include both the repulsive and attractive forces. Figure 3.8 shows the portion of force-displacement curve considered to simulate the stiffness of the springs that has been used for modelling vdW interaction between the tubes of MWNT. Accordingly, the springs are attached between two nodes separated by a maximum distance of 0.46 nm on the grounds that beyond this distance the interaction diminishes rapidly.

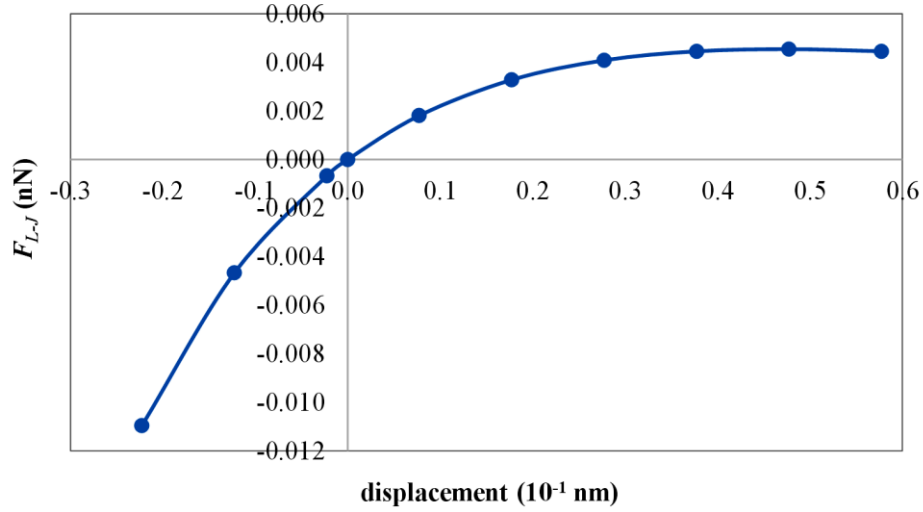


Figure 3.8 The portion of force-displacement curve considered in the study to simulate the stiffness of the springs used for modelling vdW interaction among the adjacent tubes of MWNT.

Following the results of He et al. [52] as already explained in the Section 2.1.5, the spring elements are used only to connect the atoms on the adjacent tubes, since the interaction among the remote tubes is so small that it can be neglected.

3.3. Numerical Results and Discussion

The aim of the study is to present a quantitative analysis of the mechanical properties of MWNTs which are affected by various factors like changing outer tube diameter, helicity, intershell spacing, number of tubes, and the axial length of the MWNT.

Figure 3.9 displays the isometric and top views of an armchair DWNT of configuration (5, 5) - (11, 11). It is to be noted that the interlayer distance maintained between the two tubes has been obtained from the Equation (3.8) and is different from the ones reported in literature (0.34 nm). The interlayer distance for the said configuration is ~ 0.407 nm and for the various configurations investigated in the study it ranges between 0.339 to 0.435 nm.

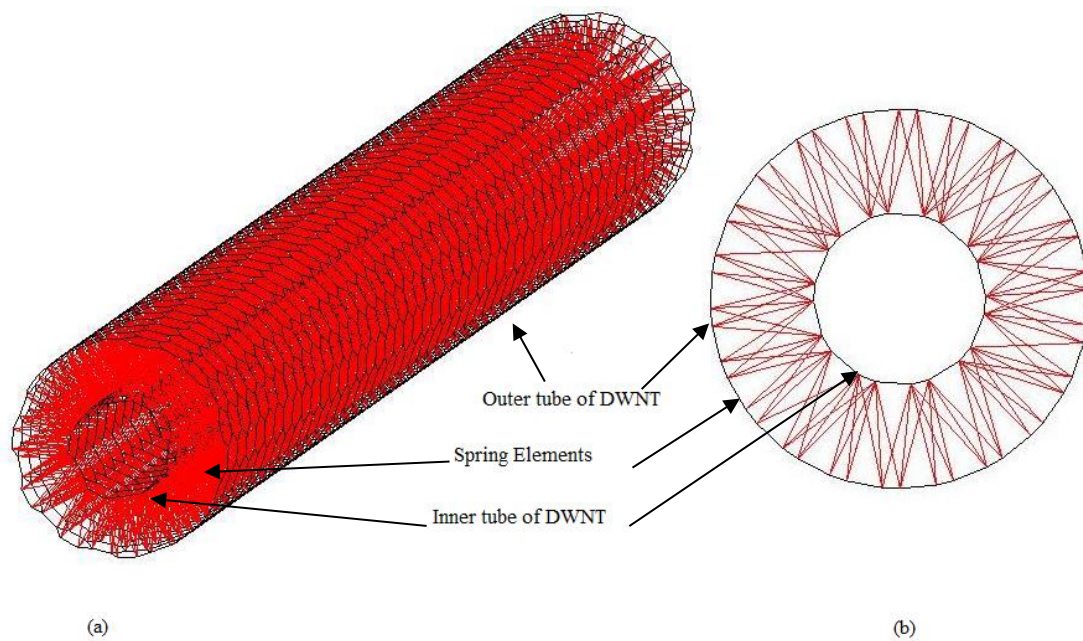


Figure 3.9 Finite element mesh of armchair DWNT of configuration (5, 5) - (11, 11) (a) Isometric view (b) Top view.

Table 3.2, Table 3.3, and Table 3.4 tabulate the characteristics of the monochiral and polychiral double-walled, triple-walled, and four-walled carbon nanotubes, respectively, that have been investigated in this research.

Table 3.2 Characteristics of monochiral and polychiral DWNTs investigated.

DWNTs	Diameter		Intershell Spacing	Inner Chirality	Outer Chirality	Length
	d_i (nm)	d_o (nm)	d_{002} (nm)	(deg)	(deg)	L (nm)
Monochiral						
Zigzag						
(5,0) - (16,0)	0.39	1.25	0.431	0	0	12.78
(9,0) - (20,0)	0.70	1.57	0.431	0	0	12.78
(12,0) - (22,0)	0.94	1.72	0.391	0	0	12.78
(17,0) - (27,0)	1.33	2.11	0.391	0	0	12.78
(20,0) - (30,0)	1.57	2.35	0.391	0	0	12.78
(25,0) - (35,0)	1.96	2.74	0.391	0	0	12.78
(35,0) - (44,0)	2.74	3.44	0.352	0	0	12.78
Armchair						
(3,3) - (9,9)	0.41	1.22	0.407	30	30	12.54
(5,5) - (11,11)	0.68	1.49	0.407	30	30	12.54
(7,7) - (13,13)	0.95	1.76	0.407	30	30	12.54
(9,9) - (15,15)	1.22	2.03	0.407	30	30	12.54
(12,12) - (18,18)	1.63	2.44	0.407	30	30	12.54
(15,15) - (21,21)	2.03	2.85	0.407	30	30	12.54
(21,21) - (26,26)	2.85	3.53	0.339	30	30	12.54
Polychiral						
Armchair-Chiral						
(2,2) - (13,2)	0.27	1.10	0.417	30	7.1	11.80
(5,5) - (16,5)	0.68	1.49	0.405	30	13.2	8.00
(9,9) - (20,9)	1.22	2.01	0.396	30	17.6	10.80
(13,13) - (24,13)	1.76	2.55	0.391	30	20.3	13.77
(17,17) - (28,17)	2.31	3.08	0.388	30	22.0	13.53
(20,20) - (31,20)	2.71	3.48	0.386	30	22.9	13.65
Zigzag-Chiral						
(3,0) - (13,2)	0.23	1.10	0.435	0	7.1	11.80
(8,0) - (16,5)	0.63	1.49	0.431	0	13.2	8.00
(16,0) - (20,9)	1.25	2.01	0.380	0	17.6	10.80
(23,0) - (24,13)	1.80	2.55	0.372	0	20.3	13.77
(30,0) - (28,17)	2.35	3.08	0.366	0	22.0	13.53
(35,0) - (31,20)	2.74	3.48	0.372	0	22.9	13.65

Table 3.3 Characteristics of TWNT investigated.

TWNTs	Diameter		Inner Chirality	Outer Chirality	Length
	d_i (nm)	d_o (nm)	θ_i (deg)	θ_o (deg)	L (nm)
Zigzag					
(5,0) - (16,0) - (26,0)	0.391	2.036	0	0	12.78
(9,0) - (20,0) - (30,0)	0.705	2.349	0	0	12.78
(12,0) - (22,0) - (32,0)	0.939	2.505	0	0	12.78
(17,0) - (27,0) - (37,0)	1.331	2.897	0	0	12.78
(20,0) - (30,0) - (40,0)	1.566	3.132	0	0	12.78
(25,0) - (35,0) - (44,0)	1.957	3.445	0	0	12.78
Armchair					
(3,3) - (9,9) - (15,15)	0.407	2.034	30	30	12.54
(5,5) - (11,11) - (17,17)	0.678	2.305	30	30	12.54
(7,7) - (13,13) - (19,19)	0.949	2.576	30	30	12.54
(9,9) - (15,15) - (21,21)	1.220	2.848	30	30	12.54
(12,12) - (18,18) - (24,24)	1.627	3.254	30	30	12.54
(15,15) - (21,21) - (26,26)	2.034	3.526	30	30	12.54

Table 3.4 Characteristics of MWNT investigated.

MWNTs	Diameter		Inner Chirality	Outer Chirality	Length
	d_i (nm)	d_o (nm)	θ_i (deg)	θ_o (deg)	L (nm)
Zigzag					
(5,0) - (16,0) - (26,0) - (36,0)	0.391	2.818	0	0	12.78
(9,0) - (20,0) - (30,0) - (40,0)	0.705	3.132	0	0	12.78
(12,0) - (22,0) - (32,0) - (42,0)	0.939	3.288	0	0	12.78
(17,0) - (27,0) - (37,0) - (46,0)	1.331	3.601	0	0	12.78
(20,0) - (30,0) - (40,0) - (49,0)	1.566	3.836	0	0	12.78
(25,0) - (35,0) - (44,0) - (53,0)	1.957	4.149	0	0	12.78
Armchair					
(3,3) - (9,9) - (15,15) - (21,21)	0.407	2.848	30	30	12.54
(5,5) - (11,11) - (17,17) - (23,23)	0.678	3.119	30	30	12.54
(7,7) - (13,13) - (19,19) - (24,24)	0.949	3.254	30	30	12.54
(9,9) - (15,15) - (21,21) - (26,26)	1.220	3.526	30	30	12.54
(12,12) - (18,18) - (24,24) - (29,29)	1.627	3.932	30	30	12.54
(15,15) - (21,21) - (26,26) - (31,31)	2.034	4.204	30	30	12.54

3.3.1. Prediction of Young's Modulus of MWNTs

Information about Young's modulus (also known as elastic modulus and modulus of elasticity) of any structural member is important to ascertain its feasibility for use in structural applications [42]. To estimate the Young's modulus of the MWNT, a fixed axial displacement (ΔL) of 0.1 nm is given at one of its ends while the other is fixed constraining any displacement or rotation in/about any axis at this end. To calculate the Young's modulus (E) Equation (3.11) is used [4]:

$$E = \frac{FL_0}{A\Delta L} \quad (3.11)$$

where F is the net reaction force of the nodes that are fixed, L_0 is the undeformed length of MWNT, and A is its annular cross-sectional area given by Equation (3.12) [4,20]:

$$A = \frac{\pi}{4} [(d_o + t)^2 - (d_i - t)^2] \quad (3.12)$$

where t is the tube thickness presumed to be equal to 0.34 nm and d_o and d_i are the outermost and innermost diameters of MWNT respectively as depicted by Figure 3.10.

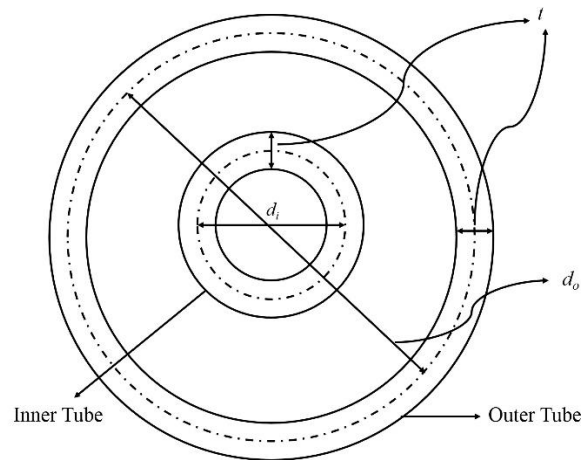


Figure 3.10 Schematic illustration of the cross section of a DWNT depicting thickness (t), inner diameter (d_i) and outer diameter (d_o).

Figure 3.11 shows the imposed boundary conditions on 4 different configurations of DWNT: Zigzag (5, 0) - (16, 0), Armchair (3, 3) - (9, 9), Armchair-chiral (2, 2) - (13, 2) and Zigzag-chiral

(3, 0) - (13, 2) respectively. As can be seen, one end is restricted from translational and rotational motion while the other is displaced axially.

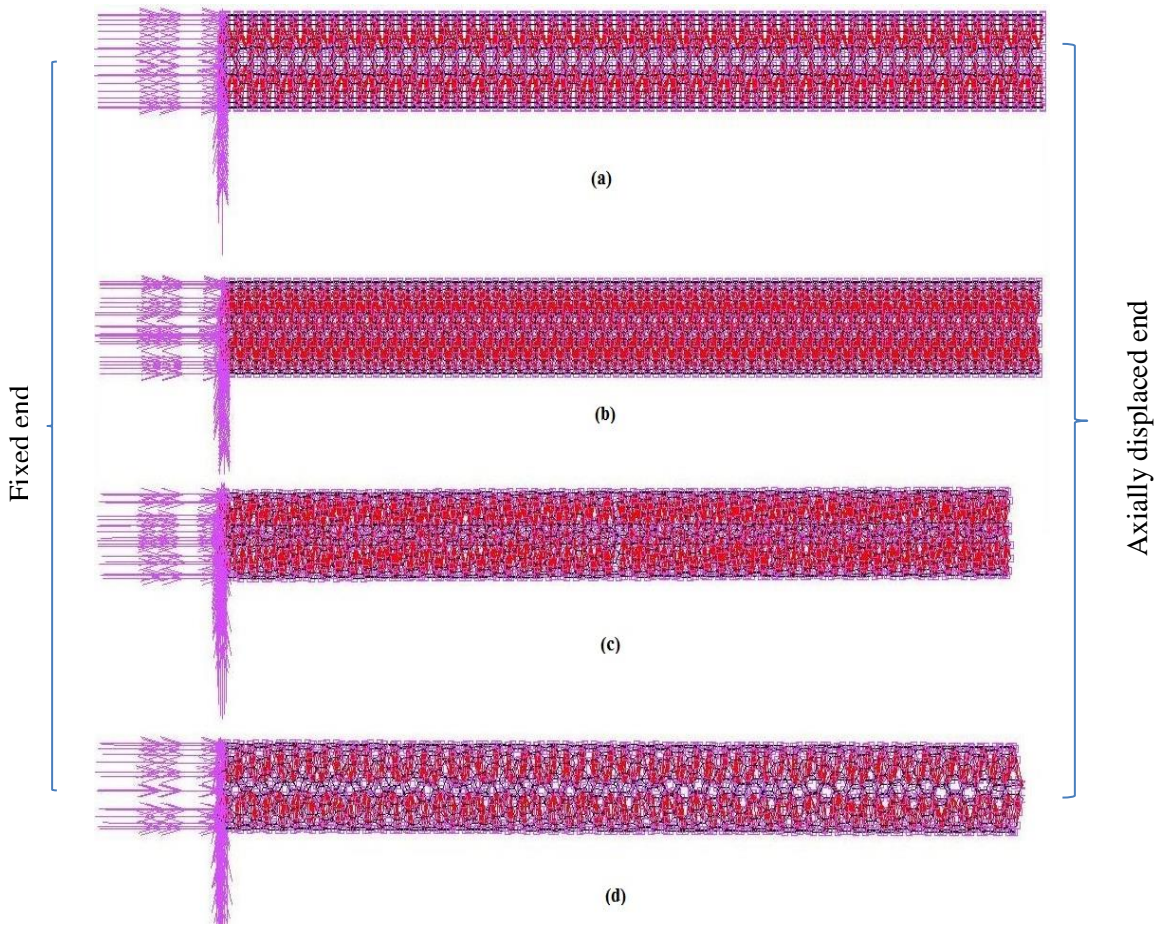


Figure 3.11 Model mesh of (a) zigzag (5, 0) - (16, 0), (b) armchair (3, 3) - (9, 9) (c) armchair-chiral (2, 2) - (13, 2) and (d) zigzag-chiral (3, 0) - (13, 2) showing the imposed boundary conditions.

Figure 3.12 depicts the simulation result for Armchair (3, 3) - (9, 9), highlighting both the undeformed and deformed lengths as a result of axial displacement. For the sake of clarity, the spring elements are not shown.

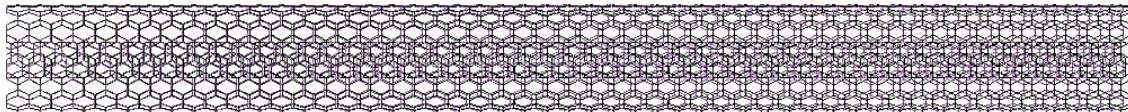


Figure 3.12 Simulation of Armchair (3, 3) - (9, 9) DWNT subjected to axial displacement (Both original and deformed simulations are shown).

3.3.1.1. Impact of DWNT's Diameter and Chirality on its Young's Modulus

As already mentioned, previous works have not reported polychiral configurations owing to the complexity involved. This work investigates and compares both monochiral and polychiral configurations of MWNT.

Figure 3.13 shows the sensitivity of Young's modulus to the influence of varying outer tube diameter and chirality of DWNT. The figure shows that the outer tube diameter positively affects the Young's moduli quite significantly for all chiral configurations. This increasing trend of modulus of elasticity against the outer tube diameter is accredited to the increase in total reaction force of the nodes at the fixed end. The total reaction force with increase in diameter increases more significantly than the simultaneous increase in the area of cross section of the DWNT. Monochiral armchair DWNTs have almost a constant modulus of elasticity around 0.810 TPa against all diameters up to around 2.0 nm, hence they can be regarded as size-independent. For greater diameters, monochiral armchair DWNTs are observed to have an influence on their Young's modulus. Young's moduli of monochiral zigzag and polychiral zigzag-chiral configurations of MWNT are extremely sensitive to changing diameter especially for small diameter up to 2 nm. Young's modulus of Polychiral armchair-chiral MWNT is less sensitive to the influence of diameter change and attains almost a plateau after the outer tube diameter of around 2 nm. The high sensitivity at small diameters is ascribed to the effect of curvatures at small diameters which tend to distort the C-C bonds which is diminished when the diameter is increased [53]. The elastic moduli of polychiral zigzag-chiral is greatest after the outer tube diameter ~ 2.0 till the outer tube diameter of ~ 3.0 nm. The rate at which the Young's moduli changes with the increase in diameter is observed to be inconsistent due to the influence of another important factor that is intershell spacing which is discussed in the Section 3.3.1.2.

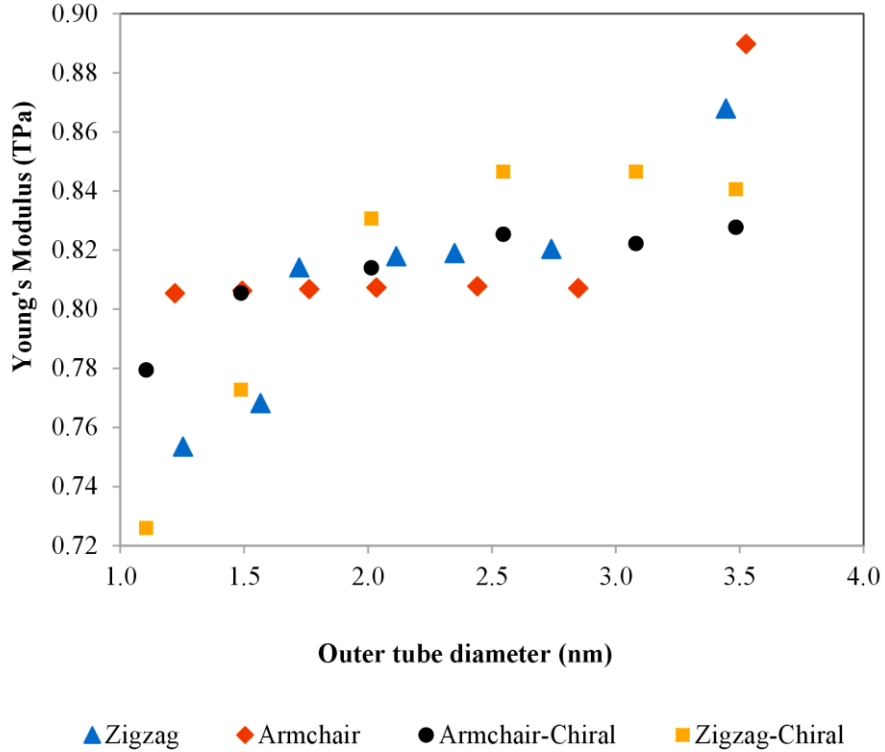


Figure 3.13 Young's Moduli versus the outer tube diameter of DWNT for zigzag, armchair, armchair-chiral and zigzag-chiral configurations.

Table 3.5 shows the impact of DWNT's chirality on its average Young's modulus for all configurations of DWNT that have been studied and the corresponding spread of the moduli in terms of standard deviation. As is evident, the average modulus of elasticity of monochiral armchair DWNT is the highest, followed by polychiral armchair-chiral and polychiral zigzag-chiral. Monochiral zigzag DWNT has the least elastic modulus. The average elastic moduli for all configurations is observed to be around 0.8 TPa. As for the overall spread of the moduli against the outer tube diameters between 1 to 3.5 nm, as depicted by the standard deviation, it can be said that polychiral zigzag-chiral configuration shows the largest deviation from its average value, followed by monochiral zigzag and monochiral armchair. Polychiral armchair-chiral shows the least standard deviation, signifying the fact that it deviates the least with the changing diameter, thus seems an ideal candidate for structural applications under axial strain.

Table 3.5 Effect of chirality on the average Young's moduli of DWNT and the corresponding standard deviation.

DWNT	Average (TPa)	St. Dev. (TPa)
Monochiral Zigzag	0.809	0.038
Monochiral Armchair	0.819	0.031
Armchair-Chiral	0.812	0.018
Zigzag-Chiral	0.811	0.050

3.3.1.2. Impact of Intershell Spacing on the Young's Modulus of DWNTs

To study the effect of intershell spacing on the Young's modulus of the DWNT, monochiral armchair and monochiral zigzag DWNTs of approximately the same outer tube diameter are taken into account in order to disregard any effect of the outer tube diameter. However, since changing the intershell spacing directly implies changing the inner diameter of the DWNT, the effect of cross-sectional area on the Young's modulus will also be included. Therefore, in order to disregard the cross-sectional area effect, the property called tensile resistance (EA), which is the product of Young's modulus and the cross-sectional area, is studied against the changing intershell spacing. Table 3.6 enlists different configurations analysed to study the effect of changing intershell spacing on the Young's modulus. Herein, the outer tube is fixed and the inner tube is arbitrarily varied in order to change the intershell spacing.

Figure 3.14 illustrates how sensitive the tensile resistance of monochiral armchair and monochiral zigzag DWNTs of an outer diameter of around 1.7 nm are to the varying intershell spacing. The outer tube diameter around 1.7 nm is deliberately chosen, since from the effect of outer diameter on the elastic modulus (Figure 3.13), it is evident that the moduli of monochiral armchair and zigzag DWNTs have almost the same value. As can be seen from Figure 3.14, decreasing the intershell spacing significantly increases the tensile resistance and thus the Young's modulus, signifying the changing gradient of Figure 3.13. Increase in outer tube diameter corresponds to an increase in inner tube diameter of a DWNT, which implies reduced intershell spacing that according to Figure 3.14 suggests increased Young's modulus.

Table 3.6 Different configurations of monochiral armchair and zigzag under investigation to study the effect of intershell spacing.

DWNTs	Diameter		Intershell Spacing
	d_i (nm)	d_o (nm)	d_{002} (nm)
Zigzag			
(5,0) - (22,0)	0.39	1.72	0.665
(9,0) - (22,0)	0.70	1.72	0.509
(12,0) - (22,0)	0.94	1.72	0.391
(17,0) - (22,0)	1.33	1.72	0.196
Armchair			
(3,3) - (13,13)	0.41	1.76	0.678
(5,5) - (13,13)	0.68	1.76	0.542
(7,7) - (13,13)	0.95	1.76	0.407
(9,9) - (13,13)	1.22	1.76	0.271

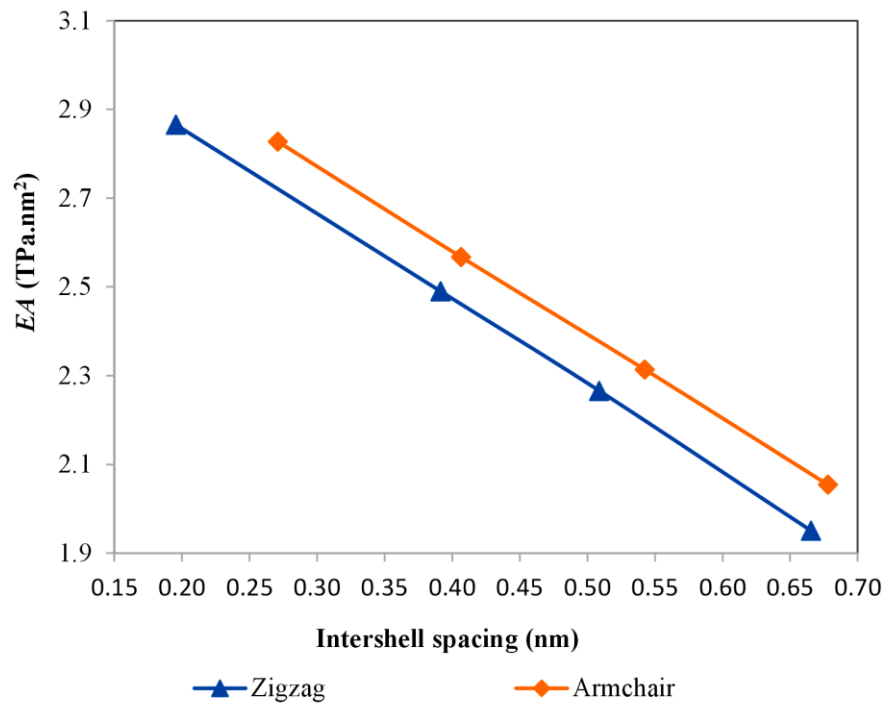


Figure 3.14 The relation between tensile resistance and the intershell spacing of DWNT of an outer diameter of ~1.7 nm for monochiral zigzag and armchair configurations.

3.3.1.3. Impact of Number of Tubes on Young's Modulus of MWNTs

To study the influence of number of tubes on the elastic modulus of the MWNTs, only the monochiral configurations of MWNT are studied owing to the complexity involved with modelling MWNT polychiral configurations. Table 3.7 shows the different configurations of monochiral zigzag and armchair MWNTs studied to analyse the effect of number of tubes on their Young's modulus.

Table 3.7 Different configurations of monochiral armchair and zigzag MWNTs under investigation to study the effect of number of tubes.

MWNTs	Diameter d_o (nm)
<i>Zigzag</i>	
(40,0)	3.132
(30,0) - (40,0)	3.132
(20,0) - (30,0) - (40,0)	3.132
(9,0) - (20,0) - (30,0) - (40,0)	3.132
<i>Armchair</i>	
(24,24)	3.254
(19,19) - (24,24)	3.254
(13,13) - (19,19) - (24,24)	3.254
(7,7) - (13,13) - (19,19) - (24,24)	3.254

Figure 3.15 shows the sensitivity of Young's modulus of MWNT to the different number of tubes. Young's modulus tends to decrease upon increasing the number of tubes for the same diameter. The increase of number of tubes should imply an increase in the reaction force and thus an upward trend of the Young's modulus. However, the increase in reaction force is accompanied by an even larger increase in the area of cross section which causes the Young's modulus to decrease. Studies by Li and Chou and Lu [53,54] have reported an upward trend of the Young's modulus against the number of tubes because of the lower intershell spacing considered by them which contributed towards a cross-sectional area which is lower than the one this study obtained. Greater intershell spacing in the present study causes the weakening of the vdW bonds between the tubes, resulting in the decrease of the modulus of elasticity.

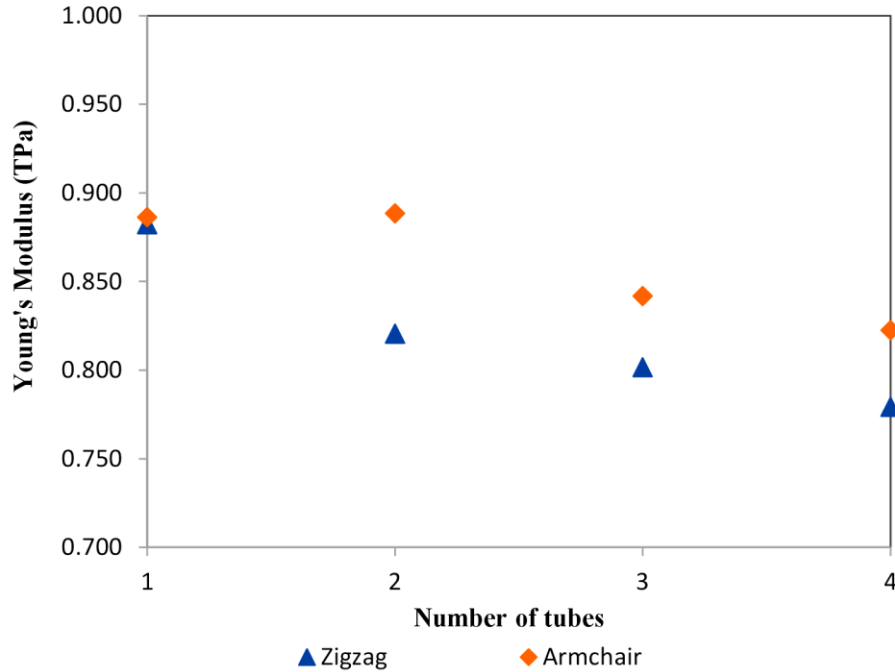


Figure 3.15 The relation between Young's Moduli and the number of tubes of MWNT with an outermost tube diameter of ~3.0 nm.

Table 3.8 shows the influence of number of tubes on the average elastic modulus of MWNT. The average Young's modulus is observed to have decreased when number of tubes is increased from 2 to 3. This is because of the larger cross-sectional area of the resulting 3-walled nanotube. Increase in number of tubes to 4 from 3, however, results in an increase in the Young's modulus

Table 3.8 Influence of number of tubes on the average elastic moduli of MWNT (n is the number of tubes).

Configuration	E (TPa)		
	$n = 2$	$n = 3$	$n = 4$
Zigzag	0.809	0.798	0.805
Armchair	0.819	0.794	0.812

3.3.1.4. Influence of Axial Length on DWNT's Young's Modulus

To analyse the influence of length on the modulus of elasticity of DWNT, two configurations of monochiral armchair and monochiral zigzag DWNTs each of approximately the same outer tube diameter are taken into consideration. Figure 3.16 shows the sensitivity of Young's modulus of zigzag and armchair DWNT with the configurations (9, 0) - (20, 0) and armchair (5, 5) - (11, 11)

respectively to the different lengths. It can be seen that changing the axial length between ~ 7 nm and ~ 12 nm affects the Young's modulus of monochiral zigzag but very slightly. Similarly, for monochiral armchair DWNT, changing length from ~ 7 nm to ~ 24 nm slightly affects the Young's modulus. Upon further increasing the length, however, no significant change in the Young's modulus was observed neither for armchair nor for zigzag configurations, as can be expected since Young's modulus is the material behaviour that depends on the morphology and geometry and not on the length.

Table 3.9 displays the modulus of elasticity with respect to the changing length and the corresponding deviation with around 100 nm length taken as the standard. For both zigzag and armchair configurations, it can be clearly seen that the percentage deviation of the Young's moduli for all lengths from the Young's modulus at 100 nm is within 3 percent which is negligible. Therefore, it would be convenient to use any length without incorporating any significant error in the final result.

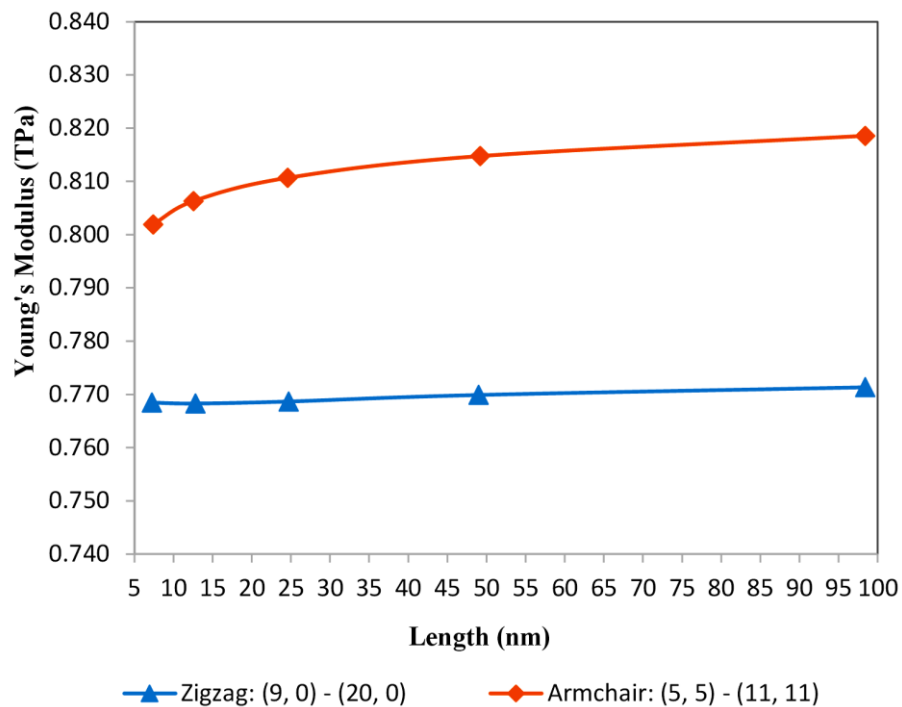


Figure 3.16 The relation between Young's Moduli and the length of DWNT for zigzag (9, 0) - (20, 0) and armchair (5, 5) - (11, 11).

Table 3.9 Effect of length on the Young's modulus of DWNT.

Length	E (TPa)	% deviation
Zigzag: (9, 0) - (20, 0)		
7.24	0.768	0.374
12.78	0.768	0.395
24.71	0.769	0.345
48.99	0.770	0.187
98.41	0.771	0.000
Armchair: (5, 5) - (11, 11)		
7.38	0.802	2.031
12.54	0.806	1.499
24.60	0.811	0.963
49.19	0.815	0.465
98.38	0.819	0.000

3.3.2. Prediction of Shear Modulus of MWNTs

To evaluate the shear Modulus of the MWNT, at one end of the MWNT a uniform amount of torsion equal to 0.1 nN.nm about the longitudinal axis (z -axis) is applied at each node. The other end of the MWNT is fixed such that any displacement or rotation in/about any axis at this end is constrained. To obtain the shear modulus (G) the following equation is used [4]:

$$G = \frac{TL_0}{J\phi} \quad (3.13)$$

where T is total applied torque, L_0 is the undeformed length of MWNT, ϕ is the twist angle measured in radians, and J is the polar moment of inertia given by [4]:

$$J = \frac{\pi}{32} [(d_o + t)^4 - (d_i - t)^4] \quad (3.14)$$

Figure 3.17 shows the simulation result for Zigzag (8, 0) - (19, 0), highlighting both the original and deformed lengths as a result of torsional load. For the sake of vividness, the spring elements are not shown.

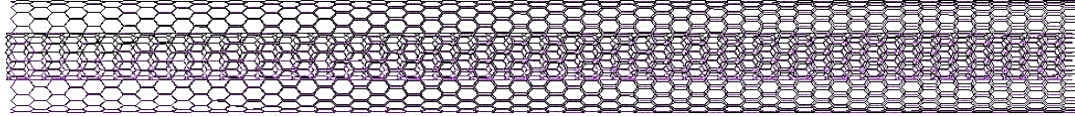


Figure 3.17 Simulation of Zigzag (8, 0) - (19, 0) DWNT subjected at one end to torsional load about the axial axis and fixed at the other end (Both original and deformed simulations are shown).

3.3.2.1. Impact of DWNT's Diameter and Chirality on its Shear Modulus

Figure 3.18 shows the effect of varying outer tube diameter and helicity of DWNT on its shear moduli. It can be seen that there is a decreasing trend for monochiral configurations with an increase in the outer tube diameter up to the diameter of around 3nm. This is due to the significant increase in the polar moment of inertia with an increase in tube diameter that leads to the decrease in shear modulus. It is worth noting that, like polar moment of inertia, angle of twist also has an inversely proportional relation with the shear modulus but since its decrease with the increase in tube diameter is not that profound, its positive effect on shear modulus is not significant in the resulting shear modulus. The figure shows that monochiral DWNTs possess greater shear moduli than polychiral for all diameters. For the monochiral configuration, shear modulus of zigzag DWNTs is greater than that of armchair for all outer tube diameters. However, for polychiral DWNT, for smaller diameters up to around 1.7 nm, shear modulus of armchair-chiral DWNT is greater than that of zigzag-chiral DWNTs but for larger outer tube diameters it is the other way round. The relationship of shear modulus of polychiral DWNTs does not seem consistent owing to the varying intershell spacing whose effect is explained in the Section 3.3.2.2.

Table 3.10 shows the influence of helicity on the shear moduli for all configurations of DWNT that have been studied and the corresponding standard deviation. As can be observed, the average shear modulus of monochiral zigzag DWNT is the greatest, followed by monochiral armchair and polychiral zigzag-chiral. Polychiral armchair-chiral DWNT has the least shear modulus. It would be appropriate to deduce from the table that the monochiral configuration of DWNT has greater shear modulus than their polychiral counterparts owing to their axial symmetry. The overall spread of the shear modulus for different chiralities against the diameters can be depicted by the standard deviation. Monochiral armchair DWNT seems to have maximum deviation from the average shear modulus. This is attributed to the sudden increase in the shear modulus for the outer tube diameter of 3.5 nm. All the other configurations have more or less same deviations from their averaged shear moduli.

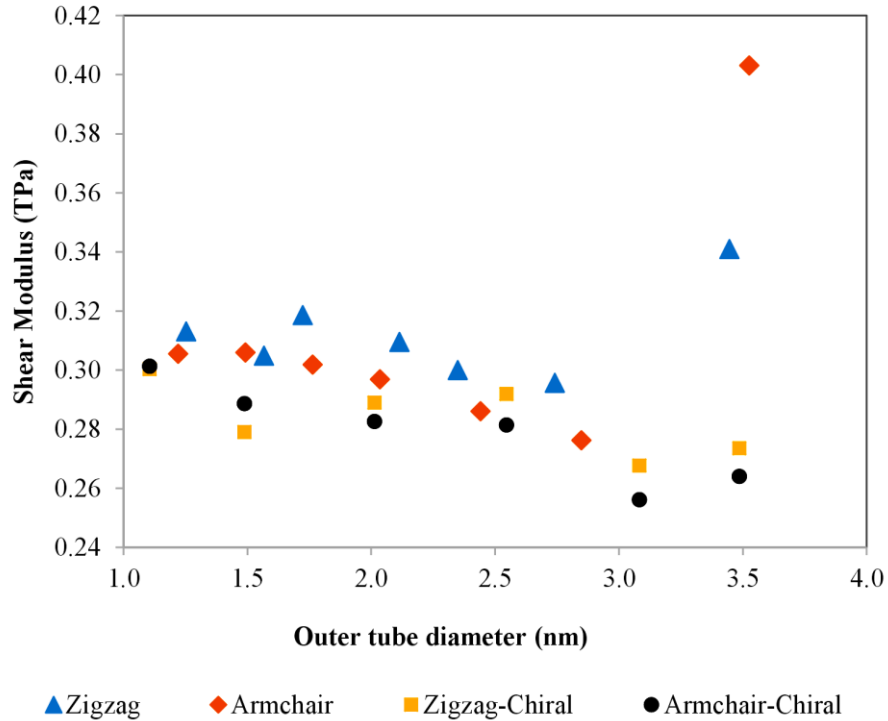


Figure 3.18 Shear moduli versus the outer tube diameter of DWNT for zigzag, armchair, armchair-chiral and zigzag-chiral configurations.

Table 3.10 Effect of chirality on the average shear moduli of DWNT and the corresponding standard deviation.

DWNT	Average (TPa)	St. Dev. (TPa)
Monochiral Zigzag	0.312	0.015
Monochiral Armchair	0.311	0.042
Armchair-Chiral	0.279	0.016
Zigzag-Chiral	0.284	0.012

3.3.2.2. Influence of Intershell Spacing on DWNT's Shear Modulus

To study the effect of intershell spacing on the shear modulus of the DWNT, monochiral armchair and monochiral zigzag DWNTs of approximately the same outer tube diameter are taken into account in order to disregard any effect of the outer tube diameter as given in Table 3.6. However, since changing the intershell spacing directly implies changing the inner diameter of the DWNT, the effect of cross-sectional area on the shear modulus will also be included. Therefore, in order to disregard the cross-sectional area effect, the property called torsional stiffness (GJ), which is

the product of shear and the polar moment of inertia, is studied against the changing intershell spacing.

Figure 3.19 shows how sensitive the torsional stiffness of monochiral armchair and monochiral zigzag DWNTs of an outer diameter of ~ 1.7 nm are to the influence of intershell spacing. As can be seen, decreasing the intershell spacing significantly increases the shear modulus signifying the sudden increase in the shear modulus in Figure 3.17. Increase in outer tube diameter corresponds to an increase in inner tube diameter of a DWNT, which implies reduced intershell spacing that according to Figure 3.19 suggests increase in shear modulus

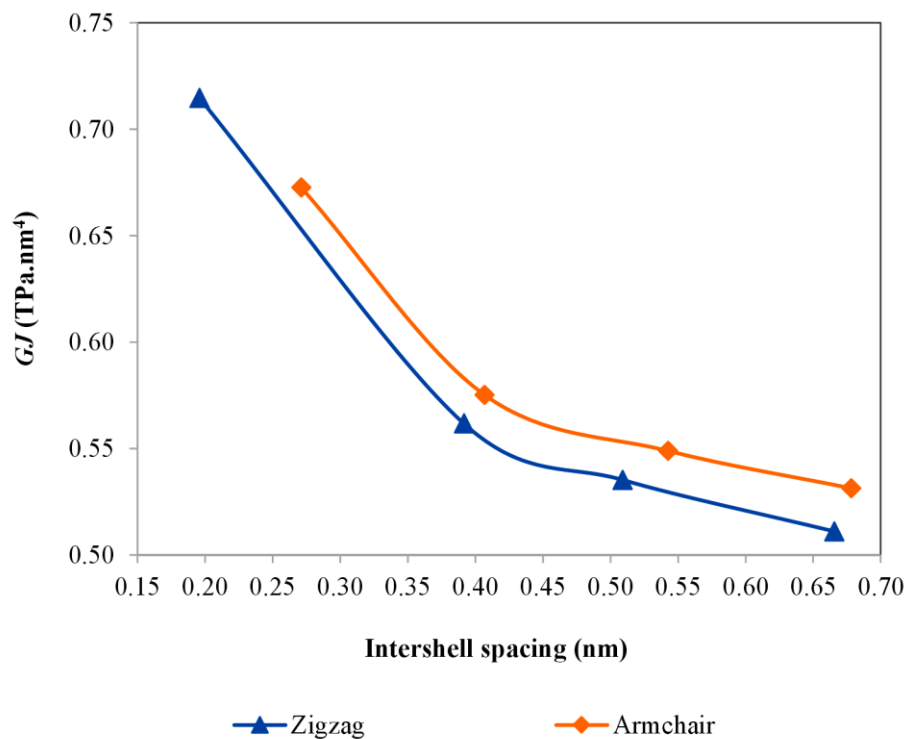


Figure 3.19 The relation between shear moduli and the intershell spacing of DWNT of an outer diameter of ~ 1.7 nm for zigzag, armchair, armchair-chiral and zigzag-chiral configurations.

3.3.2.3. Influence of Number of Tubes on MWNT's Shear Modulus

Effect of number of tubes on the shear modulus is analysed by investigating different configurations of monochiral armchair and zigzag MWNTs which are enlisted in Table 3.7. Figure 3.20 shows the sensitivity of shear modulus of MWNT to the different number of tubes. It

shows a downward trend of shear modulus against number of tubes. The downward trend is due to the increase in the polar moment of inertia.

Table 3.11 tabulates the averaged shear moduli for zigzag and armchair configurations of 2, 3 and 4 walled nanotubes. It is predicted that with increase in number of tubes, the shear modulus would decrease significantly. The decrease is ensued from the increase in polar moment of inertia that is quite significant as compared to the decrease in the angle of twist.

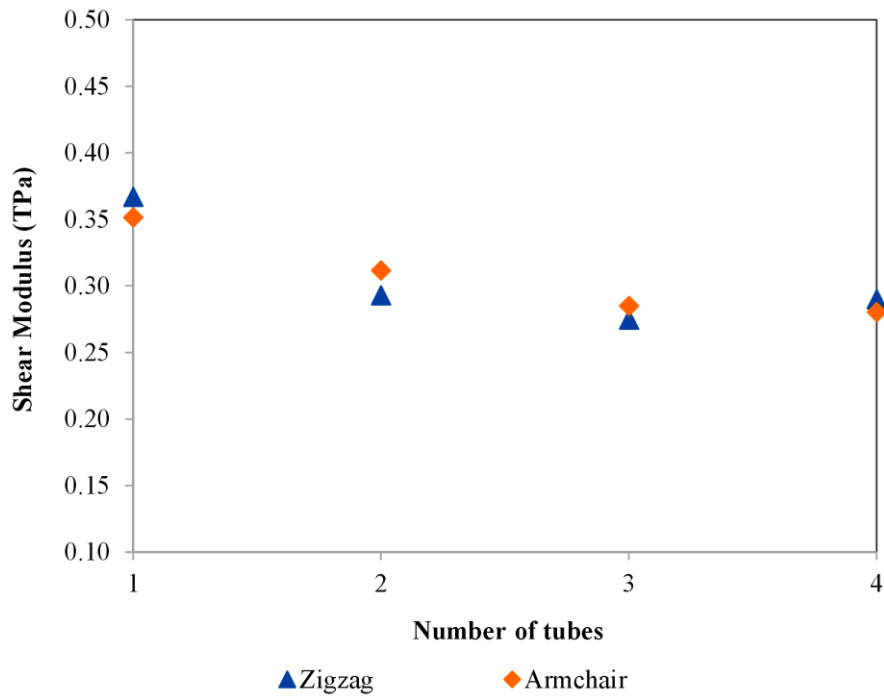


Figure 3.20 The relation between shear moduli and the number of tubes of MWNT with an outermost tube diameter of ~3.0 nm.

Table 3.11 Influence of number of tubes on the average shear moduli of zigzag and armchair MWNT (n is the number of tubes).

Configuration	G (TPa)		
	$n = 2$	$n = 3$	$n = 4$
Zigzag	0.312	0.291	0.263
Armchair	0.311	0.270	0.254

3.3.3. Prediction of Shear Strain of MWNTs

Shear strain (γ_n) for the n^{th} layer of MWNT can be calculated from [77]:

$$\gamma_n = \frac{r_n \varphi}{L} \quad (3.15)$$

where r_n is the radius of the n^{th} layer of MWNT. The highest shear strain is obtained for the outermost tube, thus shear strain for the outermost tube (γ_o) is computed using the simulation results attained for determining shear modulus.

3.3.3.1. Impact of DWNT's Diameter and Chirality on its Shear Strain

Figure 3.21 shows the effect of varying outer tube diameter of DWNT on its shear strain. The figure indicates a decreasing trend of shear strain with an increase in outer tube diameter owing to the decrease in the angle of twist for larger diameters under the application of same torsional load [67]. Since the length has been kept almost constant for the nanotubes under consideration, the outer tube radii and angle of twist are the two factors that affects the shear strain. Outer tube diameter increases only by around 0.25 nm and thus its effect on the shear strain is not that significant. Decrease of angle of twist is expected when increasing the diameter of the outer tube because the greater the outer tube diameter, greater is the ability to resist deformation. No computational and experimental values have so far been reported on shear strain for MWNTs, thus the predicted trend is first of its kind. Other than monochiral zigzag configuration, all three configurations are observed to have similar effect of diameter on their shear strain. Monochiral zigzag DWNT has the least shear strain of all four configurations.

Table 3.12 depicts the influence of helicity on the average shear strain of the outer tube of DWNT and the corresponding standard deviation. As is evident, chirality has no significant effect on the average shear strain of DWNT. While monochiral zigzag DWNT possesses slightly lower shear strain, the average shear strains of the other three configurations are the same. The deviation of the shear strain with respect to the average value is maximum for the polychiral configurations, followed by monochiral armchair and monochiral zigzag DWNTs.

Table 3.12 Effect of chirality on the average shear strain of the outer tube of DWNT.

DWNT	Average	St. Dev.
Monochiral Zigzag	0.003	0.0013
Monochiral Armchair	0.004	0.0016
Armchair-Chiral	0.004	0.0018
Zigzag-Chiral	0.004	0.0018

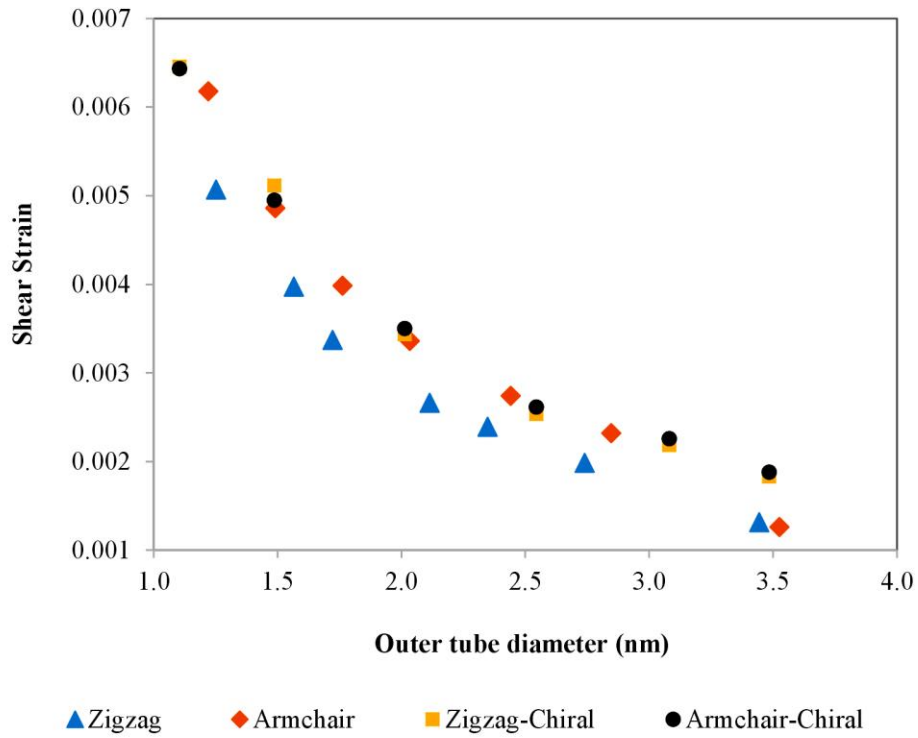


Figure 3.21 Shear strain versus the outer tube diameter of DWNT for zigzag, armchair, armchair-chiral and zigzag-chiral configurations.

3.3.3.2. Impact of Intershell Spacing on Shear Strain of DWNTs

Figure 3.22 illustrates the relation between shear strain and intershell spacing. The figure depicts that intershell spacing significantly affects the shear strain in a way that when one increases the other increases too. This is because as the intershell spacing increases, the interaction among the tubes in an MWNT gets weak, thereby increasing the shear strain.

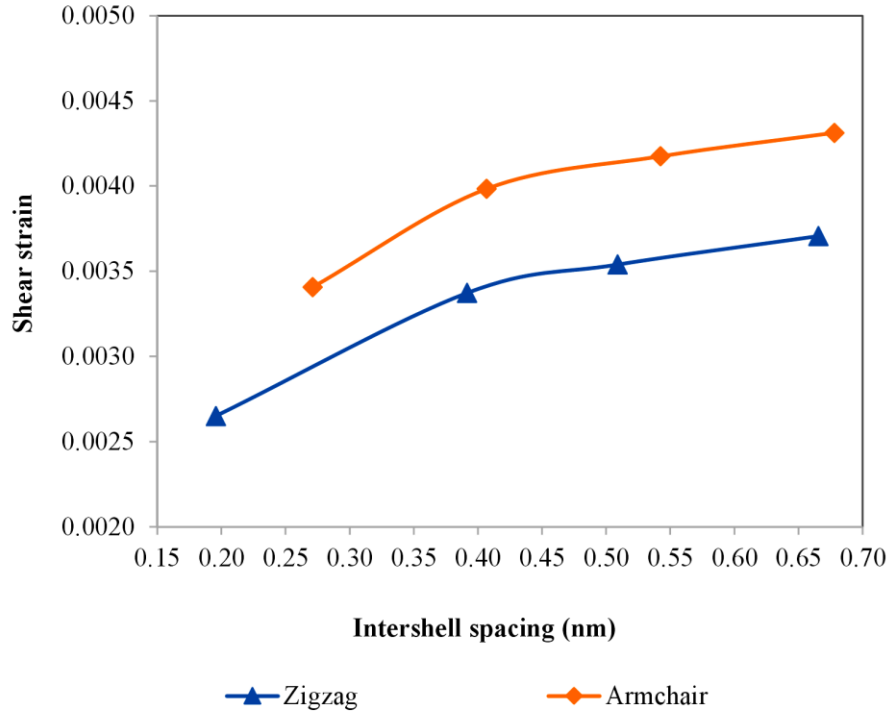


Figure 3.22 The relation between shear strain and the intershell spacing of DWNT of an outer diameter of ~1.7 nm for monochiral zigzag and monochiral armchair configurations.

3.3.3.3. Impact of Number of Tubes on Shear Strain of MWNT

Figure 3.23 shows that increasing the number of tubes of MWNT decreases the shear strain of the monochiral armchair and zigzag MWNTs. This is attributed to the fact that with an increase in number of tubes, the MWNTs become more stable towards any change in their structure.

Table 3.13 shows the similar relation between number of tubes and average shear strain. It shows that increasing the number of tubes of MWNT results in the drop of shear strain.

Table 3.13 Effect of number of tubes on the average shear strain of MWNT (n is the number of tubes).

Configuration	Shear Strain		
	$n = 2$	$n = 3$	$n = 4$
Zigzag	0.003	0.002	0.001
Armchair	0.004	0.003	0.002

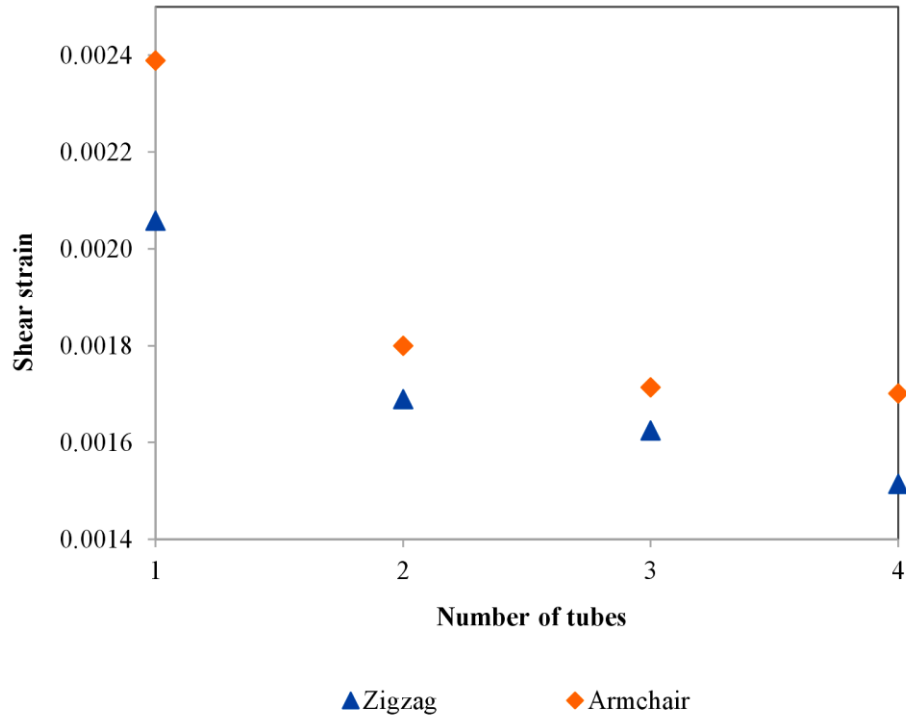


Figure 3.23 The relation between shear strain and the number of tubes of MWNT with an outer most tube diameter of ~3.0 nm.

3.3.4. Prediction of Poisson's Ratio of MWNTs

Poisson's ratio (ν) of MWNTs is determined by axially displacing one end of the tube by 0.1 nm that is fixed at the other end. It is evaluated by Equation (3.16) [67]:

$$\nu = -\frac{\Delta d}{d_o} \times \frac{L}{\Delta L} \quad (3.16)$$

where Δd and ΔL are changes in outer tube diameter and length respectively.

3.3.4.1. Impact of DWNT's Diameter and Chirality on its Poisson's Ratio

Figure 3.24 shows the sensitivity of Poisson's ratio to the influence of varying outer tube diameter and chirality of DWNT for various configurations. For monochiral zigzag DWNTs, as apparent the Poisson's ratio decreases with increase in outer tube diameter up to ~1.75 nm, because of the curvature effects for smaller diameters. After ~1.75 nm, there is no significant effect of outer tube diameter on its Poisson's ratio. For polychiral DWNT, the trend is irregular. For all the

configurations, Poisson's ratio does not exceed 0.5 which signifies the isotropic nature of carbon nanotubes. The sudden changes in the trend is due to the influence of variation in the intershell spacing. Decrease in intershell spacing to lower than the critical distance implies repulsion between the tubes which favours lateral deformation, thus causing the Poisson's ratio to increase.

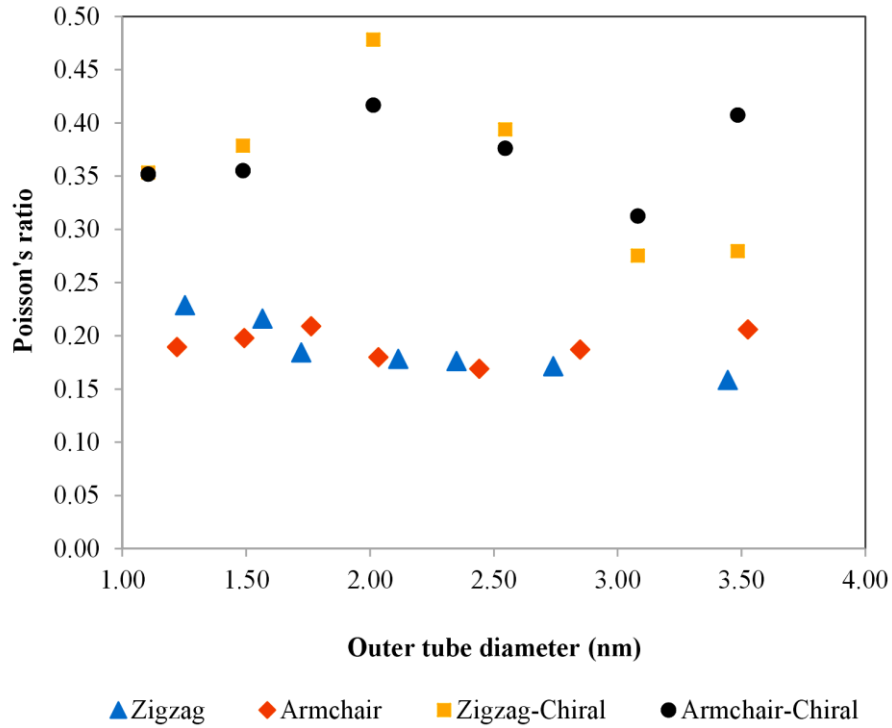


Figure 3.24 Poisson's ratio versus the outer tube diameter of DWNT for zigzag, armchair, armchair-chiral and zigzag-chiral configurations.

Table 3.14 shows the influence of helicity on the average Poisson's ratio of DWNT. On average, polychiral configurations have greater Poisson's ratio than monochiral DWNT. Overall, by the descending order of Poisson's ratio, polychiral armchair-chiral leads the group, followed by polychiral zigzag-chiral. Monochiral armchair and monochiral zigzag seem to have almost same Poisson's ratio. From the standard deviation, the deviation of the Poisson's ratio can be easily explained. The monochiral DWNTs have the least amount of deviation from their average Young's moduli while the polychiral DWNTs are observed to have the most deviation owing to their asymmetric geometrical structure.

Table 3.14 Effect of chirality on the average Poisson's ratio of DWNT and the corresponding standard deviation.

DWNT	Average	St. Dev.
Monochiral Zigzag	0.188	0.0253
Monochiral Armchair	0.191	0.0142
Armchair-Chiral	0.370	0.0386
Zigzag-Chiral	0.360	0.0763

3.3.4.2. Impact of Number of Tubes on Poisson's Ratio of MWNTs

Figure 3.25 shows the predicted relation between number of tubes and Poisson's ratio. As it can be easily perceived from the figure, the Poisson's ratio for monochiral armchair MWNT decreases up until 3-walled MWNTs. This is because of the increased stability of the MWNT attained by greater number of tubes that resists lateral deformation. However, a further increase in the tube number has no significant effect on its Poisson's ratio. In the case of monochiral zigzag MWNT, the Poisson's ratio also decreases with an increase in the tube number with the exception from increase in number of tubes from 2 to 3 whereby it increases, however, only very slightly. This change is due to the decrease in intershell spacing between tube 2 and 3.

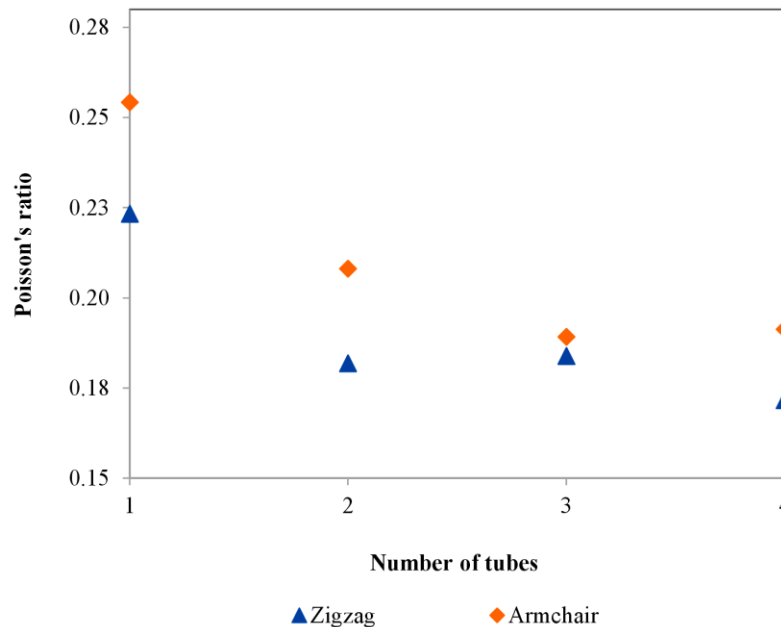


Figure 3.25 The relation between Poisson's ratio and the number of tubes of MWNT with an outermost tube diameter of ~3.0 nm.

3.3.5. Tensile resistance and Torsional Stiffness of MWNTs

Tensile resistance (EA) and torsional stiffness (GJ) are the two properties that neglect the effect, if any, of the cross-sectional area and polar moment of inertia of MWNTs on their mechanical properties.

Figure 3.26 shows the illustration of how outer tube diameter of MWNT almost linearly affects the tensile resistance. Irrespective of what the chirality of MWNTs is, the tensile resistance of all the MWNTs unanimously increases with increase in their outer tube diameter and has a direct relationship with it. Using this, one can use the Equation (3.17) to predict the tensile resistance of any configuration of DWNT using its outer tube diameter (d_o):

$$EA = 1.9464d_o - 0.8871, (1.0 \leq d_o \leq 3.5)\text{nm} \quad (3.17)$$

Figure 3.27 shows the influence of outer tube diameter of MWNT on its torsional stiffness. Like tensile resistance, torsional stiffness of the MWNT increases with increase in its outer tube diameter irrespective of the chirality. Till the outer tube diameter of 3 nm, the graph is parabolic. So for this part of the curve that is between the outer tube diameters of 1.0 till 3.0 nm Equation (3.18) can be conveniently used to predict the torsional stiffness of DWNT of any configuration:

$$GJ = 0.6485d_o^2 - 1.1798d_o + 0.6424, (1.0 \leq d_o \leq 3.0)\text{nm} \quad (3.18)$$

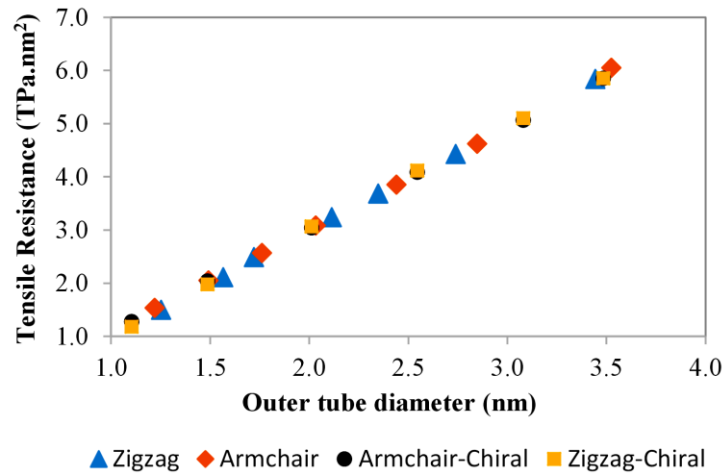


Figure 3.26 The relation between tensile resistance and the outer tube diameter of MWNT.

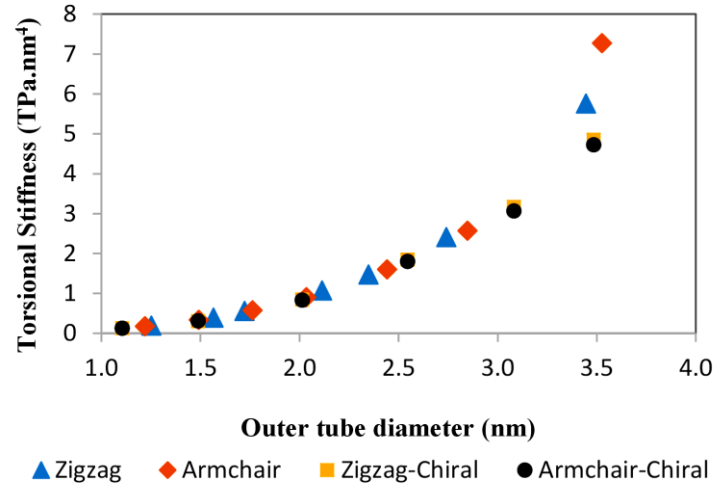


Figure 3.27 The relation between torsional stiffness and the outer tube diameter of MWNT.

3.4. Model Validation

For the purpose of validating the model, the simulation results obtained are compared with the literature values. Figure 3.28 and Figure 3.29 show the comparison.

Figure 3.28 shows the Young’s modulus reported by the previous studies and the present study. It indicates that Young’s modulus obtained in the present work are within the range of results reported by Wong et al. [41] and Salvetat et al. [42] in their experimental work that is between 0.69 – 1.87 TPa and 0.40 – 1.22 TPa respectively. It is worth noting that the results of this work are lower than the computational results reported by Li and Chou and Fan et al. [4,53]. This is because of the lower intershell spacing utilized in those cases (0.34 nm). Lower intershell spacing implies higher Young’s modulus as already explained in the section 3.3.1.2.

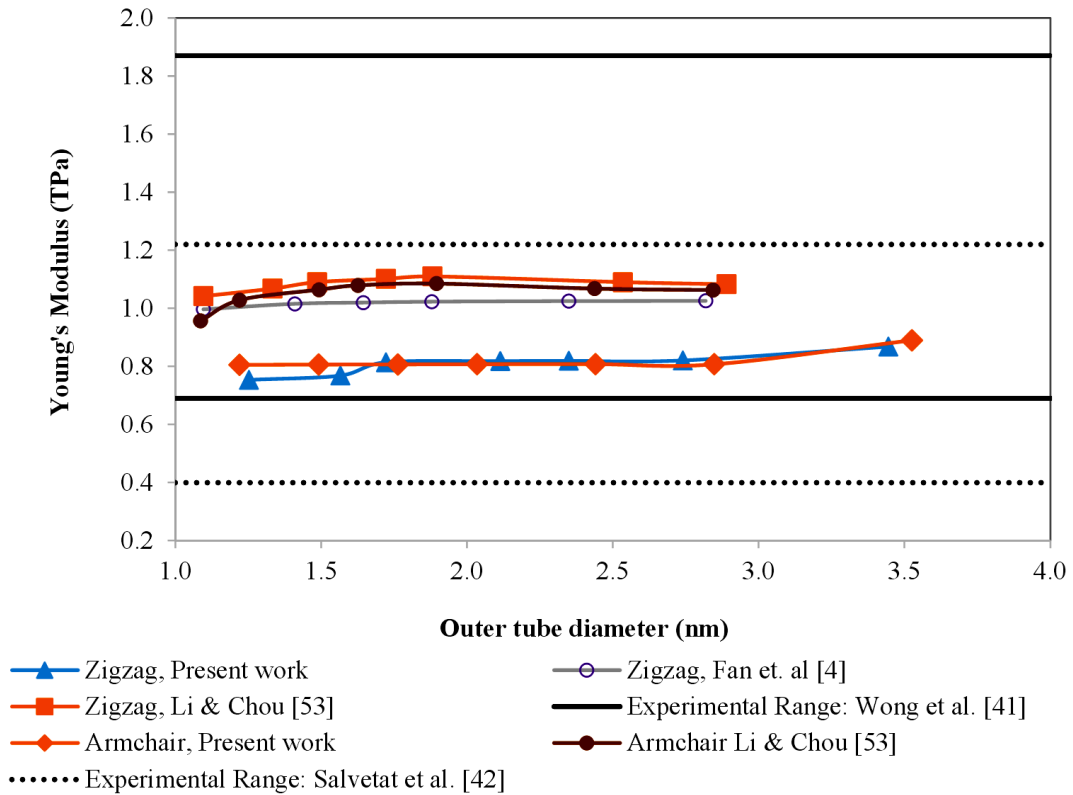


Figure 3.28 Comparison of the simulation results of Young’s modulus for monochiral armchair and zigzag MWNTs with the computational results computed by [4,53] and experimental results reported by [41,42].

Shear modulus of MWNT has not yet been determined experimentally so to verify the predicted results of shear modulus, comparison was made with the computational results reported by Li and Chou and Fan et al. [4,53]. Figure 3.29 shows that the predicted results are in close proximity to the previous reported results, the latter being a little greater than the one predicted in this research since the previous works did not take into account the variation of intershell spacing with the inner tube diameter. After the outer tube diameter of 3 nm, however, the predicted results of the research approach the published results owing to the intershell spacing approaching the similar value of 0.34 nm.

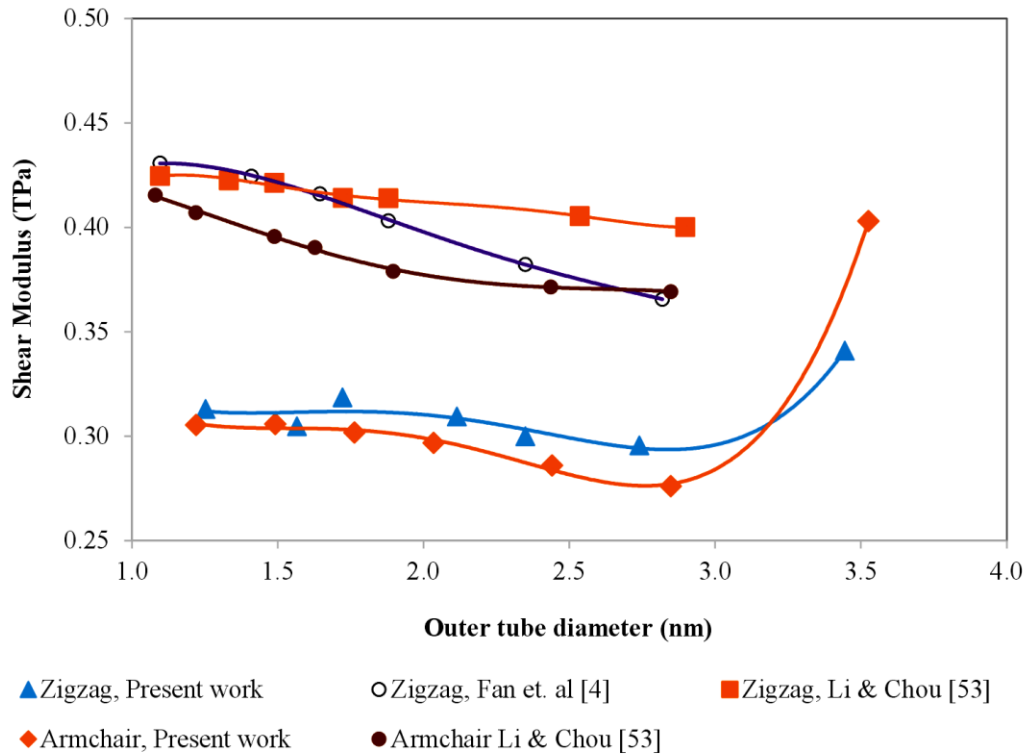


Figure 3.29 Comparison of the simulation results for monochiral armchair and zigzag MWNTs with the computational results computed by [4,5,53].

Table 3.15 shows the predicted average elastic moduli and shear moduli for armchair and zigzag DWNTs in comparison with the reported values obtained by computational modelling. It can be clearly seen that the predicted values are in sufficient agreement with the reported values, with the small discrepancy arising due to the difference in intershell spacing that has been taken into consideration in the current study.

Table 3.15 Reported and predicted average mechanical properties of DWNTs.

Reference	Year	Outer Tube Diameter (nm)	Intershell spacing (nm)	Thickness (nm)	Young's Modulus (TPa)	Shear Modulus (TPa)
Li & Chou [53]	2003	~ 1.0 - 3.0	0.34	0.34	0.956 - 1.085 [Armchair] 1.042 - 1.110 [Zigzag]	0.369 - 0.415 [Armchair] 0.400 - 0.425 [Zigzag]
Ghavamian et al. [5]	2012	~ 1.0	0.34	0.34	-	0.165 [Armchair] 0.33 [Zigzag]
Rahmandoust et al. [20]	2012	-	0.34	0.34	~ 1.05 [Armchair] ~ 1.03 [Zigzag]	0.448 [Armchair] 0.424 [Zigzag]
Brcic et al. [15]	2009	2.034	0.34	0.34	1.04	0.418
Fan et al. [4]	2009	~ 1.0 - 3.0	0.34	0.34	0.997 - 1.016 [Zigzag]	0.366 - 0.431 [Zigzag]
Lu [54]	1997		0.34	-	1.083	0.488
Present work	2016	~ 1.0 - 3.5	~ 0.40	0.34	0.819 [Armchair] 0.809 [Zigzag]	0.309 [Armchair] 0.312 [Zigzag]

CHAPTER 4

MULTI-WALLED CARBON NANOTUBE REINFORCED POLYMER COMPOSITES

To arrive at the mechanical properties of carbon nanotubes reinforced polymer composites, equivalent continuum structures of CNTs can be used [34]. The equivalent structure of MWNT, as reported in many studies, can be a linear elastic homogenous structure in the form of a fibre, a cylindrical tube whose outer radius is same as the radius of the outermost tube of the MWNT with the wall thickness being equal to $(\hat{d}_{002} \times N)$ nm where N is the number of tubes in MWNT and \hat{d}_{002} is the intershell spacing between the tubes, or a structure with N number of concentric tubes with vdW interaction among them [34]. In spite of not considering the van der Waals interaction, the second equivalent structure is popularly used by many researchers [34]. This chapter utilizes two different modelling approaches to model CNTRPs based on the representative volume element (RVE) that are built upon the models and properties of MWNT already established in Chapter 3. The properties predicted are then validated with the rule of mixtures.

4.1. Simulation Models of CNTRPs

RVEs have been made use of to study the fundamental and comprehensive interaction of a CNT with its surrounding matrix in CNTRPs [62]. A three-phase RVE of the CNTRP comprise the reinforcing material MWNT, the polymer matrix and the interphase region between the two [63]. Three different types of RVEs have been proposed by the researchers based on their cross-section; circular, square and hexagonal [62]. Figure 4.1 illustrates these different types of RVEs also depicting the constituents that make the RVE. Most of the researchers have used cylindrical RVEs with long CNTs spanning throughout the length of the matrix, because they are easier to model and for this reason they have been used in this study.

CNTRPs have been simulated using MSC Marc Mentat 2013 by two approaches that are elucidated in the Sections 4.1.1 and 4.1.2 respectively:

1. Discrete modelling approach

2. Continuum modelling approach

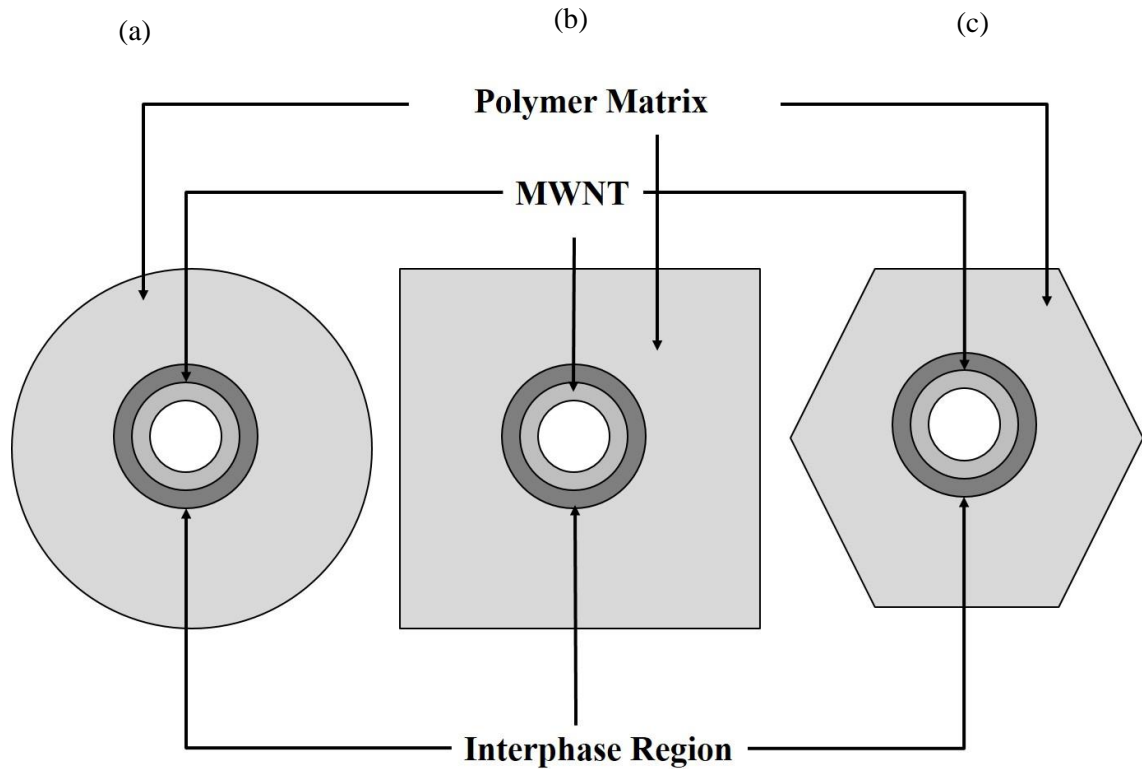


Figure 4.1 Types of RVE model (a) circular, (b) square (c) hexagonal together with its constituents.

4.1.1. Discrete Modelling Approach

In discrete modelling approach, CNT is modelled using beam/truss elements, matrix using solid elements and interphase using truss/beam/spring elements that connect the carbon atoms of CNT to the atoms of the matrix [65]. The elements used in modelling the interphase region are characterized using the L-J “6-12” potential [65]. Since this approach pictures weak non-bonded van der Waals interaction between the polymer matrix and CNT, it is also called non-bonded modelling approach.

The RVE in this approach was directly built upon the finite element model of MWNT already established in Chapter 3. Since minute addition of nanotubes in the polymer matrix drastically affects the resulting composites’ mechanical properties, volume fraction between 3 to 5 percent

is mostly observed in the polymer composites. This study in accordance with the study of Zuberi and Esat [28] uses 5 % as the volume fraction of MWNT, based on which the diameter of the RVE is deduced by the Equation (4.1):

$$d_{RVE} = \sqrt{\left[\frac{(d_o + 0.34)^2 - (d_i - 0.34)^2}{0.05} \right] + (d_i - 0.34)^2} \quad (4.1)$$

where d_{RVE} , d_o and d_i are the diameter of the RVE, outer tube diameter of the MWNT and inner tube diameter of the MWNT respectively.

The surrounding polymer matrix in the RVE is larger than the embedded MWNT in terms of volume at molecular scale so its simulations by atomistic modelling would thus require greater computational resources at nanoscale. But since the polymer is packed tightly in a much denser space as opposed to CNTs, they can be reasonably regarded as a continuum medium that can be modelled using solid elements. This method of modelling CNTRPs is also called multi-scale modelling due to the difference in length scales of modelling CNTs and the polymer matrix, the former being modelled in nano-scale while the latter in micro-scale [78].

To model the polymer matrix, Element (7) of the software has been employed as in Zuberi and Esat [28]. Element (7) is a 3D, eight-node distorted brick element with three degrees of freedom per each node [73]. The length of each element in the axial direction is kept as small as the length of the hexagons of the CNT [78]. The simulated polymer matrix is made to represent a homogenous isotropic epoxy material by incorporating its properties that taken are in line with the ones founded by Cease et al. [79] at ambient temperature that are: Young's modulus of Epoxy Resin $E_m = 3$ GPa and Poisson's ratio $\nu_m = 0.3$.

For the interphase region, it is probable that naturally the CNTs and polymer matrix are linked by means of van der Waals interaction [78]. There is no literature available about the exact thickness and mechanical properties of this region. Joshi and Upadhyay [63] studied the impact of different thickness of the interface region on the mechanical properties and concluded that greater the thickness of this region is, stronger is its effect on the stiffness of the composite.

Modelling and simulation of the van der Waals interaction between the matrix and CNT is done in a similar fashion as the interaction between the adjacent tubes of MWNT using Lennard-Jones “6-12” potential. For this reason, the interface thickness has been kept such that the distance between the atoms on the outermost layer of MWNT and the outer layer of interphase is equal to the critical distance $r_0 = 0.432$ nm so as to make the modelling of vdW links using springs simpler. The springs used have been characterized by the same force-displacement curve as shown in Figure 3.8 in the previous chapter. Figure 4.2 depicts the isometric and top view of the model mesh of a typical RVE simulated by discrete modelling approach containing the discrete model of zigzag DWNT (5, 0) – (16, 0), discretized continuum model of polymer matrix and the interphase region that portrays weak non-bonded interaction between the two. For the sake of simplicity, nodes have not been shown.

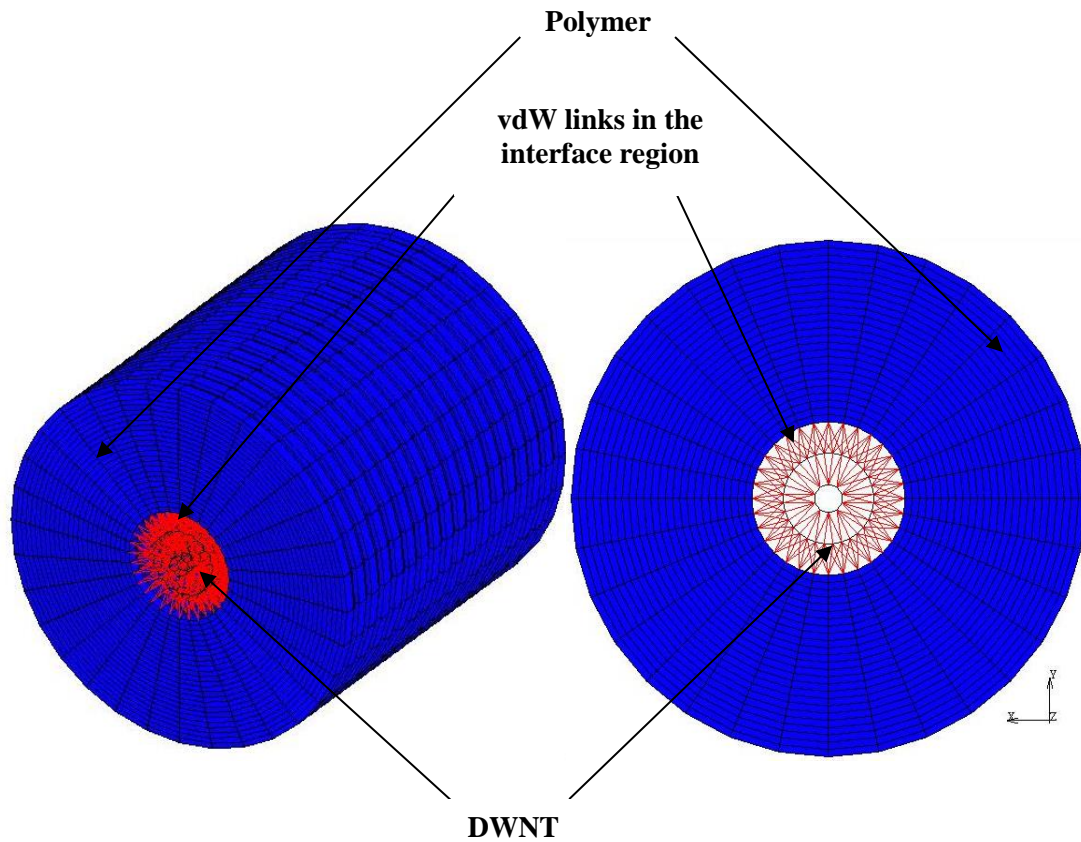


Figure 4.2 Finite Element model of RVE simulated by discrete modelling approach: (a) isometric view (b) Top view.

4.1.2. Continuum Modelling Approach

In the continuum modelling approach, the polymer matrix and embedded CNTs are modelled as continuum hollow cylinders made of solid elements. The interface region is also modelled as a solid cylinder filling the void between the matrix and the CNT due to the likelihood of the presence of strong covalent bond between the two [62,65]. Since this approach assumes covalent bonding, it is also called the perfect bonding modelling approach. Every entity in this approach is assumed to be a continua of linearly elastic, isotropic and homogenous materials with their respective elastic moduli and Poisson's ratio [62]. The properties of the polymer and thickness of the interphase region are kept the same as considered in the discrete modelling approach. The elastic modulus of the interphase region in line with the work of Zuberi and Esat [28] has been kept 20 GPa. As for the properties of the embedded MWNT, the respective numerical results obtained for the corresponding configurations used in the composites are incorporated.

Figure 4.3 illustrates the isometric and top view of the model mesh of a typical RVE simulated by continuum modelling approach containing the continuum model of zigzag DWNT (9, 0) – (20, 0), discretized continuum model of polymer matrix and the interphase region that portrays strong covalent bonding between the two. For the sake of conciseness, a coarser mesh without the nodes is shown.

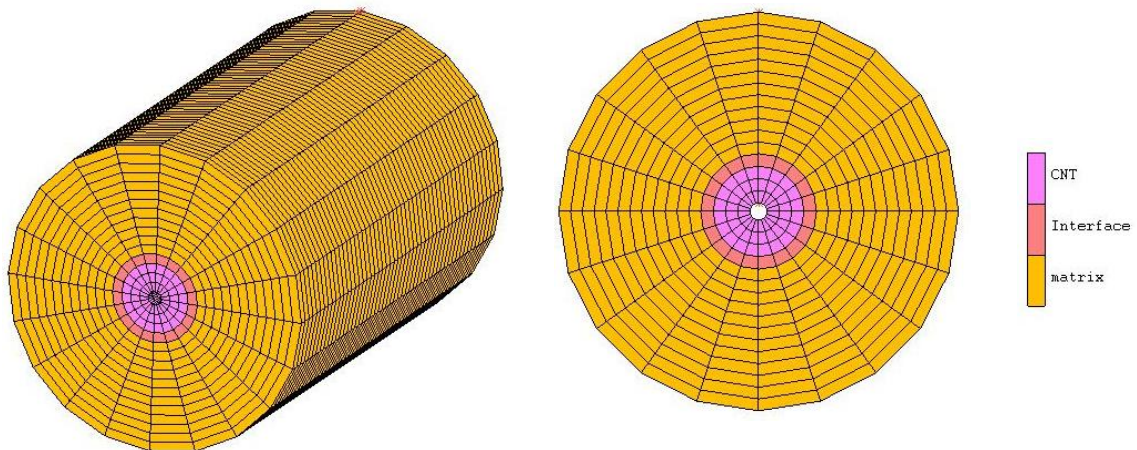


Figure 4.3 Finite Element model of RVE simulated by continuum modelling approach: (a) isometric view (b) Top view.

4.2. Model Validation

Not much theoretical work has been done on the epoxy composites reinforced with MWNTs. Thus, the validation of the models constructed by discrete and continuum modelling techniques are done by comparing the numerical results with the analytical results obtained from the rule of mixtures (ROM) and modified rule of mixtures respectively that are given by Equation (4.2) and Equation (4.3) respectively [63]. It is worth noting that ROM assumes weak bonding between the carbon nanotubes fibre and matrix and can thus be applied to compare the results found by discrete modelling approach whereas the modified rule of mixture supposes covalent bonding between the two and so is applied for comparison with the simulation results from continuum modelling.

$$E_c = E_f V_f + E_m (1 - V_f) \quad (4.2)$$

$$E_c = E_f V_f + E_m V_m + E_i V_i \quad (4.3)$$

where E_c , E_f , E_m and E_i are the elastic moduli of the composite, CNT fibre, polymer matrix, and interphase region, respectively, and V_f , V_m and V_i are the weights by volume of the CNT fibre, matrix and interphase respectively.

Table 4.1 compares the numerical results of the elastic modulus of the epoxy composite reinforced with monochiral zigzag and armchair DWNTs with the analytical results obtained by rule of mixtures and modified rule of mixtures. As can be seen, the obtained results from discrete and continuum modelling are in good agreement with the rule of mixtures, and the modified rule of mixtures, respectively; thereby providing a sort of validation for both models of the RVE. For the discrete modelling in particular, Young's moduli are observed to be slightly lower than the analytically found moduli, this is because of the weak vdW interaction especially in tensile loading which causes slippage between the tubes hindering the load to be transferred to the inner tubes [29].

Joshi and Upadhyay [29] investigated the influence of changing moduli of polymer matrix on the modulus of the composite. They observed an increasing linear trend between E_f / E_m and E_c / E_m . Figure 4.4 shows the linear trend between E_f / E_m and E_c / E_m as found by Joshi and Upadhyay [29].

Table 4.1 Comparison of numerical results of the elastic modulus of the epoxy composite reinforced with zigzag and armchair DWNTs with the analytical results by rule of mixtures and modified rule of mixture.

Reinforced DWNTs	E by Discrete Modelling (GPa)	E by ROM (GPa)	% difference	E by Continuum Modelling (GPa)	E by modified ROM (GPa)	% difference
Zigzag						
(5,0) - (16,0)	37.69	40.53	7.00	42.30	41.18	2.72
(9,0) - (20,0)	38.41	41.26	6.91	42.59	41.82	1.85
(17,0) - (27,0)	40.90	43.75	6.52	45.26	44.23	2.33
(25,0) - (35,0)	41.02	43.88	6.51	45.07	44.31	1.71
Armchair						
(3,3) - (9,9)	40.80	43.11	5.35	44.60	43.78	1.86
(5,5) - (11,11)	42.56	43.16	1.41	44.67	43.74	2.12
(9,9) - (15,15)	42.46	43.22	1.77	44.49	43.70	1.79
(15,15) - (21,21)	40.36	43.21	6.60	44.49	43.63	1.98

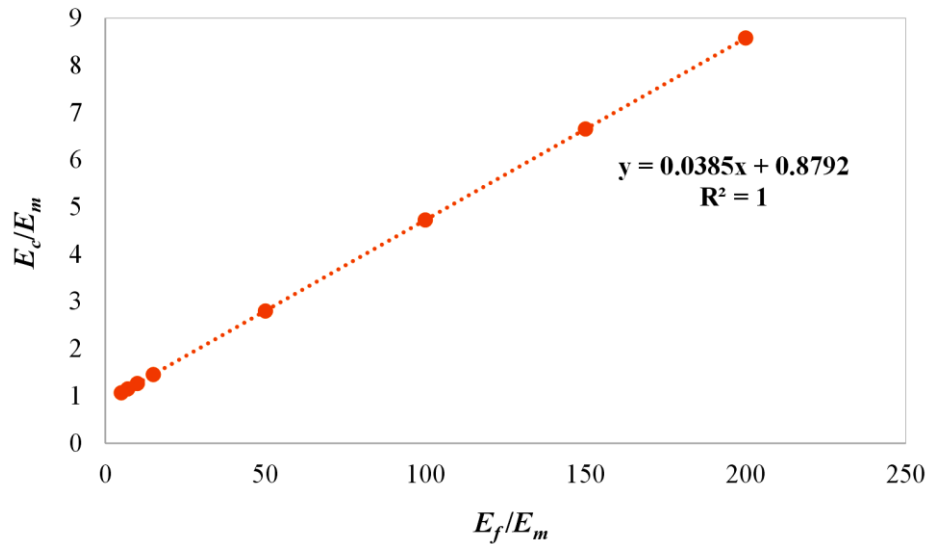


Figure 4.4 Illustration of the increasing linear trend between E_f/E_m and E_c/E_m as found by Joshi and Upadhyay [29].

This linear trend was extrapolated to incorporate the higher ratio of E_f/E_m and the results were compared with the numerical results. Table 4.2 compares these results. The results of the present study are slightly greater than the ones found by extrapolation from the trend acquired from the

results of Joshi and Upadhyay [29]. This is because of the higher interface thickness considered in the present study.

Table 4.2 Comparison of numerical results of the epoxy composite reinforced with zigzag DWNT against the extrapolated results from the trend found by Joshi and Upadhyay [29].

Reinforced DWNTs	E_f (GPa)	E_f/E_m	E_c/E_m		
			Present work by Discrete Modelling	Present work by Continuum Modelling	Joshi and Upadhyay [29]
Zigzag					
(5,0) - (16,0)	754	251	12.56	14.10	10.55
(9,0) - (20,0)	768	256	12.80	14.20	10.74
(17,0) - (27,0)	818	273	13.63	15.09	11.38
(25,0) - (35,0)	821	274	13.67	15.02	11.41
Armchair					
(3,3) - (9,9)	805	268	13.60	14.87	11.21
(5,5) - (11,11)	806	269	14.19	14.89	11.23
(9,9) - (15,15)	807	269	14.15	14.83	11.24
(15,15) - (21,21)	807	269	13.45	14.83	11.24

When it comes to validating the simulation results with the experimental results, there exists a large disparity. This is due to several other factors that have an impact on the properties of the composite:

- Dispersal and arrangement of the CNTs in the matrix which depend on the dispersion techniques at the fabrication stage but due to tendency of CNTs to agglomerate they are not perfectly oriented and aligned along the composite's axis.
- CNT's length which governs the effectiveness of the load transfer. Shorter CNTs are not as efficient as the long CNTs but since commercially available CNTs' lengths are within 100 nm to several micrometres, therefore the experimental results are based on an inefficient load transfer [31].
- Unknown properties of the interphase regions but it is anticipated that they possess properties that can increase the strength of the overall composite [66], are not considered in the present study.

The computational modelling provides an overestimate of the properties of the composite but the results are based on perfect dispersion and alignment of the CNTs and efficient load transfer. These results can therefore act as a benchmark for the researchers who are yet to achieve an ideal carbon nanotube reinforced polymer composite [28].

4.3. Numerical Results and Discussion

After validation of the two modelling techniques evaluated in the Section 4.1, it would be reasonable to employ continuum modelling technique as it complies more with the analytical and computational published results. Also, investigating the effect of chirality especially with polychiral configuration, it would be simpler to use the continuum modelling technique. The aim of the study is not to replicate the experimental results but to present a qualitative analysis of how the properties of the composite namely modulus of elasticity and Poisson's ratio vary based on computational modelling techniques.

Decision upon the mesh size of the continuum models of each configuration was based on sensitivity analysis that is given in APPENDIX C. Table 4.3 shows the characteristics of all the RVEs representing CNTRPs reinforced with DWNTs that have been investigated to bring into insight the influence of MWNT's helicity and diameter on their mechanical properties.

Table 4.3 Properties of CNTRP RVE models reinforced with DWNT.

Reinforced DWNTs	Diameter of DWNT		Interface Radius	RVE Diameter	Inner Chirality	Outer Chirality	Length (nm)
	d_i (nm)	d_o (nm)	r_i (nm)	(nm)	(deg)	(deg)	
Zigzag							
(9,0) - (20,0)	0.705	1.566	1.215	8.37	0	0	12.79
(12,0) - (22,0)	0.939	1.722	1.293	8.85	0	0	12.79
(17,0) - (27,0)	1.331	2.114	1.489	10.09	0	0	12.79
(20,0) - (30,0)	1.566	2.349	1.607	10.77	0	0	12.79
(25,0) - (35,0)	1.957	2.740	1.802	11.83	0	0	12.79
Armchair							
(5,5) - (11,11)	0.678	1.492	1.178	8.06	30	30	12.54
(7,7) - (13,13)	0.949	1.763	1.314	9.02	30	30	12.54
(9,9) - (15,15)	1.220	2.034	1.449	9.90	30	30	12.54
(12,12) - (18,18)	1.627	2.441	1.653	11.10	30	30	12.54
(15,15) - (21,21)	2.034	2.848	1.856	12.19	30	30	12.54
Armchair-chiral							
(5,5) - (16,5)	0.678	1.487	1.176	8.04	30	13.2	12.54
(9,9) - (20,9)	1.220	2.013	1.439	9.80	30	17.6	12.54
(13,13) - (24,13)	1.763	2.545	1.705	11.32	30	20.3	12.54
(17,17) - (28,17)	2.305	3.081	1.973	12.68	30	22.0	12.54
Zigzag-chiral							
(8,0) - (16,5)	0.626	1.487	1.176	8.08	0	13.2	12.79
(16,0) - (20,9)	1.253	2.013	1.439	9.74	0	17.6	12.79
(23,0) - (24,13)	1.801	2.545	1.705	11.22	0	20.3	12.79
(30,0) - (28,17)	2.349	3.081	1.973	12.55	0	22.0	12.79

4.3.1. Prediction of Young's Modulus of RVE

The Young's modulus of the RVE is evaluated by giving a fixed axial displacement (ΔL) of 0.1 nm at one of the ends of the RVE while keeping the other end fixed constraining any displacement or rotation in/about any axis at this end. Figure 4.5 shows the model mesh of the RVE reinforced with zigzag (9, 0) - (20, 0) DWNT showing these boundary conditions. The effective Young's modulus of the RVE can then be determined by Equation (4.4):

$$E_{RVE} = \frac{F_{RVE} L_{RVE}}{A_{RVE} \Delta L_{RVE}} \quad (4.4)$$

where E_{RVE} is the Young's modulus of the RVE, F_{RVE} is the total reaction force of the fixed nodes, L_{RVE} is the original length of the RVE, and A_{RVE} is the area of its cross-section that can be calculated by Equation (4.5):

$$A_{RVE} = \frac{\pi}{4} [(d_{RVE})^2 - (d_i - t)^2] \quad (4.5)$$

where d_{RVE} is the diameter of the RVE, d_i is the inner tube diameter of the MWNT and t is thickness of the tube of MWNT.

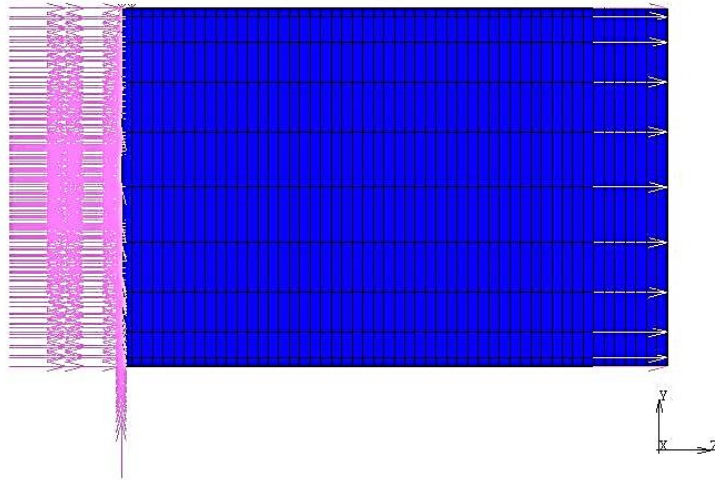


Figure 4.5 Model mesh of an RVE reinforced with zigzag (9, 0) - (20, 0) DWNT highlighting the imposed boundary conditions.

The impact of DWNT's diameter and helicity on the properties of CNTRPs have not been reported in the literature. Figure 4.6 illustrates how sensitive composite's elastic modulus is to the variation of DWNT's helicity and RVE diameter. Since RVE diameter is proportional to the diameter of DWNT, it would be pertinent to deduce the influence of MWNT diameter on the elastic modulus of the composite from the same figure. The figure shows that polychiral DWNTs are significantly affected by the DWNT diameter as opposed to monochiral DWNTs. For monochiral armchair DWNT, however, changing diameter does not significantly influence the Young's modulus of the composite. For polychiral DWNTs, changing diameter seems to influence the Young's modulus. This is because for every diameter increase in the polychiral case,

the outer chirality is not exactly same its effect shows up by an increase in RVE's elastic modulus. However, against the same RVE diameter greater than around 10.5 nm, it can be concluded that the RVE reinforced with polychiral zigzag-chiral has the greatest Young's modulus, followed by polychiral armchair-chiral DWNT and monochiral zigzag DWNT. RVE reinforced with monochiral armchair DWNT has the least Young's modulus for all RVE diameters greater than 9 nm.

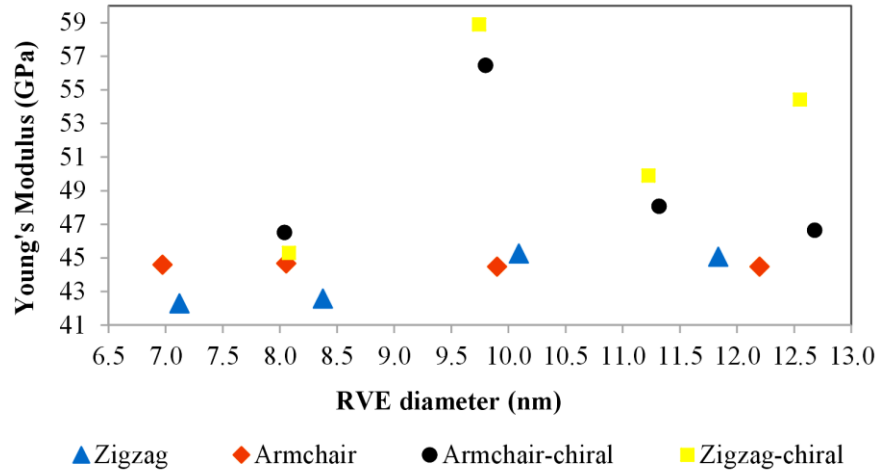


Figure 4.6 The relation between Young's Moduli and RVE diameter of CNTRPs reinforced with DWNT zigzag, armchair, armchair-chiral and zigzag-chiral configurations.

4.3.2. Prediction of Poisson's Ratio of RVE

From the same boundary conditions as used to define the RVE's modulus of elasticity, its Poisson's ratio is evaluated using Equation (4.6)

$$\nu_{RVE} = -\frac{\Delta d_{RVE}}{d_{RVE}} \times \frac{L_{RVE}}{\Delta L_{RVE}} \quad (4.6)$$

where ν_{RVE} is the Poisson's ratio of the RVE, Δd_{RVE} and ΔL_{RVE} are the changes in the the diameter and axial length respectively and d_{RVE} and L_{RVE} are the initial diameter and length of the RVE respectively.

Figure 4.7 shows the sensitivity of Poisson's ratio of the RVE to the influence of RVE diameter. For monochiral DWNTs, the effect is not significant. For polychiral DWNTs, however, the

increase in RVE diameter increases the Poisson's ratio quite significantly up to the RVE diameter of around 11 nm.

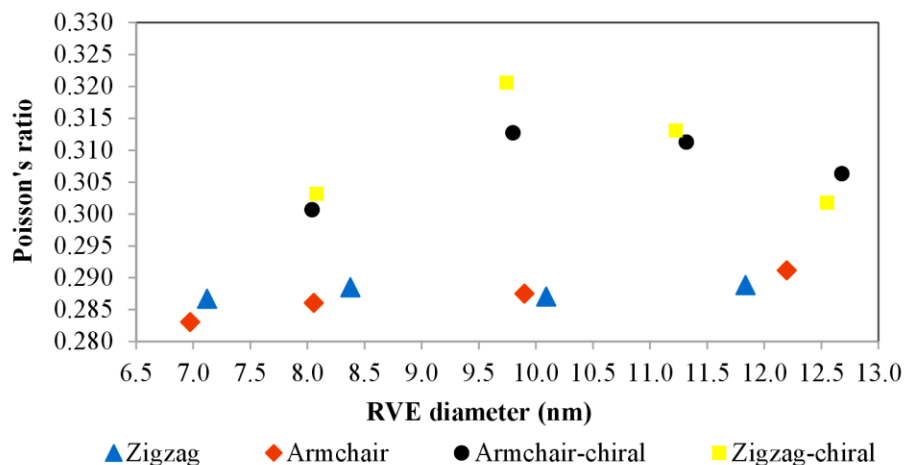


Figure 4.7 The relation between Poisson's ratio and RVE diameter of CNTRPs reinforced with DWNT zigzag, armchair, armchair-chiral and zigzag-chiral configurations.

Table 4.4 shows the influence of chirality on the Poisson's ratio of the RVEs that are approximately the same in diameter. For the same diameter, RVE reinforced with zigzag-chiral DWNTs possesses greatest Poisson's ratio, followed by armchair-chiral and monochiral zigzag DWNT. Monochiral armchair DWNT possesses the least Poisson's ratio. On average, the Poisson's ratio evaluated is in good agreement with the value evaluated by Joshi and Upadhyay [29] which is reported to be around 0.3.

Table 4.4 Effect of DWNT's helicity on the Poisson's ratio of the RVE about 8 nm in diameter.

Reinforced DWNTs	RVE diameter (nm)	Poisson's ratio (ν)
Zigzag	8.37	0.289
Armchair	8.06	0.286
Armchair-chiral	8.04	0.301
Zigzag-chiral	8.08	0.303

4.4. Predicted Reduction of Crude Oil Consumption

According to an estimation, every year 250 million barrels of crude can be saved by reducing a quarter of the car weight [80]. Using this estimation, the amount of crude oil saved by replacing the material of the car bumper made of fibre-glass/epoxy composite with MWNT/epoxy composite can be predicted. The volume fraction of the glass-fibre added in fibre-glass/epoxy composite is taken as 30 percent whereas the volume fraction of MWNT in MWNT/epoxy composite is taken as 5 percent as is required in their respective composites [25]. Table 4.5 shows the properties of glass fibre, DWNT (9, 0) - (20, 0) and neat epoxy resin along with their composites. Specific stiffness is the ratio of Young's modulus and density that helps gauge the performance of the materials.

Table 4.5 Properties of glass fibre, DWNT (9, 0) - (20, 0) and neat epoxy resin along with their composites. (Asterisked entities are taken from [79])

Material	Density (kg/m ³)	Young's Modulus (GPa)	Specific Stiffness (MPa/kg/m ³)
Neat Epoxy Resin	1100*	3*	2.73
Glass-fiber	2500*	70*	28.00
DWNT (9,0) - (20, 0)	1800*	768	426.67
Fiber/Epoxy Composite	1170	23.1	19.74
DWNT/Epoxy Composite	1135	42.592	37.53

The reciprocal of the specific stiffness gives the amount of mass required per unit strength and volume. This parameter indicates that using a DWNT/epoxy composite, mass of the bumper is reduced by 2 times that corresponds to 47 percent reduction in the weight of the car bumper which is equivalent to saving 470 million barrels of crude oil every year.

CHAPTER 5

CONCLUSIONS AND FUTURE WORK

5.1. Conclusions

Discovery of carbon nanotubes have spurred the research on sustainable materials that can offer desirable mechanical properties without damaging the ecosystem and environment. For this reason, nanotube-reinforced composites that are a new class of advanced materials are being extensively studied over the past two decades. Their high strength-to-weight ratio and improved biodegradability make them a promising material for various applications. Their use can help curb global environmental change ultimately leading to a low-carbon society. Despite all this, its use and its potential applications are still premature owing to the lack of knowledge about its exact properties. This thesis aimed at investigating the properties of multi-walled carbon nanotubes (MWNT) and the composites reinforced with MWNT together with how their properties can be affected by size, chirality, intershell spacing of MWNT and number of tubes in MWNT. Properties like shear strain and Poisson's ratio have also been reported which have not been done before.

This thesis was divided into two parts. The first part was dedicated to multi-walled carbon nanotubes whose individual tubes were simulated as a space-frame structure by means of equivalent-continuum modelling. Other than monochiral DWNTs, polychiral DWNTs have also been investigated in this study which have not been studied before. The intershell spacing was based on the empirical relationship with the inner diameter of the MWNT and unlike the previous studies have not been kept equal to 0.34 nm that is the spacing between the layers in graphite. The intershell interaction was modelled using springs characterized by Lennard-Jones potential. Finite element models for different configurations of MWNT were generated and their properties were evaluated against the effect of changing diameter, chirality, number of tubes and intershell spacing. The attained numerical results are in good agreement with those found in literature by experiments. As for the published values reported by the authors using computational techniques

are a bit greater than the ones obtained in the study due to the lower and constant intershell spacing. Nonetheless, the results were in close proximity, making the proposed model valid for use in the second part of the thesis.

From the results of MWNTs, it can be concluded that their mechanical properties are significantly affected by the changing intershell spacing. The smaller the inner radius, the greater the intershell spacing between the adjacent tubes that decreases both the Young's and shear moduli of the MWNTs and increases the shear strain. Also, changing the number of tubes in MWNT affects the mechanical properties significantly. Increasing the number of tubes of an MWNT, decreases both its shear and Young's moduli but also decreases its Poisson's ratio signifying the increased stability to lateral deformation. As for the change in outer tube diameter of the MWNT, increase in the diameter of MWNT increases its Young's modulus but decreases its shear modulus and also the shear strain. Also a novel relationship is developed for the tensile resistance (EA) and torsional stiffness (GJ) as a function of the outer tube diameter of DWNT for the range of 1 to 3 nm of outer diameter.

The second part of the thesis dealt with the modelling of multi-walled carbon nanotube reinforced polymer composites which built upon the already developed model of MWNT. The polymer chosen was epoxy resin owing to its current dominance in the market today and its suitability for use in the composite. The thickness of the interphase region has not been ascertained by experimental means as yet and so for the sake of simplicity and making use of the fact that thicker interphase region makes the composite stiffer, the value of the critical distance by Lennard-Jones force has been used. Two different modelling approaches were employed, namely, discrete and continuum, whose results were compared with those of the rule of mixtures and the modified rule of mixtures respectively. Since the continuum modelling approach complied more with the analytical results, it was chosen to evaluate the effect of diameter of MWNT and its chirality on all RVEs that has not been reported before in case of composite reinforced with MWNT. From the results obtained, composite reinforced with polychiral DWNTs are considered to be stiffer than monochiral DWNTs, whereas monochiral DWNTs are considered to be more resistant towards lateral deformation

5.2. Future Work

This research investigated the MWNT with up to 4 tubes. Commercialized MWNTs are larger and are comprised of 70-90 tubes. Modelling such MWNTs would need powerful computational hardware. Also, for smaller diameter MWNTs, the C-C bonds of the inner tubes are prone to distortion and so in the future these distorted tubes can also be investigated. Moreover, some MWNTs are produced with end caps that can be incorporated in the model to evaluate its effect on the properties of MWNTs.

In the present study, RVEs which depict perfect orientation and an ideal load transferring capability of the interphase are investigated. A more realistic approach can be incorporated by disorienting and misaligning the fibres to arrive at more realistic results. The interphase region which appears to glue the two parts of the composite together is anticipated to possess properties beneficial to the entire strength of the composite. Though, the properties of this region are still unknown but inclusion of polymer chains in the region is likely and can thus be investigated.

REFERENCES

- [1] Sharma VP, Agarwal V, Umar S, Singh AK. Polymer Composites Sustainability: Environmental Perspective, Future Trends and Minimization of Health Risk. IACSIT Press Singap., vol. 4, 2011, p. 259–61.
- [2] Haghgi AK, Thomas S. Carbon Nanotubes: Theoretical Concepts and Research Strategies for Engineers. 2015.
- [3] Lau AK-T, Hui D. The revolutionary creation of new advanced materials—carbon nanotube composites. *Compos Part B Eng* 2002;33:263–77. doi:10.1016/S1359-8368(02)00012-4.
- [4] Fan CW, Liu YY, Hwu C. Finite element simulation for estimating the mechanical properties of multi-walled carbon nanotubes. *Appl Phys A* 2009;95:819–31. doi:10.1007/s00339-009-5080-y.
- [5] Ghavamian A, Rahmandoust M, Öchsner A. On the determination of the shear modulus of carbon nanotubes. *Compos Part B Eng* 2013;44:52–9. doi:10.1016/j.compositesb.2012.07.040.
- [6] Gupta AK, Harsha SP. Analysis of Mechanical Properties of Carbon Nanotube Reinforced Polymer Composites Using Continuum Mechanics Approach. *Procedia Mater Sci* 2014;6:18–25. doi:10.1016/j.mspro.2014.07.004.
- [7] Jorio A, Dresselhaus G, Dresselhaus MS, editors. Carbon Nanotubes. vol. 111. Berlin, Heidelberg: Springer Berlin Heidelberg; 2008.
- [8] Rangel JH, Brostow W, Castano VM. Mechanical modeling of a single-walled carbon nanotube using the finite element approach 2013;4:276–81.
- [9] Kalamkarov AL, Georgiades AV, Rokkam SK, Veedu VP, Ghasemi-Nejhad MN. Analytical and numerical techniques to predict carbon nanotubes properties. *Int J Solids Struct* 2006;43:6832–54. doi:10.1016/j.ijsolstr.2006.02.009.
- [10] Tasis D, Tagmatarchis N, Bianco A, Prato M. Chemistry of carbon nanotubes. *Chem Rev* 2006;106:1105–36. doi:10.1021/cr050569o.
- [11] Belin T, Epron F. Characterization methods of carbon nanotubes: a review. *Mater Sci Eng B* 2005;119:105–18. doi:10.1016/j.mseb.2005.02.046.
- [12] Srivastava D, Wei C, Cho K. Nanomechanics of carbon nanotubes and composites. *Appl Mech Rev* 2003;56:215. doi:10.1115/1.1538625.

- [13] Ruoff RS, Qian D, Liu WK. Mechanical properties of carbon nanotubes: theoretical predictions and experimental measurements. *Comptes Rendus Phys* 2003;4:993–1008. doi:10.1016/j.crhy.2003.08.001.
- [14] Li C, Chou T-W. A structural mechanics approach for the analysis of carbon nanotubes. *Int J Solids Struct* 2003;40:2487–99. doi:10.1016/S0020-7683(03)00056-8.
- [15] Brcic M, Canadija M, Brnic J, Lanc D, Krscanski S, Vukelic G. FE modelling of multi-walled carbon nanotubes. *Est J Eng* 2009;15:77. doi:10.3176/eng.2009.2.01.
- [16] Zuberi MJS, Esat V. Estimating the Effect of Chirality and Size on the Mechanical Properties of Carbon Nanotubes Through Finite Element Modelling, ASME; 2014, p. V001T04A002. doi:10.1115/ESDA2014-20156.
- [17] Ganesh EN. Single Walled and Multi Walled Carbon Nanotube Structure, Synthesis and Applications. *Int J Innov Technol Explor Eng IJITEE* 2013;2:311–20.
- [18] Lu X, Hu Z. Mechanical property evaluation of single-walled carbon nanotubes by finite element modeling. *Compos Part B Eng* 2012;43:1902–13. doi:10.1016/j.compositesb.2012.02.002.
- [19] Bichoutskaia E, Heggie MI, Popov AM, Lozovik YE. Interwall interaction and elastic properties of carbon nanotubes. *Phys Rev B* 2006;73:45435. doi:10.1103/PhysRevB.73.045435.
- [20] Rahmandoust M, Ochsner A. On finite element modeling of single- and multi-walled carbon nanotubes. *J Nanosci Nanotechnol* 2012;12:8129–36.
- [21] Szabó A, Perri C, Csató A, Giordano G, Vuono D, Nagy JB. Synthesis Methods of Carbon Nanotubes and Related Materials. *Materials* 2010;3:3092–140. doi:10.3390/ma3053092.
- [22] Camargo PHC, Satyanarayana KG, Wypych F. Nanocomposites: synthesis, structure, properties and new application opportunities. *Mater Res* 2009;12:1–39. doi:10.1590/S1516-14392009000100002.
- [23] Hussain F. Review article: Polymer-matrix Nanocomposites, Processing, Manufacturing, and Application: An Overview. *J Compos Mater* 2006;40:1511–75. doi:10.1177/0021998306067321.
- [24] Cristina B, Ion D, Adriana S, George P. Nanocomposites as Advanced Materials for Aerospace Industry. *INCAS Bull* 2012;4:57–72. doi:10.13111/2066-8201.2012.4.4.6.
- [25] Breuer O, Sundararaj U. Big returns from small fibers: A review of polymer/carbon nanotube composites. *Polym Compos* 2004;25:630–45. doi:10.1002/pc.20058.

- [26] Thostenson ET, Chou T-W. Aligned multi-walled carbon nanotube-reinforced composites: processing and mechanical characterization. *J Phys Appl Phys* 2002;35:L77. doi:10.1088/0022-3727/35/16/103.
- [27] Wagner HD, Vaia RA. Nanocomposites: issues at the interface. *Mater Today* 2004;7:38–42. doi:10.1016/S1369-7021(04)00507-3.
- [28] Zuberi MJS, Esat V. Investigating the mechanical properties of single walled carbon nanotube reinforced epoxy composite through finite element modelling. *Compos Part B Eng* 2015;71:1–9. doi:10.1016/j.compositesb.2014.11.020.
- [29] Joshi P, Upadhyay SH. Evaluation of elastic properties of multi walled carbon nanotube reinforced composite. *Comput Mater Sci* 2014;81:332–8. doi:10.1016/j.commatsci.2013.08.034.
- [30] Du J-H. The present status and key problems of carbon nanotube based polymer composites. *EXPRESS Polym Lett* 2007;1:253–73. doi:10.3144/expresspolymlett.2007.39.
- [31] Esawi AMK, Farag MM. Carbon nanotube reinforced composites: Potential and current challenges. *Mater Des* 2007;28:2394–401. doi:10.1016/j.matdes.2006.09.022.
- [32] Mohamed B. *Handbook of Research on Nanoscience, Nanotechnology, and Advanced Materials*. IGI Global; 2014.
- [33] TASC. Dissemination of Results | Project | Technology Research Association for Single Wall Carbon Nanotubes n.d. <http://www.tasc-nt.or.jp/en/project/result.html> (accessed August 6, 2016).
- [34] Batra RC, Sears A. Continuum models of multi-walled carbon nanotubes. *Int J Solids Struct* 2007;44:7577–96. doi:10.1016/j.ijsolstr.2007.04.029.
- [35] Zuberi MJS. *Computational modelling of carbon nanotube reinforced polymer composites*. M.S. Middle East Technical University, 2014.
- [36] Journet C, Picher M, Jourdain V. Carbon nanotube synthesis: from large-scale production to atom-by-atom growth. *Nanotechnology* 2012;23:142001. doi:10.1088/0957-4484/23/14/142001.
- [37] Vigolo B, Hrol C. Processing Carbon Nanotubes. In: Yellampalli S, editor. *Carbon Nanotub. - Synth. Charact. Appl.*, InTech; 2011.
- [38] Salvétat JP, Kulik AJ, Bonard JM, Briggs GAD, Stöckli T, Méténier K, et al. Elastic Modulus of Ordered and Disordered Multiwalled Carbon Nanotubes. *Adv Mater* 1999;11:161–5.

- [39] Duncan R, Stolojan V, Lekakou C. Manufacture of Carbon Multi-Walled Nanotubes by the Arc Discharge Technique. *World Congr. Eng.* 2007, vol. II, London, U.K.: IAENG; 2007.
- [40] Thostenson ET, Ren Z, Chou T-W. Advances in the science and technology of carbon nanotubes and their composites: a review. *Compos Sci Technol* 2001;61:1899–912. doi:10.1016/S0266-3538(01)00094-X.
- [41] Wong EW. Nanobeam Mechanics: Elasticity, Strength, and Toughness of Nanorods and Nanotubes. *Science* 1997;277:1971–5. doi:10.1126/science.277.5334.1971.
- [42] Salvétat J-P, Bonard J-M, Thomson NH, Kulik AJ, Forró L, Benoit W, et al. Mechanical properties of carbon nanotubes. *Appl Phys Mater Sci Process* 1999;69:255–60. doi:10.1007/s003390050999.
- [43] Ruland W, Schaper AK, Hou H, Greiner A. Multi-wall carbon nanotubes with uniform chirality: evidence for scroll structures 2003;41:423–7. doi:10.1016/S0008-6223(02)00342-1.
- [44] Friedrichs S, Windle AH, Koziol K, Ducati C, Midgley PA. Single-Chirality Multi-walled Carbon Nanotubes. *Microsc Microanal* 2005;11:1536–1537. doi:10.1017/S1431927605503519.
- [45] Karthikeyan S, Mahalingam P, Karthik M. Large Scale Synthesis of Carbon Nanotubes. *E-J Chem* 2009;6.
- [46] Gerard Lavin J, Subramoney S, Ruoff RS, Berber S, Tománek D. Scrolls and nested tubes in multiwall carbon nanotubes. *Carbon* 2002;40:1123–30. doi:10.1016/S0008-6223(02)00050-7.
- [47] Poncharal P. Electrostatic Deflections and Electromechanical Resonances of Carbon Nanotubes. *Science* 1999;283:1513–6. doi:10.1126/science.283.5407.1513.
- [48] Treacy MMJ, Ebbesen TW, Gibson JM. Exceptionally high Young's modulus observed for individual carbon nanotubes. *Nature* 1996;381:678–80. doi:10.1038/381678a0.
- [49] Krishnan A, Dujardin E, Ebbesen TW, Yianilos PN, Treacy MMJ. Young's modulus of single-walled nanotubes. *Phys Rev B* 1998;58:14013–9. doi:10.1103/PhysRevB.58.14013.
- [50] Cooper CA, Young RJ, Halsall M. Investigation into the deformation of carbon nanotubes and their composites through the use of Raman spectroscopy. *Compos Part Appl Sci Manuf* 2001;32:401–11. doi:10.1016/S1359-835X(00)00107-X.
- [51] Rafiee R, Moghadam RM. On the modeling of carbon nanotubes: A critical review. *Compos Part B Eng* 2014;56:435–49. doi:10.1016/j.compositesb.2013.08.037.

- [52] He XQ, Kitipornchai S, Wang CM, Liew KM. Modeling of van der Waals force for infinitesimal deformation of multi-walled carbon nanotubes treated as cylindrical shells. *Int J Solids Struct* 2005;42:6032–47. doi:10.1016/j.ijsolstr.2005.03.045.
- [53] Li C, Chou T. Elastic moduli of multi-walled carbon nanotubes and the effect of van der Waals forces. *Compos Sci Technol* 2003;63:1517–24. doi:10.1016/S0266-3538(03)00072-1.
- [54] Lu JP. Elastic Properties of Carbon Nanotubes and Nanoropes. *Phys Rev Lett* 1997;79:1297–300. doi:10.1103/PhysRevLett.79.1297.
- [55] Montazeri A, Montazeri N. Viscoelastic and mechanical properties of multi walled carbon nanotube/epoxy composites with different nanotube content. *Mater Des* 2011;32:2301–7. doi:10.1016/j.matdes.2010.11.003.
- [56] Leon V, Parret R, Almairac R, Alvarez L, Babaa M-R, Doyle BP, et al. Spectroscopic study of double-walled carbon nanotube functionalization for preparation of carbon nanotube / epoxy composites. *Carbon* 2012;50:4987–94. doi:10.1016/j.carbon.2012.06.007.
- [57] Hsiao K-T, Alms J, Advani SG. Use of epoxy/multiwalled carbon nanotubes as adhesives to join graphite fibre reinforced polymer composites. *Nanotechnology* 2003;14:791. doi:10.1088/0957-4484/14/7/316.
- [58] Zhu J, Peng H, Rodriguez-Macias F, Margrave JL, Khabashesku VN, Imam AM, et al. Reinforcing Epoxy Polymer Composites Through Covalent Integration of Functionalized Nanotubes. *Adv Funct Mater* 2004;14:643–8. doi:10.1002/adfm.200305162.
- [59] Allaoui A. Mechanical and electrical properties of a MWNT/epoxy composite. *Compos Sci Technol* 2002;62:1993–8. doi:10.1016/S0266-3538(02)00129-X.
- [60] Ying Z, Du J-H, Bai S, Li F, Liu C, Cheng H-M. MECHANICAL PROPERTIES OF SURFACTANT-COATING CARBON NANOFIBER/EPOXY COMPOSITE. *Int J Nanosci* 2002;1:425–30. doi:10.1142/S0219581X02000449.
- [61] Montazeri A, Javadpour J, Khavandi A, Tcharkhtchi A, Mohajeri A. Mechanical properties of multi-walled carbon nanotube/epoxy composites. *Mater Des* 2010;31:4202–8. doi:10.1016/j.matdes.2010.04.018.
- [62] Karimzadeh F, Ziaei-Rad S, Adibi S. Modeling Considerations and Material Properties Evaluation in Analysis of Carbon Nano-Tubes Composite. *Metall Mater Trans B* 2007;38:695–705. doi:10.1007/s11663-007-9065-y.
- [63] Joshi P, Upadhyay S. Effect of interphase on elastic behavior of multiwalled carbon nanotube reinforced composite. *Comput Mater Sci* 2014;87:267–73. doi:10.1016/j.commatsci.2014.02.029.

- [64] Ayatollahi MR, Shadlou S, Shokrieh MM. Multiscale modeling for mechanical properties of carbon nanotube reinforced nanocomposites subjected to different types of loading. *Compos Struct* 2011;93:2250–9. doi:10.1016/j.compstruct.2011.03.013.
- [65] Rafiee R, Maleki Moghadam R. Simulation of impact and post-impact behavior of carbon nanotube reinforced polymer using multi-scale finite element modeling. *Comput Mater Sci* 2012;63:261–8. doi:10.1016/j.commatsci.2012.06.010.
- [66] Han F, Azdoud Y, Lubineau G. Computational modeling of elastic properties of carbon nanotube/polymer composites with interphase regions. Part I: Micro-structural characterization and geometric modeling. *Comput Mater Sci* 2014;81:641–51. doi:10.1016/j.commatsci.2013.07.036.
- [67] Zuberi MJS, Esat V. Evaluating the effects of size and chirality on the mechanical properties of single-walled carbon nanotubes through equivalent-continuum modelling. *Proc Inst Mech Eng Part J Mater Des Appl* 2015:1464420715588217. doi:10.1177/1464420715588217.
- [68] Odegard GM, Gates TS, Nicholson LM, Wise KE. Equivalent-Continuum Modeling With Application to Carbon Nanotubes. 2002.
- [69] Hehre WJ. *A Guide to Molecular Mechanics and Quantum Chemical Calculations*. n.d.
- [70] Rappe AK, Casewit CJ, Colwell KS, Goddard WA, Skiff WM. UFF, a full periodic table force field for molecular mechanics and molecular dynamics simulations. *J Am Chem Soc* 1992;114:10024–35. doi:10.1021/ja00051a040.
- [71] Tserpes KI, Papanikos P. Finite element modeling of single-walled carbon nanotubes. *Compos Part B Eng* 2005;36:468–77. doi:10.1016/j.compositesb.2004.10.003.
- [72] Scarpa F, Adhikari S. A mechanical equivalence for Poisson's ratio and thickness of C–C bonds in single wall carbon nanotubes. *J Phys Appl Phys* 2008;41:85306. doi:10.1088/0022-3727/41/8/085306.
- [73] Marc® 2013.1. Volume B: Element Library. MSC Software Corporation; 2013.
- [74] Charlier J-C, Gonze X, Michenaud J-P. Graphite Interplanar Bonding: Electronic Delocalization and van der Waals Interaction. *EPL Europhys Lett* 1994;28:403. doi:10.1209/0295-5075/28/6/005.
- [75] Kiang C-H, Endo M, Ajayan PM, Dresselhaus G, Dresselhaus MS. Size Effects in Carbon Nanotubes. *Phys Rev Lett* 1998;81:1869–72. doi:10.1103/PhysRevLett.81.1869.
- [76] Walther JH, Jaffe R, Halicioglu T, Koumoutsakos P. Carbon Nanotubes in Water: Structural Characteristics and Energetics. *J Phys Chem B* 2001;105:9980–7. doi:10.1021/jp011344u.

- [77] Arroyo M, Belytschko T. Nonlinear Mechanical Response and Rippling of Thick Multiwalled Carbon Nanotubes. *Phys Rev Lett* 2003;91. doi:10.1103/PhysRevLett.91.215505.
- [78] Shokrieh MM, Rafiee R. On the tensile behavior of an embedded carbon nanotube in polymer matrix with non-bonded interphase region. *Compos Struct* 2010;92:647–52. doi:10.1016/j.compstruct.2009.09.033.
- [79] Cease H, Derwent PF, Diehl HT, Fast J, Finley D. Measurement of mechanical properties of three epoxy adhesives at cryogenic temperatures for CCD construction. *Fermi Natl Accel Lab* 2006.
- [80] Davoodi MM, Sapuan SM, Ahmad D, Ali A, Khalina A, Jonoobi M. Mechanical properties of hybrid kenaf/glass reinforced epoxy composite for passenger car bumper beam. *Mater Des* 2010;31:4927–32. doi:10.1016/j.matdes.2010.05.021.

APPENDIX A

CHARACTERISTICS OF SIMULATED FINITE ELEMENT MODELS

Table A.1 Characteristics of the simulated DWNT models.

DWNTs	Diameter		Intershell	Inner	Outer	Length <i>L</i> (nm)	No. of Nodes	No. of Elements	No. of Springs
	<i>d_i</i> (nm)	<i>d_o</i> (nm)	Spacing <i>d₀₀₂</i> (nm)	Chirality (deg)	Chirality (deg)				
Monochiral									
Zigzag									
(5,0) - (16,0)	0.39	1.25	0.431	0	0	12.78	2541	3780	3840
(9,0) - (20,0)	0.70	1.57	0.431	0	0	12.78	3509	5220	3509
(12,0) - (22,0)	0.94	1.72	0.391	0	0	12.78	4114	6120	13260
(17,0) - (27,0)	1.33	2.11	0.391	0	0	12.78	5324	7920	17130
(20,0) - (30,0)	1.57	2.35	0.391	0	0	12.78	6050	9000	18900
(25,0) - (35,0)	1.96	2.74	0.391	0	0	12.78	7260	10800	23850
(35,0) - (44,0)	2.74	3.44	0.352	0	0	12.78	9559	14220	44160
Armchair									
(3,3) - (9,9)	0.41	1.22	0.407	30	30	12.54	2472	3684	7956
(5,5) - (11,11)	0.68	1.49	0.407	30	30	12.54	3296	4912	9792
(7,7) - (13,13)	0.95	1.76	0.407	30	30	12.54	4120	6140	12444
(9,9) - (15,15)	1.22	2.03	0.407	30	30	12.54	4944	7368	15300
(12,12) - (18,18)	1.63	2.44	0.407	30	30	12.54	6180	9210	19584
(15,15) - (21,21)	2.03	2.85	0.407	30	30	12.54	7416	11052	22338
(21,21) - (26,26)	2.85	3.53	0.339	30	30	12.54	9682	14429	53754
Polychiral									
Armchair-Chiral									
(2,2) - (13,2)	0.27	1.10	0.417	30	7.1	11.80	1984	2954	3600
(5,5) - (16,5)	0.68	1.49	0.405	30	13.2	8.00	2104	3122	5561
(9,9) - (20,9)	1.22	2.01	0.396	30	17.6	10.80	4246	6319	13384
(13,13) - (24,13)	1.76	2.55	0.391	30	20.3	13.77	7166	10682	24596
(17,17) - (28,17)	2.31	3.08	0.388	30	22.0	13.53	8879	13234	31909
(20,20) - (31,20)	2.71	3.48	0.386	30	22.9	13.65	10273	15317	37879
Zigzag-Chiral									
(3,0) - (13,2)	0.23	1.10	0.435	0	7.1	11.80	1934	2880	2023
(8,0) - (16,5)	0.63	1.49	0.431	0	13.2	8.00	2044	3030	2906
(16,0) - (20,9)	1.25	2.01	0.380	0	17.6	10.80	4276	6365	16590
(23,0) - (24,13)	1.80	2.55	0.372	0	20.3	13.77	7218	10763	30901
(30,0) - (28,17)	2.35	3.08	0.366	0	22.0	13.53	8941	13316	40634
(35,0) - (31,20)	2.74	3.48	0.372	0	22.9	13.65	10343	15427	44671

Table A.2 Characteristics of the simulated continuum RVE models.

Reinforced DWNTs	Diameter of DWNT		Inner Chirality (deg)	Outer Chirality (deg)	Interface diameter (nm)	RVE Diameter d_{RVE} (nm)	Length L (nm)	No. of nodes	No. of Elements
	d_i (nm)	d_o (nm)							
Zigzag									
(5,0) - (16,0)	0.391	1.253	0	0	2.117	7.12	7.38	69750	63000
(9,0) - (20,0)	0.705	1.566	0	0	2.430	8.37	7.38	93000	85500
(17,0) - (27,0)	1.331	2.114	0	0	2.978	10.09	7.38	93000	85500
(25,0) - (35,0)	1.957	2.740	0	0	3.605	11.83	7.38	93000	85500
Armchair									
(3,3) - (9,9)	0.407	1.220	30	30	2.085	6.97	7.38	93000	85500
(5,5) - (11,11)	0.678	1.492	30	30	2.356	8.06	7.38	93000	85500
(9,9) - (15,15)	1.220	2.034	30	30	2.899	9.90	7.38	93000	85500
(15,15) - (21,21)	2.034	2.848	30	30	3.712	12.19	7.38	93000	85500
Armchair-Chiral									
(5,5) - (16,5)	0.678	1.487	30	13.2	2.352	8.04	7.38	93000	85500
(9,9) - (20,9)	1.220	2.013	30	17.6	2.877	9.80	7.38	93000	85500
(13,13) - (24,13)	1.763	2.545	30	20.3	3.410	11.32	7.38	93000	85500
(17,17) - (28,17)	2.305	3.081	30	22.0	3.946	12.68	7.38	93000	85500
Zigzag-chiral									
(8,0) - (16,5)	0.626	1.487	0	13.2	2.352	8.08	7.38	93000	85500
(16,0) - (20,9)	1.253	2.013	0	17.6	2.877	9.74	7.38	93000	85500
(23,0) - (24,13)	1.801	2.545	0	20.3	3.410	11.22	7.38	93000	85500
(30,0) - (28,17)	2.349	3.081	0	22.0	3.946	12.55	7.38	93000	85500

APPENDIX B

IMPORTANT NUMERICAL RESULTS

Table B.1 Predicted Young's moduli of Monochiral and Polychiral DWNTs.

DWNTs	Diameter		d_{002}	Inner Chirality	Outer Chirality	L	ΔL	F	E	EA
	d_i	d_o								
	(nm)	(nm)	(nm)	(deg)	(deg)	(nm)	(nm)	(nN)	(TPa)	(TPa.nm ²)
Zigzag										
(5,0) - (16,0)	0.39	1.25	0.431	0	0	12.8	0.1	11.735	0.754	1.500
(9,0) - (20,0)	0.70	1.57	0.431	0	0	12.8	0.1	16.521	0.768	2.111
(12,0) - (22,0)	0.94	1.72	0.391	0	0	12.8	0.1	19.484	0.814	2.490
(17,0) - (27,0)	1.33	2.11	0.391	0	0	12.8	0.1	25.331	0.818	3.237
(20,0) - (30,0)	1.57	2.35	0.391	0	0	12.8	0.1	28.826	0.819	3.684
(25,0) - (35,0)	1.96	2.74	0.391	0	0	12.8	0.1	34.650	0.821	4.428
(35,0) - (44,0)	2.74	3.44	0.352	0	0	12.8	0.1	45.682	0.868	5.838
Average:									0.809	3.327
Armchair										
(3,3) - (9,9)	0.41	1.22	0.407	30	30	12.54	0.1	12.257	0.805	1.538
(5,5) - (11,11)	0.68	1.49	0.407	30	30	12.54	0.1	16.360	0.806	2.052
(7,7) - (13,13)	0.95	1.76	0.407	30	30	12.54	0.1	20.464	0.807	2.567
(9,9) - (15,15)	1.22	2.03	0.407	30	30	12.54	0.1	24.574	0.807	3.082
(12,12) - (18,18)	1.63	2.44	0.407	30	30	12.54	0.1	30.733	0.808	3.855
(15,15) - (21,21)	2.03	2.85	0.407	30	30	12.54	0.1	36.848	0.807	4.622
(21,21) - (26,26)	2.85	3.53	0.339	30	30	12.54	0.1	48.220	0.890	6.048
Average:									0.819	3.395
Armchair-Chiral										
(2,2) - (13,2)	0.27	1.10	0.417	30	7.1	11.80	0.1	10.800	0.780	1.274
(5,5) - (16,5)	0.68	1.49	0.405	30	13.2	8.00	0.1	25.509	0.806	2.041
(9,9) - (20,9)	1.22	2.01	0.396	30	17.6	10.80	0.1	28.182	0.814	3.044
(13,13) - (24,13)	1.76	2.55	0.391	30	20.3	13.77	0.1	29.662	0.825	4.084
(17,17) - (28,17)	2.31	3.08	0.388	30	22.0	13.53	0.1	37.439	0.822	5.065
(20,20) - (31,20)	2.71	3.48	0.386	30	22.9	13.65	0.1	42.872	0.828	5.852
Average:									0.812	3.560
Zigzag-Chiral										
(3,0) - (13,2)	0.23	1.10	0.435	0	7.1	11.80	0.1	10.029	0.726	1.183
(8,0) - (16,5)	0.63	1.49	0.431	0	13.2	8.00	0.1	24.718	0.773	1.977
(16,0) - (20,9)	1.25	2.01	0.380	0	17.6	10.80	0.1	28.413	0.831	3.069
(23,0) - (24,13)	1.80	2.55	0.372	0	20.3	13.77	0.1	29.896	0.847	4.117
(30,0) - (28,17)	2.35	3.08	0.366	0	22.0	13.53	0.1	37.696	0.847	5.100
(35,0) - (31,20)	2.74	3.48	0.372	0	22.9	13.65	0.1	42.887	0.841	5.854
Average:									0.811	3.550

Table B.2 Predicted Young's moduli of Monochiral triple walled carbon nanotubes.

TWNTs	Diameter		L (nm)	ΔL (nm)	F (nN)	E (TPa)	EA (TPa nm ²)
	d_i (nm)	d_o (nm)					
Zigzag							
(5,0) - (16,0) - (26,0)	0.39	2.0	12.78	0.1	26.725	0.771	3.42
(9,0) - (20,0) - (30,0)	0.70	2.3	12.78	0.1	33.968	0.779	4.34
(12,0) - (22,0) - (32,0)	0.94	2.5	12.78	0.1	37.975	0.799	4.85
(17,0) - (27,0) - (37,0)	1.33	2.9	12.78	0.1	46.735	0.801	5.97
(20,0) - (30,0) - (40,0)	1.57	3.1	12.78	0.1	51.969	0.802	6.64
(25,0) - (35,0) - (44,0)	1.96	3.4	12.78	0.1	60.141	0.836	7.69
Average:						0.798	5.485
Armchair							
(3,3) - (9,9) - (15,15)	0.41	2.0	12.54	0.1	27.655	0.784	3.47
(5,5) - (11,11) - (17,17)	0.68	2.3	12.54	0.1	33.800	0.784	4.24
(7,7) - (13,13) - (19,19)	0.95	2.6	12.54	0.1	39.978	0.785	5.01
(9,9) - (15,15) - (21,21)	1.22	2.8	12.54	0.1	46.147	0.785	5.79
(12,12) - (18,18) - (24,24)	1.63	3.3	12.54	0.1	55.426	0.786	6.95
(15,15) - (21,21) - (26,26)	2.03	3.5	12.54	0.1	63.657	0.842	7.98
Average:						0.794	5.575

Table B.3 Predicted Young's moduli of Monochiral Four-walled carbon nanotubes.

MWNTs	Diameter		L (nm)	ΔL (nm)	F (nN)	E (TPa)	EA (TPa nm ²)
	d_i (nm)	d_o (nm)					
Zigzag							
(5,0) - (16,0) - (26,0) - (36,0)	0.39	2.8	12.8	0.1	47.545	0.776	6.08
(9,0) - (20,0) - (30,0) - (40,0)	0.70	3.1	12.8	0.1	57.076	0.779	7.29
(12,0) - (22,0) - (32,0) - (42,0)	0.94	3.3	12.8	0.1	62.264	0.791	7.96
(17,0) - (27,0) - (37,0) - (46,0)	1.33	3.6	12.8	0.1	73.376	0.820	9.38
(20,0) - (30,0) - (40,0) - (49,0)	1.57	3.8	12.8	0.1	80.352	0.820	10.27
(25,0) - (35,0) - (44,0) - (53,0)	1.96	4.1	12.8	0.1	90.883	0.843	11.61
Average:						0.805	8.765
Armchair							
(3,3) - (9,9) - (15,15) - (21,21)	0.41	2.8	12.54	0.1	49.232	0.774	6.18
(5,5) - (11,11) - (17,17) - (23,23)	0.68	3.1	12.54	0.1	57.428	0.774	7.20
(7,7) - (13,13) - (19,19) - (24,24)	0.95	3.3	12.54	0.1	64.649	0.823	8.11
(9,9) - (15,15) - (21,21) - (26,26)	1.22	3.5	12.54	0.1	72.930	0.822	9.15
(12,12) - (18,18) - (24,24) - (29,29)	1.63	3.9	12.54	0.1	85.231	0.820	10.69
(15,15) - (21,21) - (26,26) - (31,31)	2.03	4.2	12.54	0.1	95.480	0.858	11.98
Average:						0.812	8.884

Table B.4 Predicted Shear Moduli of Monochiral and Polychiral DWNTs.

DWNTs	Diameter		Intershell Spacing	Inner Chirality	Outer Chirality	Length	Twist angle	Total Torsion	Shear Modulus	Torsional Stiffness
	d_i (nm)	d_o (nm)	d_{002} (nm)	(deg)	(deg)	L (nm)	\emptyset (rad)	T (nN.nm)	G (TPa)	GJ (TPa.nm ⁴)
Zigzag										
(5,0) - (16,0)	0.39	1.25	0.431	0	0	12.78	0.10	1.600	0.313	0.198
(9,0) - (20,0)	0.70	1.57	0.431	0	0	12.78	0.06	2.000	0.305	0.394
(12,0) - (22,0)	0.94	1.72	0.391	0	0	12.78	0.05	2.200	0.319	0.562
(17,0) - (27,0)	1.33	2.11	0.391	0	0	12.78	0.03	2.700	0.309	1.072
(20,0) - (30,0)	1.57	2.35	0.391	0	0	12.78	0.03	3.000	0.300	1.473
(25,0) - (35,0)	1.96	2.74	0.391	0	0	12.78	0.02	3.500	0.296	2.414
(35,0) - (44,0)	2.74	3.44	0.352	0	0	12.78	0.01	4.400	0.341	5.756
Average:									0.312	1.696
Armchair										
(3,3) - (9,9)	0.41	1.22	0.407	30	30	12.54	0.13	1.800	0.305	0.178
(5,5) - (11,11)	0.68	1.49	0.407	30	30	12.54	0.08	2.200	0.306	0.338
(7,7) - (13,13)	0.95	1.76	0.407	30	30	12.54	0.06	2.600	0.302	0.575
(9,9) - (15,15)	1.22	2.03	0.407	30	30	12.54	0.04	3.000	0.297	0.908
(12,12) - (18,18)	1.63	2.44	0.407	30	30	12.54	0.03	3.600	0.286	1.602
(15,15) - (21,21)	2.03	2.85	0.407	30	30	12.54	0.02	4.200	0.276	2.576
(21,21) - (26,26)	2.85	3.53	0.339	30	30	12.54	0.01	5.200	0.403	7.271
Average:									0.311	1.921
Armchair-Chiral										
(2,2) - (13,2)	0.27	1.10	0.417	30	7.1	11.80	0.14	1.500	0.301	0.129
(5,5) - (16,5)	0.68	1.49	0.405	30	13.2	8.00	0.05	2.100	0.289	0.316
(9,9) - (20,9)	1.22	2.01	0.396	30	17.6	10.80	0.04	2.900	0.283	0.833
(13,13) - (24,13)	1.76	2.55	0.391	30	20.3	13.77	0.03	3.700	0.281	1.801
(17,17) - (28,17)	2.31	3.08	0.388	30	22.0	13.53	0.02	4.500	0.256	3.070
(20,20) - (31,20)	2.71	3.48	0.386	30	22.9	13.65	0.01	5.100	0.264	4.724
Average:									0.279	1.812
Zigzag-Chiral										
(3,0) - (13,2)	0.23	1.10	0.435	0	7.1	11.80	0.14	1.500	0.300	0.128
(8,0) - (16,5)	0.63	1.49	0.431	0	13.2	8.00	0.06	2.100	0.279	0.305
(16,0) - (20,9)	1.25	2.01	0.380	0	17.6	10.80	0.04	2.900	0.289	0.850
(23,0) - (24,13)	1.80	2.55	0.372	0	20.3	13.77	0.03	3.700	0.292	1.856
(30,0) - (28,17)	2.35	3.08	0.366	0	22.0	13.53	0.02	4.500	0.268	3.173
(35,0) - (31,20)	2.74	3.48	0.372	0	22.9	13.65	0.01	5.100	0.273	4.853
Average:									0.284	1.861

Table B.5 Predicted Shear Moduli of Monochiral triple-walled carbon nanotubes.

TWNTs	Diameter		Length (nm)	disp (nm)	\emptyset (rad)	J (nm ⁴)	T nN.nm	G (TPa)	GJ (TPa nm ⁴)
	di (nm)	do (nm)							
Zigzag									
(5,0) - (16,0) - (26,0)	0.39	2.0	12.78	0.036	0.035	3.126	2.600	0.301	0.941
(9,0) - (20,0) - (30,0)	0.70	2.3	12.78	0.030	0.026	5.129	3.000	0.292	1.496
(12,0) - (22,0) - (32,0)	0.94	2.5	12.78	0.029	0.023	6.421	3.200	0.280	1.795
(17,0) - (27,0) - (37,0)	1.33	2.9	12.78	0.023	0.016	10.680	3.700	0.281	3.005
(20,0) - (30,0) - (40,0)	1.57	3.1	12.78	0.021	0.013	14.037	4.000	0.275	3.855
(25,0) - (35,0) - (44,0)	1.96	3.4	12.78	0.01573	0.009	19.472	4.400	0.316	6.157
Average:								0.291	2.875
Armchair									
(3,3) - (9,9) - (15,15)	0.41	2.0	12.54	0.042	0.041	3.12	3.000	0.292	0.912
(5,5) - (11,11) - (17,17)	0.68	2.3	12.54	0.037	0.032	4.81	3.400	0.278	1.336
(7,7) - (13,13) - (19,19)	0.95	2.6	12.54	0.032	0.025	7.09	3.800	0.271	1.919
(9,9) - (15,15) - (21,21)	1.22	2.8	12.54	0.029	0.020	10.08	4.200	0.261	2.628
(12,12) - (18,18) - (24,24)	1.63	3.3	12.54	0.024	0.015	16.12	4.800	0.249	4.019
(15,15) - (21,21) - (26,26)	2.03	3.5	12.54	0.041	0.023	21.11	10.400	0.269	5.677
Average:								0.270	2.749

Table B.6 Predicted Shear Moduli of Monochiral four-walled carbon nanotubes.

MWNTs	Diameter		Length (nm)	disp (nm)	ϕ (rad)	J (nm ⁴)	T nN.nm	G (TPa)
	di (nm)	do (nm)						
Zigzag								
(5,0) - (16,0) - (26,0) - (36,0)	0.39	2.8	12.78	0.049	0.035	9.769	7.200	0.270
(9,0) - (20,0) - (30,0) - (40,0)	0.70	3.1	12.78	0.044	0.028	14.257	8.000	0.255
(12,0) - (22,0) - (32,0) - (42,0)	0.94	3.3	12.78	0.042	0.026	16.998	8.400	0.246
(17,0) - (27,0) - (37,0) - (46,0)	1.33	3.6	12.78	0.033	0.018	23.594	9.200	0.271
(20,0) - (30,0) - (40,0) - (49,0)	1.57	3.8	12.78	0.031	0.016	29.639	9.800	0.264
(25,0) - (35,0) - (44,0) - (53,0)	1.96	4.1	12.78	0.026	0.013	39.205	10.600	0.272
Average:								0.263
Armchair								
(3,3) - (9,9) - (15,15) - (21,21)	0.41	2.8	12.54	0.058	0.041	10.14	8.400	0.254
(5,5) - (11,11) - (17,17) - (23,23)	0.68	3.1	12.54	0.053	0.034	14.05	9.200	0.243
(7,7) - (13,13) - (19,19) - (24,24)	0.95	3.3	12.54	0.044	0.027	16.37	9.600	0.274
(9,9) - (15,15) - (21,21) - (26,26)	1.22	3.5	12.54	0.040	0.023	21.86	10.400	0.262
(12,12) - (18,18) - (24,24) - (29,29)	1.63	3.9	12.54	0.036	0.018	32.44	11.600	0.248
(15,15) - (21,21) - (26,26) - (31,31)	2.03	4.2	12.54	0.032	0.015	41.03	12.400	0.246
Average:								0.254

Table B.7 Predicted Shear Strain of Monochiral and Polychiral DWNTs.

DWNTs	Diameter		Intershell Spacing	Inner Chirality	Outer Chirality	Length	Twist angle	Shear Strain
	d_i (nm)	d_o (nm)	d_{002} (nm)	(deg)	(deg)	L (nm)	\emptyset (rad)	Υ
Zigzag								
(5,0) - (16,0)	0.39	1.25	0.431	0	0	12.78	0.10	0.005
(9,0) - (20,0)	0.70	1.57	0.431	0	0	12.78	0.06	0.004
(12,0) - (22,0)	0.94	1.72	0.391	0	0	12.78	0.05	0.003
(17,0) - (27,0)	1.33	2.11	0.391	0	0	12.78	0.03	0.003
(20,0) - (30,0)	1.57	2.35	0.391	0	0	12.78	0.03	0.002
(25,0) - (35,0)	1.96	2.74	0.391	0	0	12.78	0.02	0.002
(35,0) - (44,0)	2.74	3.44	0.352	0	0	12.78	0.01	0.001
Average:								0.003
Armchair								
(3,3) - (9,9)	0.41	1.22	0.407	30	30	12.54	0.13	0.006
(5,5) - (11,11)	0.68	1.49	0.407	30	30	12.54	0.08	0.005
(7,7) - (13,13)	0.95	1.76	0.407	30	30	12.54	0.06	0.004
(9,9) - (15,15)	1.22	2.03	0.407	30	30	12.54	0.04	0.003
(12,12) - (18,18)	1.63	2.44	0.407	30	30	12.54	0.03	0.003
(15,15) - (21,21)	2.03	2.85	0.407	30	30	12.54	0.02	0.002
(21,21) - (26,26)	2.85	3.53	0.339	30	30	12.54	0.01	0.001
Average:								0.004
Armchair-Chiral								
(2,2) - (13,2)	0.27	1.10	0.417	30	7.1	11.80	0.14	0.006
(5,5) - (16,5)	0.68	1.49	0.405	30	13.2	8.00	0.05	0.005
(9,9) - (20,9)	1.22	2.01	0.396	30	17.6	10.80	0.04	0.004
(13,13) - (24,13)	1.76	2.55	0.391	30	20.3	13.77	0.03	0.003
(17,17) - (28,17)	2.31	3.08	0.388	30	22.0	13.53	0.02	0.002
(20,20) - (31,20)	2.71	3.48	0.386	30	22.9	13.65	0.01	0.002
Average:								0.004
Zigzag-Chiral								
(3,0) - (13,2)	0.23	1.10	0.435	0	7.1	11.80	0.14	0.006
(8,0) - (16,5)	0.63	1.49	0.431	0	13.2	8.00	0.06	0.005
(16,0) - (20,9)	1.25	2.01	0.380	0	17.6	10.80	0.04	0.003
(23,0) - (24,13)	1.80	2.55	0.372	0	20.3	13.77	0.03	0.003
(30,0) - (28,17)	2.35	3.08	0.366	0	22.0	13.53	0.02	0.002
(35,0) - (31,20)	2.74	3.48	0.372	0	22.9	13.65	0.01	0.002
Average:								0.004

Table B.8 Predicted Poisson's ratio of Monochiral and Polychiral DWNTs.

DWNTs	Diameter		Empirical intershell spacing (nm)	Intershell Spacing d_{002} (nm)	Inner Chirality (deg)	Outer Chirality (deg)	Length L (nm)	Axial displacement ΔL (nm)	Change in diameter Δd (nm)	Poisson's ratio ν
	d_i (nm)	d_o (nm)								
Zigzag										
(5,0) - (16,0)	0.39	1.25	0.426	0.431	0	0	12.78	0.1	-0.0022	0.229
(9,0) - (20,0)	0.70	1.57	0.414	0.431	0	0	12.78	0.1	-0.0026	0.216
(12,0) - (22,0)	0.94	1.72	0.407	0.391	0	0	12.78	0.1	-0.0025	0.184
(17,0) - (27,0)	1.33	2.11	0.395	0.391	0	0	12.78	0.1	-0.0030	0.178
(20,0) - (30,0)	1.57	2.35	0.390	0.391	0	0	12.78	0.1	-0.0032	0.176
(25,0) - (35,0)	1.96	2.74	0.382	0.391	0	0	12.78	0.1	-0.0037	0.172
(35,0) - (44,0)	2.74	3.44	0.369	0.352	0	0	12.78	0.1	-0.0043	0.159
Average:										0.188
Armchair										
(3,3) - (9,9)	0.41	1.22	0.426	0.407	30	30	12.54	0.1	-0.0018	0.189
(5,5) - (11,11)	0.68	1.49	0.415	0.407	30	30	12.54	0.1	-0.0024	0.198
(7,7) - (13,13)	0.95	1.76	0.406	0.407	30	30	12.54	0.1	-0.0029	0.209
(9,9) - (15,15)	1.22	2.03	0.398	0.407	30	30	12.54	0.1	-0.0029	0.180
(12,12) - (18,18)	1.63	2.44	0.388	0.407	30	30	12.54	0.1	-0.0033	0.169
(15,15) - (21,21)	2.03	2.85	0.380	0.407	30	30	12.54	0.1	-0.0042	0.187
(21,21) - (26,26)	2.85	3.53	0.368	0.339	30	30	12.54	0.1	-0.0058	0.206
Average:										0.191
Armchair-Chiral										
(2,2) - (13,2)	0.27	1.10	0.431	0.417	30	7.1	11.80	0.1	-0.0033	0.352
(5,5) - (16,5)	0.68	1.49	0.415	0.405	30	13.2	8.00	0.1	-0.0066	0.355
(9,9) - (20,9)	1.22	2.01	0.398	0.396	30	17.6	10.80	0.1	-0.0078	0.417
(13,13) - (24,13)	1.76	2.55	0.385	0.391	30	20.3	13.77	0.1	-0.0070	0.376
(17,17) - (28,17)	2.31	3.08	0.376	0.388	30	22.0	13.53	0.1	-0.0071	0.313
(20,20) - (31,20)	2.71	3.48	0.370	0.386	30	22.9	13.65	0.1	-0.0104	0.407
Average:										0.370
Zigzag-Chiral										
(3,0) - (13,2)	0.23	1.10	0.433	0.435	0	7.1	11.80	0.1	-0.0033	0.354
(8,0) - (16,5)	0.63	1.49	0.417	0.431	0	13.2	8.00	0.1	-0.0070	0.378
(16,0) - (20,9)	1.25	2.01	0.397	0.380	0	17.6	10.80	0.1	-0.0089	0.478
(23,0) - (24,13)	1.80	2.55	0.385	0.372	0	20.3	13.77	0.1	-0.0073	0.394
(30,0) - (28,17)	2.35	3.08	0.375	0.366	0	22.0	13.53	0.1	-0.0063	0.275
(35,0) - (31,20)	2.74	3.48	0.369	0.372	0	22.9	13.65	0.1	-0.0071	0.280
Average:										0.360

Table B.9 Predicted Young's moduli of the RVE

Reinforced DWNTs	Diameter of DWNT		Inner Chirality (deg)	Outer Chirality (deg)	RVE	RVE	Length L (nm)	Axial Disp ΔL (nm)	Reaction Force F (nN)	Young's Modulus E (GPa)
	d_i (nm)	d_o (nm)			Diameter d_{RVE} (nm)	Area A_{RVE} (nm ²)				
Zigzag										
(5,0) - (16,0)	0.39	1.25	0	0	7.12	39.80	7.38	0.10	22.82	42.305
(9,0) - (20,0)	0.70	1.57	0	0	8.37	54.96	7.38	0.10	31.73	42.592
(17,0) - (27,0)	1.33	2.11	0	0	10.09	79.16	7.38	0.10	48.55	45.257
(25,0) - (35,0)	1.96	2.74	0	0	11.83	107.94	7.38	0.10	65.93	45.067
Average:										43.805
Armchair										
(3,3) - (9,9)	0.41	1.22	30	30	6.97	38.18	7.38	0.10	23.07	44.596
(5,5) - (11,11)	0.68	1.49	30	30	8.06	50.90	7.38	0.10	30.82	44.669
(9,9) - (15,15)	1.22	2.03	30	30	9.90	76.35	7.38	0.10	46.04	44.488
(15,15) - (21,21)	2.03	2.85	30	30	12.19	114.53	7.38	0.10	69.06	44.495
Average:										44.562
Armchair-chiral										
(5,5) - (16,5)	0.68	1.49	30	13.2	8.04	50.67	7.38	0.10	31.94	46.510
(9,9) - (20,9)	1.22	2.01	30	17.6	9.80	74.78	7.38	0.10	57.22	56.463
(13,13) - (24,13)	1.76	2.55	30	20.3	11.32	98.97	7.38	0.10	64.48	48.073
(17,17) - (28,17)	2.31	3.08	30	22.0	12.68	123.19	7.38	0.10	77.88	46.647
Average:										49.423
Zigzag-chiral										
(8,0) - (16,5)	0.63	1.49	0	13.2	8.08	51.17	7.38	0.10	31.42	45.304
(16,0) - (20,9)	1.25	2.01	0	17.6	9.74	73.87	7.38	0.10	58.96	58.891
(23,0) - (24,13)	1.80	2.55	0	20.3	11.22	97.25	7.38	0.10	65.77	49.896
(30,0) - (28,17)	2.35	3.08	0	22.0	12.55	120.48	7.38	0.10	88.88	54.430
Average:										52.130

Table B.10 Predicted Poisson's Ratio of RVE.

Reinforced DWNTs	Diameter of DWNT		Inner Chirality	Outer Chirality	RVE Diameter	RVE Area	Length	Axial Disp	Change in dia	Poisson's ratio
	d_i (nm)	d_o (nm)	(deg)	(deg)	d_{RVE} (nm)	A_{RVE} (nm ²)	L (nm)	ΔL (nm)	Δd (nm)	ν
<i>Zigzag</i>										
(5,0) - (16,0)	0.39	1.25	0	0	7.12	39.80	7.38	0.10	-0.0277	0.287
(9,0) - (20,0)	0.70	1.57	0	0	8.37	54.96	7.38	0.10	-0.0327	0.289
(17,0) - (27,0)	1.33	2.11	0	0	10.09	79.16	7.38	0.10	-0.0392	0.287
(25,0) - (35,0)	1.96	2.74	0	0	11.83	107.94	7.38	0.10	-0.0463	0.289
Average:										0.288
<i>Armchair</i>										
(3,3) - (9,9)	0.41	1.22	30	30	6.97	38.18	7.38	0.10	-0.0267	0.283
(5,5) - (11,11)	0.68	1.49	30	30	8.06	50.90	7.38	0.10	-0.0312	0.286
(9,9) - (15,15)	1.22	2.03	30	30	9.90	76.35	7.38	0.10	-0.0386	0.287
(15,15) - (21,21)	2.03	2.85	30	30	12.19	114.53	7.38	0.10	-0.0481	0.291
Average:										0.287
<i>Armchair-chiral</i>										
(5,5) - (16,5)	0.68	1.49	30	13.2	8.04	50.67	7.38	0.10	-0.0328	0.301
(9,9) - (20,9)	1.22	2.01	30	17.6	9.80	74.78	7.38	0.10	-0.0415	0.313
(13,13) - (24,13)	1.76	2.55	30	20.3	11.32	98.97	7.38	0.10	-0.0477	0.311
(17,17) - (28,17)	2.31	3.08	30	22.0	12.68	123.19	7.38	0.10	-0.0526	0.306
Average:										0.308
<i>Zigzag-chiral</i>										
(8,0) - (16,5)	0.63	1.49	0	13.2	8.08	51.17	7.38	0.10	-0.0332	0.303
(16,0) - (20,9)	1.25	2.01	0	17.6	9.74	73.87	7.38	0.10	-0.0423	0.321
(23,0) - (24,13)	1.80	2.55	0	20.3	11.22	97.25	7.38	0.10	-0.0476	0.313
(30,0) - (28,17)	2.35	3.08	0	22.0	12.55	120.48	7.38	0.10	-0.0513	0.302
Average:										0.310

APPENDIX C

SENSITIVITY ANALYSIS OF CONTINUUM MODELS

Mesh refinement of the continuum models is important to determine their accurate properties. Table C.1 and Figure C.1 show the sensitivity of Young's moduli of monochiral armchair DWNT (15, 15) – (21, 21) to the influence of mesh size. It can be seen that up to an element number of 57000, the Young's modulus is sensitive to changing mesh size. Further increment of mesh size does not have an influence on the Young's modulus. Therefore, mesh size with 85500 elements is chosen for the said RVE.

Table C.1 Mesh refinement of continuum model RVE reinforced by monochiral armchair DWNT (15, 15) – (21, 21) by Young's modulus sensitivity analysis.

No. of nodes	No. of elements	RVE Area (nm ²)	Length (nm)	ΔL (nm)	F (nN)	E (GPa)
24800	22800	114.53	7.38	0.10	68.80	44.33
29760	27360	114.53	7.38	0.10	68.89	44.39
37200	34200	114.53	7.38	0.10	68.96	44.43
46500	42750	114.53	7.38	0.10	69.00	44.46
62000	57000	114.53	7.38	0.10	69.04	44.49
93000	85500	114.53	7.38	0.10	69.06	44.50
124000	114000	114.53	7.38	0.10	69.07	44.51

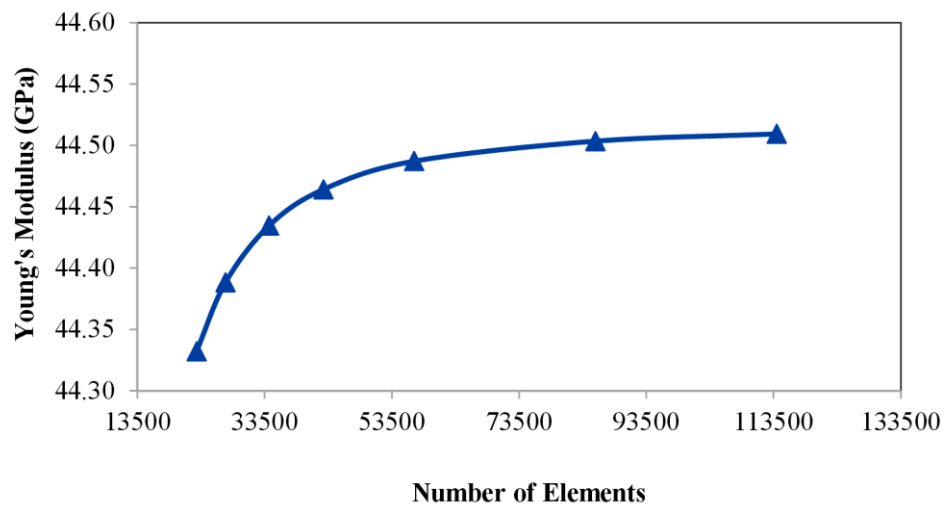


Figure C.1 Mesh refinement of continuum model RVE reinforced by monochiral armchair DWNT (15, 15) – (21, 21).